LUND UNIVERSITY

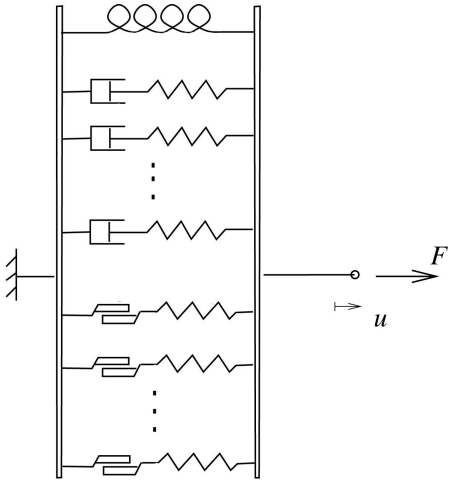

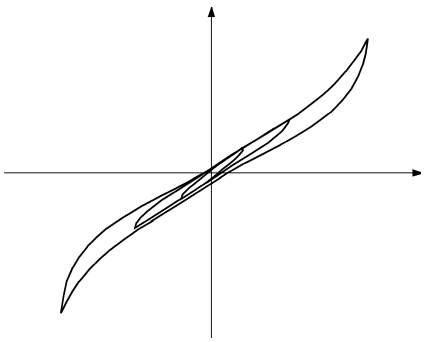

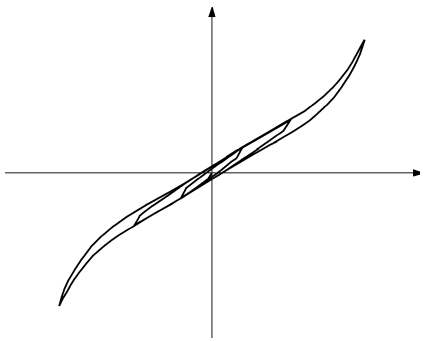

MODELLING NON-LINEAR DYNAMICS OF RUBBER BUSHINGS - Parameter Identification and Validation

FREDRIK KARLSSON and ANDERS PERSSON

Structural Mechanics

Master's Dissertation

Structural Mechanics

ISRN LUTVDG/TVSM--03/5119--SE (1-151)
ISSN 0281-6679

MODELLING NON-LINEAR DYNAMICS OF RUBBER BUSHINGS
- Parameter Identification and Validation

Master's Dissertation by
FREDRIK KARLSSON and ANDERS PERSSON

Supervisors:
Per-Erik Austrell, Div. of Structural Mechanics
Anders Wirje and Jan Hellberg, Volvo Car Corporation

Printed by KFS I Lund AB, Lund, Sweden, August 2003.

For information, address:
Division of Structural Mechanics, LTH, Lund University, Box 118, SE-221 00 Lund, Sweden.
Homepage: http://www.byggmek.lth.se

Preface

This Master's thesis was carried out at the division of Structural Mechanics, Lund University, Sweden, during the period September 2002 - May 2003 in cooperation with the Strength and Durability Centre of Volvo Car Corporation (VCC).

We would like to express our gratitude to our supervisor Ph.D. Per-Erik Austrell at the division of Structural Mechanics, for supporting us with ideas and guidance during the project. We would also like to thank our supervisors at VCC M.Sc. Jan Hellberg and especially M.Sc. Anders Wirje for being a very active supervisor with many thoughts and for supervising the experimental tests performed at VCC. Finally we want to thank Postgrad. S. Anders Olsson for supporting us with useful help regarding MATLAB problems and general questions.

Lund, May 2003

Fredrik Karlsson and Anders Persson

Contents

Chapter 1

Introduction

This Master's dissertation is based mainly on the work done by Per-Erik Austrell [1]. Some text and figures are copied from [1] to give a background for used models.

1.1 Background

Rubber bushings can be found in all vehicle suspension systems. The suspension components are connected to each other, to the subframe, and to the body structure via rubber bushings. They are a key element in designing desired quasi-static and dynamic behaviour of suspension systems. The dynamic characteristics of a rubber bushing are often very complex in nature, due to the fact that the response is dependent on several variables, such as frequency, amplitude, preload, and temperature. The displacement dependence is predominant, but the other dependencies can be absolutely critical in capturing the mechanical behaviour.

Multi-body simulations (MBS) of complete vehicles or subsystems are performed on a daily basis in the automotive industry for analysis of durability, handling, and ride comfort. At Volvo Car Corporation the general MBS code ADAMS is used. To achieve a high level of confidence in the MBS simulations, accurate component models of rubber bushings are crucial. The basic bushing model in ADAMS is simple and lacks frequency and amplitude dependence. In order to refine in-house bushing models and to develop more advanced models it is of greatest interest to perform systematic studies of the dynamic behaviour of rubber bushings.

1.2 Objective

This Master's thesis work addresses the non-linear dynamic behaviour of rubber bushings and methods to model dynamically loaded rubber components.

The main objectives of this project are to:

- Gain further insight in material characteristics and dynamic properties of rubber components.
- Analyse and determine the validity of different bushing models.
- Evaluate a methodology for model parameter identification from physical component tests.
- Give directions for rubber bushing modelling in MBS models.

The ultimate objective is to establish a methodology/work flow for rubber bushing modelling and parameter identification, which can be implemented into a commercial MBS code and used in the product development of new cars.

1.3 Project overview

The project is conducted in cooperation between Volvo Car Corporation, Lund Institute of Technology and Forsheda rubber company. The studied approach for bushing modelling is based on model parameter identification from physical component tests.

Major activities:

- Create and study different 1-D bushing models in MATLAB:
  -Viscoelastic models including Kelvin-Voigt, Zener, and Generalized Maxwell (no amplitude dependence).
  -Elastoplastic models (no frequency dependence).
  -Generalized viscoplastic models (both frequency and amplitude dependence).
- Evaluate a methodology for model parameter identification from physical component tests.
- Validate the bushing models by comparison with component testing.

The viscoelastic models are unable to model amplitude dependence and the elastoplastic models are unable to model frequency dependence. The generalized viscoplastic (viscoelastic elastoplastic) models describe both amplitude and frequency

dependence. Therefore are the generalized viscoplastic models more carefully studied.

Three rubber components have been used to validate the bushing models for harmonic behaviour. Two of the components are geometrically simple model components and the third is an actual component used in a Volvo car. The first model component is a double shear specimen giving an almost homogeneous state of shear strain. This state of strain is advantageous because rubber is almost linear in simple shear, making it possible to avoid non-linear elastic behaviour and isolate the non-linear dynamic behaviour that originates from the filler induced damping. The second model component is a cylindrical bushing with simple geometry (i.e. no cavities). The third component is a hydrobushing 'taken from the shelf' with material and geometry as specified for the Volvo car.

Two materials with different dynamic characteristics have been chosen for the two model components, which are manufactured by Forsheda rubber company. One material with low filler content, corresponding to what is normally used in the automotive industry, and one material with high content of filler have been studied.

1.4 Dynamic modulus and phase angle

The dynamic modulus and phase angle are used here to characterize the dynamic properties. The definition of these parameters has its origin in linear dynamic behaviour of viscoelastic materials.

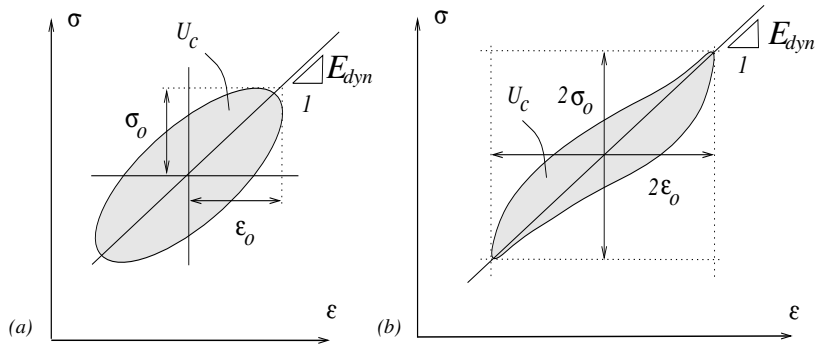

Figure 1.1: *Linear viscoelastic (a) and general (b) hysteresis loop for harmonic excitation.*

Linear dynamic is characterized by sinusoidal response to sinusoidal excitation. The response is of the same frequency but shifted by a phase angle δ. Figure 1.1(a) corresponds to linear (viscoelastic) behaviour, which is characterized by a pure elliptical form. Figure 1.1(b) is more general where non-linearities are present. The non-linear behaviour appears as a distortion of the hysteresis loop. These non-linearities are due to non-linear elasticity and/or frictional damping (filler structure breakdown and reforming).

On the basis of a steady state harmonic excitation the *dynamic modulus* is defined according to Figure 1.1 as

$$E_{dyn} = \frac{\sigma_0}{\epsilon_0} \tag{1.1}$$

Note that the dynamic modulus for the non-linear case is not unambiguous by this definition since the same dynamic modulus can be achieved with different hysteresis (if σ_0 and ϵ_0 is the same).

The dissipated energy U_c for each strain cycle is related to the phase angle δ according to $U_c = \pi\sigma_0\epsilon_0 \sin(\delta)$. This expression is derived in connection with linear viscoelastic models in Appendix B and is only valid for linear viscoelastic materials. The *normalized damping* d is defined according to

$$d = \sin(\delta) = \frac{U_c}{\pi\sigma_0\epsilon_0} \tag{1.2}$$

For moderate damping, $\sin(\delta) \approx \delta$, it is concluded that the normalized damping d will coincide with the phase angle (loss angle).

1.5 Summary of harmonic dynamic properties

Deviations from linear dynamic behaviour are caused by the underlying non-linear elastic properties and/or by the damping mechanisms introduced by the filler.

For unfilled rubbers, a linear viscoelastic behaviour can be observed in simple shear, which is a linear mode of deformation if the strains are not too large. In the case of filled rubbers, non-linear dynamic behaviour is present even for simple shear due to breakdown and reforming of the carbon-black structure.

Important dynamic properties of carbon-black-filled natural rubbers are summarized here.

- In harmonic loading it can be observed that the dynamic modulus shows a considerable amplitude dependence. The modulus declines with amplitude towards an asymptotic value for large amplitudes. The damping represented by the equivalent phase angle reaches a maximum where the decline in modulus is the greatest (cf. Figure A.8).

- Payne [10] interpreted the decline in dynamic modulus for increasing strain amplitude as a result of breaking of the filler structure. Payne found that the modulus is almost recoverable upon return to small amplitudes, i.e. the filler structure largely reforms for an amplitude cycle.

- Mullins' effect is attributed to breaking of the cross-links between the filler and elastomeric material, which results in decline in dynamic modulus for increasing strain amplitude. This breaking of cross-links between the filler and elastomeric material has a recovery time of less than 24 hours.

- The dynamic modulus is almost recoverable for a strain cycle with increasing amplitude followed by decreasing amplitude in harmonic testing. The mechanisms on microstructural level involved must therefore be different from the mechanisms involved in the Mullins' effect. The explanation lies in the breakdown and quick reforming of the carbon-black structure.

- In quasi-static loading it can be observed that a difference between loading and unloading curves is present irrespective of how low the loading rate is, according to [1]. It can also be observed that the hysteresis loop in quasi-static loading for heavily filled rubber takes the approximate shape of a parallelogram, according to [1].

- The shape of the strain history in quasi-static loading does not appreciately influence the shape of the hysteresis loop. Triangular shaped periodic shear strain and sinusoidal shear strain in quasi-static loading gives almost the same hysteresis loops, according to [1].

- The shape of the decline of the dynamic modulus with amplitude is insensitive to frequency. Experiments indicate that the amplitude and frequency dependence are separable (cf. Figure A.9).

1.6 Material model for rubber

A starting point for the modelling of filled rubbers is the simple one-dimensional model of elastic and damping properties shown in Figure 1.2. The elastic behaviour is provided by the spring element, which is assumed to be non-linear. Damping is modelled by the rate-dependent viscous damper and the rate-independent frictional element. The frictional element makes it possible to model hysteresis in quasi-static load cases, i.e. when the strain rate approaches zero.

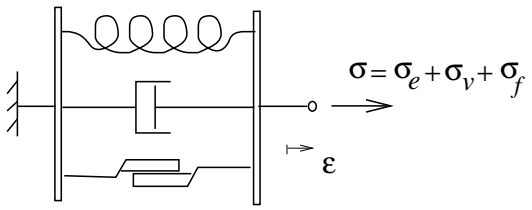

Figure 1.2: *Simple one-dimensional rheological model including non-linear elastic, viscous, and frictional properties.*

The elastic, viscous, and frictional forces act in parallel, and the total stress is the sum of the stresses in the elements, i.e. $\sigma = \sigma_e + \sigma_v + \sigma_f$. The viscous stress σ_v corresponds to dissipative stresses in the rubber network. Stresses in the filler phase and in the rubber-filler interfaces are responsible for the rate-independent contribution σ_f.

This model incorporates some important aspects of the mechanical behaviour of filled rubbers. Frequency dependence, effects of static load on the dynamic modulus, distortion of the elliptic shape of the hysteresis loop, and amplitude dependence are properties of the simple model. However, it has some unphysical properties, e.g. discontinuous stress response for continuous strain and inability to exhibit relaxation behaviour. More sophisticated models are therefore needed.

1.7 Other work within this field

Here follows a discussion of experimental investigations and modelling of dynamic properties of rubber. These properties are dependent on frequency, temperature, static load, and amplitude. Special emphasis will here be on strain amplitude dependence.

The dynamic modulus is seen to decrease with increasing strain amplitude. This effect is sometimes denoted the Payne effect due to investigations of reinforced elastomers made by Payne [10]. He interpreted the decline in modulus for increasing strain amplitude as a result of breaking of the filler structure. The structure is composed of aggregates held together by van der Waals bonds. Payne found that the modulus is almost recoverable upon return to small amplitudes, i.e. the filler structure largely reforms for an amplitude cycle.

Payne also observed that the shape of the decline in modulus for increasing strain amplitude was almost independent of frequency for low frequencies, and he also refers to Warnaka [21] who observed the same frequency independence for higher frequencies, up to 1500 Hz.

A comprehensive review of dynamic properties of carbon-black-filled rubbers and the amplitude dependence can be found in the often-cited article by Medalia [18].

Experimental investigations suggest that unfilled rubbers can be modelled by viscoelastic models, whereas the behaviour of filled rubbers can not, according to Stevenson [5] and other researchers. The amplitude dependence of the dynamic modulus is significant for filled rubbers and is in general more important than the influence of frequency and temperature. It should be observed that the amplitude dependence is not included in the viscoelastic models.

A one-dimensional model of the amplitude dependence for periodic sinusoidal loading was suggested by Kraus [17]. This model explains the amplitude dependence by continuous breaking and reforming of van der Waals bonds between carbon-black aggregates. The Kraus model has been investigated and evaluated by many researchers, see for example Ulmer [19] and Vieweg [20]. The latter finds that the sigmoidal decline (in logarithmic coordinates) of the dynamic modulus does not depend on frequency for the investigated range $0.06 - 20$ Hz.

Rate-independent damping mechanisms have been employed to model the amplitude dependence of the dynamic stiffness for lumped damper models, usually expressed in terms of force and displacement relations as is also employed here. It will be argued that viscoplasticity is necessary to explain the non-linear dynamic

behaviour of rubbers with filler.

One-dimensional models of the type discussed here have been used as models of dampers, often described in terms of a force and displacement relationship. Gregory [15] and Coveney [14] have modelled the rate-independent damping of rubber by using frictional elements.

Similar models have been used for example in vehicle dynamics or earthquake protection applications. Berg [12] has proposed a five-parameter rubber spring model with elastic, frictional, and viscous forces in parallel, for dynamic analysis of rail vehicles.

This model has been assimilated by Kari and Sjöberg [16] who used the frictional part in the model by Berg together with a rate-dependent part using fractional derivatives. This approach yields a very elegant solution to the problem of the weak rate-dependence of most rubbers. The rate-dependent part can be modelled by only two parameters by using fractional derivatives. The essential drawback is that the numerical evaluation requires a large portion of the strain history to be stored and used in each increment.

A so-called stress fraction model is the basis of this work and it originates from a constitutive model, i.e. a multiaxial model of rubber behaviour on a material level. It relies on summing stress contributions obtained from simple constitutive models for each fraction. This model was originally proposed by Besseling [13]. The basic concept of this model is that the material is thought to be subdivided into a number of parallel fractions, each with simple conventional properties. The more complicated behaviour of real materials is approximated by choosing a number of parallel fractions with suitable models and model parameters. The original fraction model was formulated for small strains, and it has been applied to metal plasticity and creep phenomena in metals.

This model has been adopted by Austrell and Olsson [4] in the context of finite element analysis. Here it is used as a lumped model on a structural level to model the dynamic behaviour of rubber bushings. Basic features of the model is that it contains three major branches, i.e. a non-linear elastic, a viscoelastic, and an elastoplastic (frictional) branch. The viscoelastic and the elastoplastic branches are then in turn divided into smaller fractions. The basic viscoelastic fraction is the Maxwell modell and the basic elastoplastic fraction is the von Mises model without any hardening behaviour.

A major advantage with this approach is that each fraction can be expressed in a very simple format giving a numerically efficient evaluation of general strain histories. The rate-dependent (viscoelastic) branch of stress (or force) is evaluated by simple time-stepping where only the previous time step needs to be stored. The elastoplastic branch is also evaluated with a simple algorithm for each fraction. The main drawback is the large number of parameters required. However, the determination of model parameters is in this work made by utilising an automatic procedure due to Olsson and Austrell [3].

Chapter 2

Generalized material models for rubber

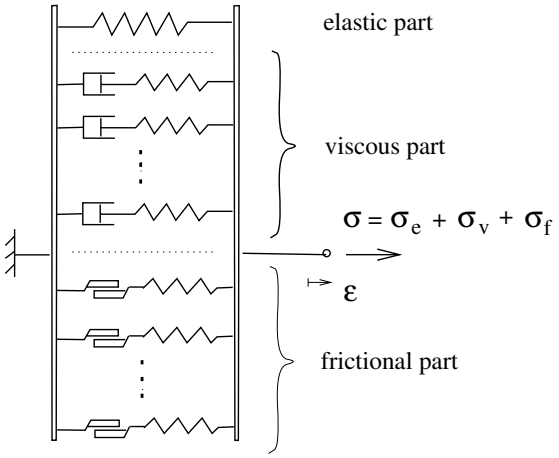

Figure 2.1: *One-dimensional model including elastic, viscous, and friction properties.*

A generalized material model with several Maxwell and frictional elements connected in parallel according to Figure 2.1 is discussed in this chapter. The model has an elastic part that can be non-linear elastic. This model is used later in terms of force and displacement for modelling the three test specimens. This chapter also includes the stress response algorithm for the basic elements used in the generalized one-dimensional material models. Most of the figures and text in this chapter are copied from the PhD thesis by Per-Erik Austrell [1].

2.1 Generalized Maxwell model

The generalized Maxwell model (Figure 2.2) is discussed in terms of complex modulus and also its response to a general strain history.

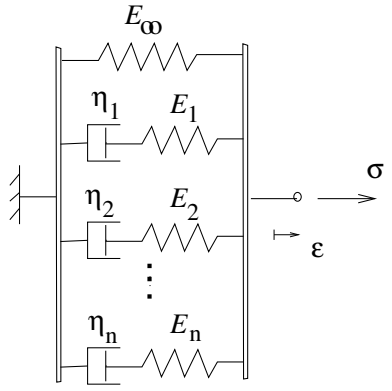

Figure 2.2: *The generalized Maxwell model.*

The Zener model in Appendix B can be generalized by adding more Maxwell elements in parallel with the linear spring c.f. Figure 2.2. This yields a so-called *generalized Maxwell model* with properties qualitatively the same as the Zener model but with better ability to accurately fit experimental data.

We denote the stress in the spring component with σ_∞ and the stress in the first Maxwell element with σ_{M1}, etc. The total stress σ in the generalized model is

$$\sigma = \sigma_\infty + \sigma_{M1} + \sigma_{M2} + \dots \sigma_{Mn} \tag{2.1}$$

with

$$\sigma_\infty = E_\infty \epsilon \tag{2.2}$$

By using (B.51) it is concluded that the differential equation for one Maxwell element is given by

$$\dot{\sigma}_{Mj} + \frac{E_j}{\eta_j}\sigma_{Mj} = E_j \dot{\epsilon} \tag{2.3}$$

Solving (2.3) for all elements and summing stresses according to (2.1) defines the stress-strain relation for the generalized Maxwell model.

Solving equation (2.3) for a step strain history yields

$$\sigma_R(t) = E_\infty \epsilon_0 + \epsilon_0 \sum_{j=1}^{n} E_j e^{\frac{-E_j}{\eta_j}t} \qquad t > 0 \tag{2.4}$$

The relaxation modulus for the generalized model is consequently established by summing the individual Maxwell modulis, giving a so called Prony series

$$E_R(t) = E_\infty + \sum_{j=1}^{n} E_j e^{-t/t_{rj}} \tag{2.5}$$

The complex modulus for the generalized Maxwell model can be derived in a similar manner, i.e. by summing the complex modulis,

$$E^*(\omega) = E_\infty + \sum_{j=1}^{n} E_j \frac{i\omega t_{rj}}{1 + i\omega t_{rj}}$$

giving the complex modulus for the generalized model.

Another way to determine the complex modulus, is as mentioned in Appendix B, by Fourier transforming the dimensionless relaxation modulus.

2.2 Stress response algorithm for the Maxwell model

Consider the hereditary integral which was derived in Appendix B that defines the linear viscoelastic stress response for an arbitrary strain history

$$\sigma(t) = \int_{-\infty}^{t} E_R(t-\tau)\frac{d\epsilon}{d\tau}d\tau$$

The relaxation modulus for a Maxwell element is expressed according to $E_R(t) = Ee^{-t/t_r}$ where $t_r = \eta/E$. Inserting this expression in the above hereditary integral gives

$$\sigma(t) = Ee^{-t/t_r}\int_{-\infty}^{t} e^{\tau/t_r}\frac{d\epsilon}{d\tau}d\tau \tag{2.6}$$

Similarly for time $t + \Delta t$

$$\sigma(t+\Delta t) = Ee^{-(t+\Delta t)/t_r}\int_{-\infty}^{t+\Delta t} e^{\tau/t_r}\frac{d\epsilon}{d\tau}d\tau$$

The increment $\Delta\sigma = \sigma(t+\Delta t) - \sigma(t)$ is given by

$$\Delta\sigma = \sigma(t)(e^{-\Delta t/t_r} - 1) + Ee^{-(t+\Delta t)/t_r}\int_{t}^{t+\Delta t} e^{\tau/t_r}\frac{d\epsilon}{d\tau}d\tau \tag{2.7}$$

with $\sigma(t)$ according to (2.6).

For small time steps Δt it is possible to approximate the integral in equation (2.7) by the trapezoidal rule

$$\int_{t}^{t+\Delta t} e^{\tau/t_r}\frac{d\epsilon}{d\tau}d\tau \approx \frac{1}{2}(e^{(t+\Delta t)/t_r} + e^{t/t_r})\Delta\epsilon$$

Equation (2.7) can now be written on the form

$$\Delta\sigma = A + B\Delta\epsilon$$

where $A = \sigma(t)(e^{-\Delta t/t_r} - 1)$ and $B = \frac{E}{2}(1 + e^{-\Delta t/t_r})$.

A simple time stepping algorithm for determining the stress from an arbitrary strain history can hence be written

for $i = 1$ *to* n

$A = \sigma_{i-1}(e^{-\Delta t/t_r} - 1)$

$B = \frac{E}{2}(1 + e^{-\Delta t/t_r})$

$$\Delta\sigma = A + B\Delta\epsilon_i$$
$$\sigma_i = \sigma_{i-1} + \Delta\sigma$$

A considerable numerical advantage of this form is that the stress increment is directly computed only from the state of the previous time step. This is in contrast to theories involving fractional derivatives which require storage of a large part of the strain history.

2.3 Generalized frictional solid model

The elastoplastic part is discussed here in terms of dynamic modulus and damping according to the definition (1.2) in Section 1.4. Moreover, a general algorithm for the stress response is presented.

The *generalized frictional solid model* includes several frictional elements. The stress-strain relation becomes more smooth when more frictional elements are used, but the derivative of the stress history is still discontinuous. This phenomena is shown in Figure 2.3.

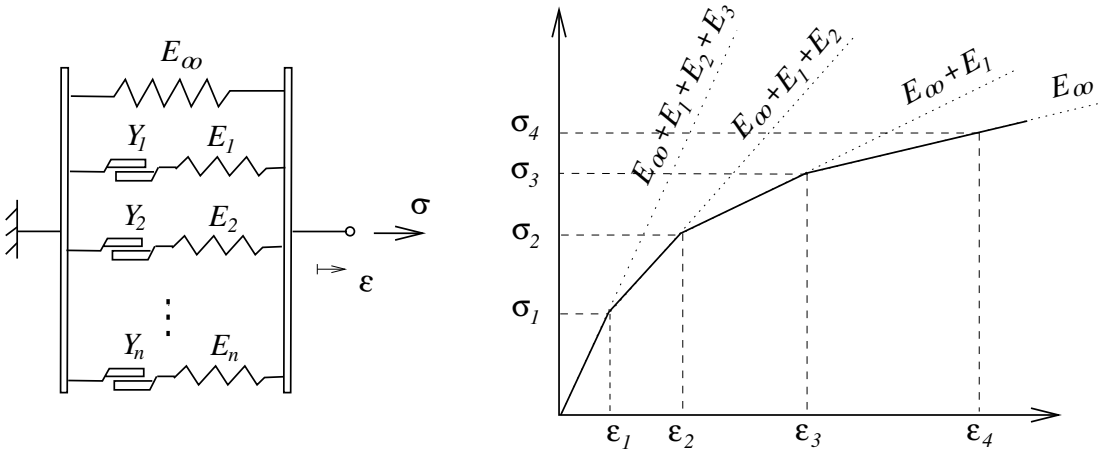

Figure 2.3: *The generalized frictional solid model and corresponding initial loading curve.*

The model parameters can be obtained from the initial loading curve. It is a piecewise linear curve according to Figure 2.3. The elements are assumed to yield in the order $1, 2, \ldots n$ i.e. from above in Figure 2.3, and a particular break point means that limit load has been reached in one element. The parameters are determined directly from

$$E_i = \frac{\sigma_i - \sigma_{i-1}}{\epsilon_i - \epsilon_{i-1}} - \frac{\sigma_{i+1} - \sigma_i}{\epsilon_{i+1} - \epsilon_i} \qquad \text{and} \qquad Y_i = E_i\epsilon_i \tag{2.8}$$

The inverse relation, i.e. the break points obtained from the model parameters, is

given by

$$\epsilon_i = \frac{Y_i}{E_i} \qquad \text{and} \qquad \sigma_i = \sum_{k=1}^{i-1} E_k \epsilon_k + (E_\infty + \sum_{k=i}^{n} E_k)\, \epsilon_i$$

where it is assumed that the first sum vanishes if i=1.

The dynamic modulus for the generalized model is also found directly from the loading curve. Values of the dynamic modulus for amplitudes corresponding to the break point strains are

$$E^i_{dyn} = \frac{\sigma_i}{\epsilon_i}$$

The damping for the strain amplitudes corresponding to the break points can be determined by calculating the enclosed areas for the frictional elements that have reached yielding, using definition (1.2) in Section 1.4.

The algorithm for each stress element is very simple and will be discussed in detail in the next section. The model has the important characteristic that the amplitude dependence of filled rubbers can be modelled in detail.

2.4 Stress history algorithm for the basic frictional solid model

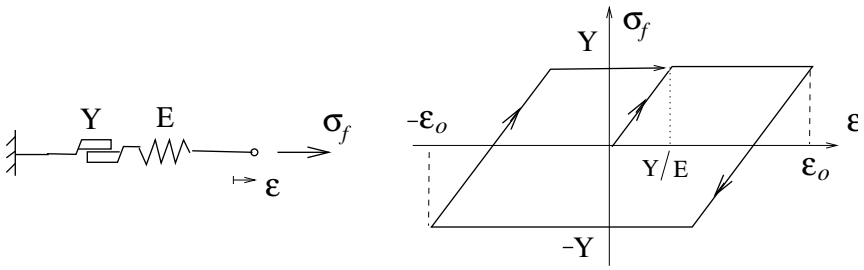

Figure 2.4: *Frictional stress in the basic element.*

The rate-independent damping is symbolized by two blocks with sliding friction that is fully developed when the stress in the element reaches the yield stress $\sigma_f = Y$. The stress-strain relationship for the basic element, according to Figure 2.4, must be evaluated for increments of strain and stress. The strain is a sum of elastic and (frictional) plastic strain $\epsilon = \epsilon^e + \epsilon^p$.

To obtain an algorithm an incremental relation given by

$$\Delta\epsilon = \Delta\epsilon^e + \Delta\epsilon^p$$

is employed. The task is to find the stress increment $\Delta\sigma_f$. It can be derived from the elastic part, because the stress is the same in the elastic and the frictional element giving $\sigma_f = E\,\epsilon^e$. Hence, the stress increment can always be expressed as

$$\Delta\sigma_f = E\Delta\epsilon^e$$

A trial stress is determined from the assumption that the strain increment is purely elastic. Suppose that the current stress σ_f is known. The trial stress is then

$$\sigma^{trial} = \sigma_f + E\Delta\epsilon$$

The total stress is limited to $-Y < \sigma_f < Y$; this condition is tested for each increment. If the trial stress σ^{trial} is larger than the yield stress, then at least a part of the strain increment is plastic. Eventually we have $\Delta\epsilon^e = 0$, if the strain increment is purely plastic. We get the condition

$$if \quad |\, \sigma^{trial} \,| > Y \;\; then \;\; \sigma_f = \pm Y \tag{2.9}$$

Hence, the stress has to be scaled back to $\sigma_f = \pm Y$ if the condition (2.9) is fulfilled. A scale factor $\alpha = Y/\sigma^{trial}$ is introduced and the stress is consequently obtained as $\sigma_f = \alpha\sigma^{trial}$. If the condition (2.9) is not fulfilled then we have a purely elastic stress and $\sigma = \sigma^{trial}$ i.e. the strain increment is elastic.

The algorithm for determining the stress can now be written

$$\begin{aligned}
&i = 1, 2, 3... \\
&\quad \Delta\epsilon = \epsilon^{i+1} - \epsilon^i \\
&\quad \sigma^{trial} = \sigma_f^i + E\Delta\epsilon \\
&\quad \alpha = Y/\sigma^{trial} \\
&\quad if \;\; \alpha > 1 \;\; then \;\; \alpha = 1 \\
&\quad \sigma_f^{i+1} = \alpha\sigma^{trial}
\end{aligned}$$

2.5 Generalized viscoelastic elastoplastic model

As mentioned in Appendix A the reorganization of the rubber network during periodic loading results in frequency dependent loss angle and dynamic modulus. Heavily filled rubber prove to have a very strong amplitude dependence with respect to both loss angle and dynamic modulus. This is believed to be caused by the breakdown and reforming of the filler structure.

The rubber network and filler give two kinds of damping, viscous and frictional damping. A combination of rate-independent and rate-dependent damping is needed to account for the inelastic effects in the filled rubber. The combination of a viscoelastic and elastoplastic model, gives a so-called *viscoelastic elastoplastic (viscoplastic) material model*.

2.5.1 Generalized linear elastic viscoelastic elastoplastic model

A successful way to model the different kinds of damping is to combine the linear spring, the Maxwell elements, and the frictional elements, according to Figure 2.5. This model is called the *generalized linear elastic viscoelastic elastoplastic model*. It

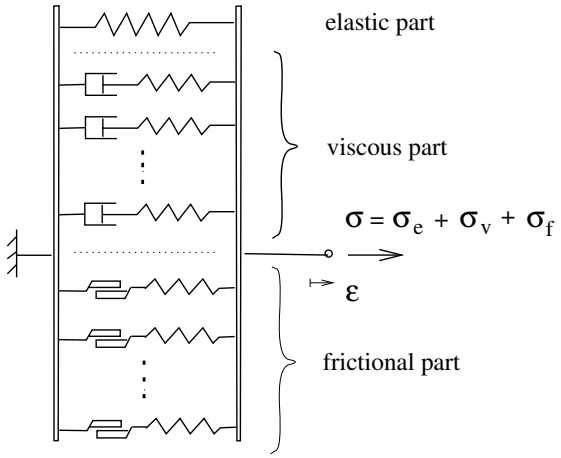

Figure 2.5: *One-dimensional model including elastic, viscous, and friction properties.*

will be shown that this model can be made to fit static, quasi-static, and dynamic tests with reasonable accuracy. The stress expression is calculated by

$$\sigma = \sigma_e + \sigma_v + \sigma_f$$

Several viscous elements make it possible to conduct a fit of the dynamic modulus to a wider frequency range, or in the time range, fit the relaxation over a wider time range. Likewise, several frictional elements make it possible to closely fit the amplitude dependence for larger variations in the amplitude.

2.5.2 Generalized non-linear elastic viscoelastic elastoplastic model

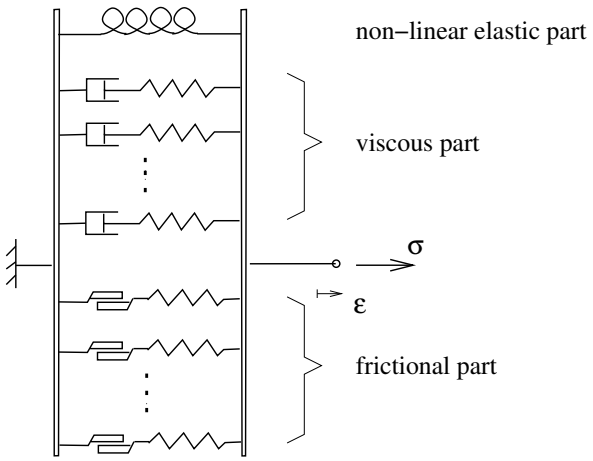

Figure 2.6: *One-dimensional model including non-linear elastic, viscous, and friction properties.*

The generalized non-linear elastic viscoelastic elastoplastic model includes a non-linear elastic stress component.

This model is the same as the previous model except that the linear elastic spring is replaced by a non-linear elastic spring (cf. Figure **??**) with a stiffness $E_e(\epsilon)$ dependent on the actual strain ϵ. The stress is expressed in an incremental manner by

$$\Delta\sigma = E_e(\epsilon)\Delta\epsilon + \Delta\sigma_v + \Delta\sigma_f$$

and the total stress in the whole model is obtained from

$$\begin{aligned} i &= 1, 2, 3 \ldots \\ \Delta\sigma_i &= E_e(\epsilon)\Delta\epsilon_i + \Delta\sigma_i^v + \Delta\sigma_i^f \\ \sigma_i &= \sigma_{i-1} + \Delta\sigma_i \end{aligned}$$

Chapter 3

Transition from material to structural level

In this chapter, the transition from material to structural level is discussed. Constitutive relations on a material level have been established in Appendix B and the previous chapter, i.e. in terms of stresses and strains. The following chapters will deal with relations on a structural level, i.e. in terms of forces and displacements, since the experimental data are established as forces and displacements. The only difference between the two levels will turn out to be a geometrical factor for simple geometries and homogeneous states of stress.

Young's modulus E (N/m^2) transforms to a stiffness K (N/m) by a geometrical factor. Likewise can the viscosity coefficient η (Ns/m^2) be transformed to a viscous damping coefficient c (Ns/m) by a geometrical factor. This is here shown for a structural geometry in the form of a simple bar. A force F is applied to a bar with a material assumed to be linear elastic with Young's modulus E (N/m^2). The bar has a cross section A and length L and will extend the distance u *(m)* when the force F is applied. On the material level it is well known that $\sigma = E\epsilon$ i.e. $F/A = Eu/L$ which leads to $F = Ku$ where $K = EA/L$ (N/m) and A/L represents the geometrical factor. If the force F instead is applied to a bar with a purely viscous material with the viscosity coefficient η (Ns/m^2) the expression on material level is $\sigma = \eta\dot{\epsilon}$. The expression $\sigma = \eta\dot{\epsilon}$ is rewritten as $F/A = \eta\dot{u}/L$ which leads to $F = c\dot{u}$ where $c = \eta A/L$ (Ns/m). Also in this case the geometrical factor A/L arises.

3.1 Viscoelastic and frictional models

The derived expressions in Appendix B can easily and in a straight-forward manner be converted from material to structural level. The conversion is shown for the complex modulus of the Zener model

$$E^*(\omega) = E_\infty + E\frac{i\omega t_r}{1 + i\omega t_r}$$

Assume again that the structural geometry is in the form of a simple bar. The complex modulus is converted to structural level by multiplication of a geometrical factor A/L according to

$$\frac{A}{L}E^*(\omega) = \frac{A}{L}E_\infty + \frac{A}{L}E\frac{i\omega t_r}{1+i\omega t_r}$$

or

$$K^*(\omega) = K_\infty + K\frac{i\omega t_r}{1+i\omega t_r}$$

where $t_r = c/K$

Likewise, the enclosed area U_c in a hysteresis loop of an arbitrary linear viscoelastic material in the $(\sigma, \epsilon) - plane$ is $U_c = \pi\sigma_0\epsilon_0 \sin\delta$ (see equation (1.2)). If the structural geometry is in the form of a simple bar, $U_c = \pi(F_0u_0/AL)\sin\delta$. The enclosed area in the $(F, u) - plane$ can therefore be expressed as $U_s = \pi F_0u_0 \sin\delta$ where $U_s = ALU_c$, (i.e. total strain energy).

frictional model. Assume next that we have a pure frictional model. For a simple bar with cross section A and length L then σ_f transforms according to

$$\sigma_f = sign(\dot{\epsilon})Y \Rightarrow F_f = sign(\dot{u})F_y$$

where $F_f = \sigma_f A$, $F_y = YA$ and $\dot{u} = \dot{\epsilon}L$

3.2 Non-linear elastic models

The difference between stress-strain and force-displacement relationship is shown for the Yeoh material. In shear, (B.21) and (B.22) yields

$$\frac{P}{A} = 2(C_{10} + 2\kappa^2C_{20} + 3\kappa^4C_{30})\kappa \tag{3.1}$$

with $\kappa = u/H$

$$P = 2A(C_{10} + 2(\frac{u}{H})^2C_{20} + 3(\frac{u}{H})^4C_{30})\frac{u}{H} \tag{3.2}$$

Defining $AC_{10}/H = D_{10}$, $AC_{20}/H^3 = D_{20}$, and $AC_{30}/H^5 = D_{30}$ gives the following force-displacement relationship

$$P = 2(D_{10} + 2D_{20}u^2 + 3D_{30}u^4)u \tag{3.3}$$

A similar expression can be obtained for a compression/tension like behaviour by using (B.4) and (B.11).

Chapter 4

Laboratory experiments

Figure 4.1: *The test specimens. From left: shear specimen, cylindrical bushing, and hydrobushing.*

This chapter concerns testing of three different kinds of rubber components, two geometrically simple components and one bushing taken from a Volvo car. The first component is a *double shear specimen*. The second component is a *cylindrical bushing* and the third component is a *hydrobushing* existing in a Volvo car. The first two components are made in two kinds of natural rubber (NR), which have the same hardness but different filler content. Static, quasi-static, and steady state harmonic dynamic testing have been conducted for the rubber components. The components are conditioned to avoid Mullins' effect. The frequency and amplitude dependence of dynamic stiffness and phase angle have been studied in detail.

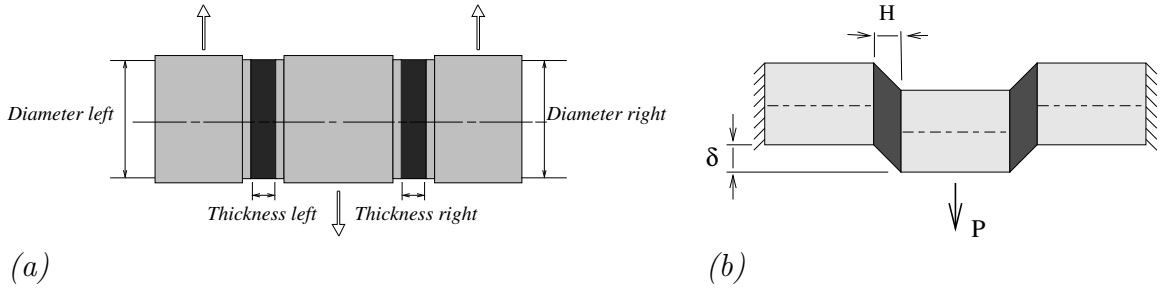

Figure 4.2: *(a) Double shear specimen (nominal geometry). (b) Displacement in double shear specimen, $\kappa = \delta/H$.*

4.1 Test specimens

Three different kinds of rubber components are as mentioned studied in this Master's dissertation. Two of them are geometrically simple components and the third is an actual component used in a Volvo car. The double shear specimens and cylindrical bushings have been manufactured by Forsheda rubber company. The Volvo bushing is a so-called hydrobushing and can be found in the S60, S80, V70, and XC70 cars.

The double shear specimen illustrated in Figure 4.1 and 4.2 gives an almost homogeneous state of shear strain up to about $\kappa = 100\%$. This state of strain is advantageous since rubber is almost linear elastic in simple shear, making it possible to isolate the non-linear dynamic behaviour that originates from inelastic effects, i.e. viscous and frictional damping. It is desirable to isolate this non-linear dynamic behaviour for validation of the amplitude and frequency dependence of the material models. The shear specimen has been made in two kinds of natural rubber with different amount of filler. The geometry of the double shear specimens can be seen in Table 4.1.

The second component is a cylindrical bushing with simple geometry, see Figure 4.1. This component expects to show a strong non-linear elastic behaviour for large displacements in radial loading. A major purpose for studying this component is to investigate the material models ability to capture non-linear elasticity in combination with viscous and frictional damping. The cylindrical bushings have been made in the same two rubber compounds as the double shear specimens. Material properties and geometry of the cylindrical bushings are listed in Table 4.2.

The third component, a hydrobushing from Volvo Car Corporation, can be seen in Figure 4.1. The hydrobushing consists of natural rubber and cavities partly filled with a fluid. The fluid (glycol) can stream between different chambers through channels. The component is designed to give high damping for low amplitudes and a specific frequency.

The rubber material

The double shear specimen and the cylindrical bushing have been manufactured in two natural rubber compounds. Both the compounds have a hardness of 50 IRHD

Shear spec.	Diameter left [mm]	Diameter right [mm]	Thickness left [mm]	Thickness right [mm]	Material	Hardness [IRHD]	Loss angle [deg]
A	24.96	25.01	5.09	4.52	NR	50	5
B	24.93	24.94	5.33	5.99	NR	50	14.5

Table 4.1: *Material properties and geometry of the shear specimens.*

Cylindrical bushing	Outer Diameter[1] [mm]	Radial thickness[2][mm]	Length [mm]	Material	Hardness [IRHD]	Loss angle [deg]
C	50.17	12.75	40.37	NR	50	5
D	50.27	12.72	39.82	NR	50	14.5

Table 4.2: *Material properties and geometry of the cylindrical bushings.*
[1] *Distance between the outer housing's outer sides.*
[2] *Measured from the outer housing's inner side to the inner housing's outer side.*

and will consequently have similar stiffness properties. One of the compounds is low filled and the other is highly filled. The low filled natural rubber has a nominal phase angle of 5 degrees, which is a typical phase angle for NR in automotive applications. The highly filled material has a nominal phase angle of 14.5 degrees and is chosen to validate the material models for, from an automotive point of view, very high-damped natural rubber. The low filled compound is used in shear specimen A and cylindrical bushing C, whereas the highly filled compound is used in shear specimen B and cylindrical bushing D.

4.2 Test method

The tests have been carried out by Lars Janerstål at the Materials Centre of Volvo Car Corporation. All tests have been performed with a *Schenck* static/dynamic tensile testing machine, see Figure 4.3. The machine has a load cell with maximum capacity of ±7 kN which is 110% of the maximum level of stretch used in the testing and is able to measure at a frequency interval of 0.1-1000 Hz. The used software is *TEST STAR II*. The accuracy measured at the latest calibration occation is less than ±0.1% in the middle of the measuring interval, and up to at the most ±0.5% at the wings of the interval. It is possible to increase the accuracy even at low loads by choosing interval depending on the components stiffness.

The components are as mentioned mechanically conditioned to avoid Mullins' effect. It is important to perform this condition properly because the usefulness of the test data depends on how the mechanical conditioning has been performed. The method to condition the components used in this Master's dissertation is the *one-level conditioning*, see Figure 4.4. This one-level method uses only one level of stretch in the conditioning procedure, and it is also the maximum level + 10% of stretch used in the testing. In order to avoid heat build-up in the component it is

Figure 4.3: *The machine used for testing. A Schenck static/dynamic tensile testing machine.*

important to not cycle the component too long. The components are exposed to 3 cycles. A disadvantage of the one-level method, is that it tends to lower the stiffness of the vulcanizate too much in regions of small stretch values, according to [1]. The order of the tests have been chosen to preserve the conditioning during the tests. The testing has been conducted with the highest amplitude first and continued with decreasing amplitudes.

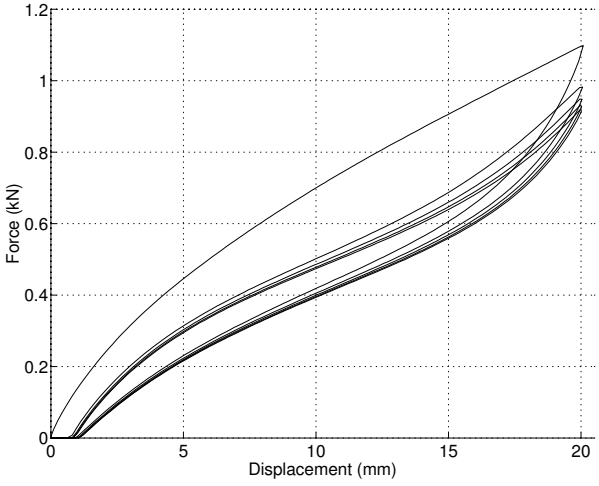

Figure 4.4: *The one-level conditioning of rubber components.*

4.3 Overview of performed tests

The three chosen components have been experimentally tested at the Materials Centre laboratory of Volvo Car Corporation. Static, quasi-static, and steady state harmonic dynamic tests have been conducted and they are listed in Table 4.3, 4.4, and 4.5 respectively. The components, i.e. the shear specimens, the cylindrical bushings, and the hydrobushing have been tested in the radial direction. To avoid Mullins' effect, the test specimens have been mechanically conditioned. The strategy to preserve the conditioning during the testing has been to test the highest amplitude first and to continue with decreasing amplitudes.

Static testing

The static tests have been conducted with a triangular displacement history, i.e. with a constant velocity. The tested amplitudes for each component are listed in Table 4.3. The shear specimens are tested with a constant velocity v=0.05 mm/s. The cylindrical bushings are tested with v=0.05 mm/s except for the amplitude 0.12 mm which is tested with v=0.01 mm/s. The hydrobushing is tested with v=0.05 mm/s except for the amplitudes 0.5 mm, 0.2 mm, and 0.12 mm which are tested with v=0.01 mm/s.

Component	Amplitude [mm] Shear strain [%] is given for the shear specimens
Shear specimen A (low filled)	0.12(2%), 0.30(5%), 0.60(10%), 1.2(20%), 3.0(50%), 6.0(100%), 9.0(150%)
Shear specimen B (high filled)	0.12(2%), 0.30(5%), 0.60(10%), 1.2(20%), 3.0(50%), 6.0(100%), 9.0(150%)
Cylindrical bushing C (low filled)	0.12, 0.30, 0.60, 1.2, 3.0, 6.25
Cylindrical bushing D (high filled)	0.12, 0.30, 0.60, 1.2, 3.0, 6.25
Hydrobushing	0.12, 0.20, 0.50, 0.80, 1.0, 1.5, 2.0, 3.0, 4.0, 4.5

Table 4.3: *Static tests.*

Quasi-static testing

The quasi-static tests have been performed with a sinusoidal displacement history at 0.03 Hz. The tested amplitudes for each component are listed in Table 4.4.

Component	Frequency [Hz]	Amplitude [mm]
Cylindrical bushing C (low filled)	0.03	0.20, 0.50, 0.80, 1.0, 1.5, 2.0, 3.0, 5.0
Cylindrical bushing D (high filled)	0.03	0.20, 0.50, 0.80, 1.0, 1.5, 2.0, 3.0, 5.0
Hydrobushing	0.03	0.20, 0.50, 0.80, 1.0, 1.5, 2.0, 3.0

Table 4.4: *Quasi-static tests.*

Steady state harmonic dynamic testing

The dynamic tests have been performed as discrete frequency sweeps for a given amplitude. The amplitudes and frequency sweeps for each component can be seen in Table 4.5.

Component	Frequency [Hz]	Amplitude [mm] Shear strain [%] is given for the shear specimens
Shear specimen A (low filled)	0.1-1 (Δf=0.1) 1-49 (Δf=3)	0.012(0.2%), 0.030(0.5%), 0.060(1%), 0.12(2%), 0.30(5%), 0.60(10%), 1.2(20%), 3.0(50%)
Shear specimen B (high filled)	0.1-1 (Δf=0.1) 1-49 (Δf=3)	0.012(0.2%), 0.030(0.5%), 0.060(1%), 0.12(2%), 0.30(5%), 0.60(10%), 1.2(20%), 3.0(50%)
Cylindrical bushing C (low filled)	1-51 (Δf=2)	0.20, 0.50, 0.80, 1.0, 1.5, 2.0, 3.0
Cylindrical bushing D (high filled)	1-51 (Δf=2)	0.20, 0.50, 0.80, 1.0, 1.5, 2.0, 3.0
Hydrobushing	1-41 (Δf=2)	0.10, 0.20, 0.50, 0.80, 1.0, 1.5, 2.0

Table 4.5: *Steady state harmonic dynamic tests.*

4.4 Analysis of experimental data

In this section, the experimental tests results are presented and some conclusions are drawn. The amplitude and frequency dependence of the dynamic stiffness and phase angle have been studied in detail. (The definition of dynamic modulus and phase angle are discussed in Chapter 1). As mentioned in Chapter 3, the only difference between dynamic modulus and dynamic stiffness is a geometrical factor. The expression for dynamic stiffness can thus easily be derived. The components with highly filled natural rubber are expected to show a strong amplitude dependence. Non-linear elastic behaviour is expected for the cylindrical bushings and the hydrobushing when they are subjected to large displacements.

4.4.1 Double shear specimens

The double shear specimens are studied in this section. The static tests are first discussed and thereafter the steady state harmonic dynamic tests.

Static tests

Static test results are shown in Figure 4.5. It is clearly seen that the hysteresis loops for the high filled specimen B is wider than the corresponding ones for the low filled specimen A. The wider hysteresis loops for specimen B are due to damping, in this case frictional damping induced by the filler. The amplitude dependence of high filled natural rubber is illustrated in Figure 4.5(c), where a higher amplitude gives a lower static stiffness. For the higher amplitudes in Figure 4.5(b) and (d), influence of non-linear elasticity can be seen.

Steady state harmonic dynamic tests

Steady state harmonic dynamic tests have been performed to analyse the amplitude and frequency dependence of the dynamic stiffness and phase angle. An overview of the results are shown in Figure 4.6.

The experimental testing was not completely successful. The plots for the amplitudes 0.012 and 0.030 mm are irregular for both specimen A and B, see Figure 4.6 and 4.8. These amplitudes are neglected in the following chapters. From Figure 4.6 it is obvious that the dynamic stiffness and phase angle are dependent on amplitude and frequency.

The amplitude dependence is studied in detail by 2-D plots of dynamic stiffness and phase angle as function of amplitude for some specific frequencies (0.1, 13, and 49 Hz) cf. Figure 4.7. The high filled shear specimen B has a strong amplitude dependence with respect to dynamic stiffness. Increasing amplitude gives decreasing stiffness. It is a bit unexpected that the low filled shear specimen A is so amplitude dependent since the amplitude dependence originates from the filler. Shear specimen B has higher dynamic stiffness than shear specimen A due to higher filler content, especially at low amplitudes according to Figure 4.6 (a), 4.6(c), 4.7(a), and 4.7(c).

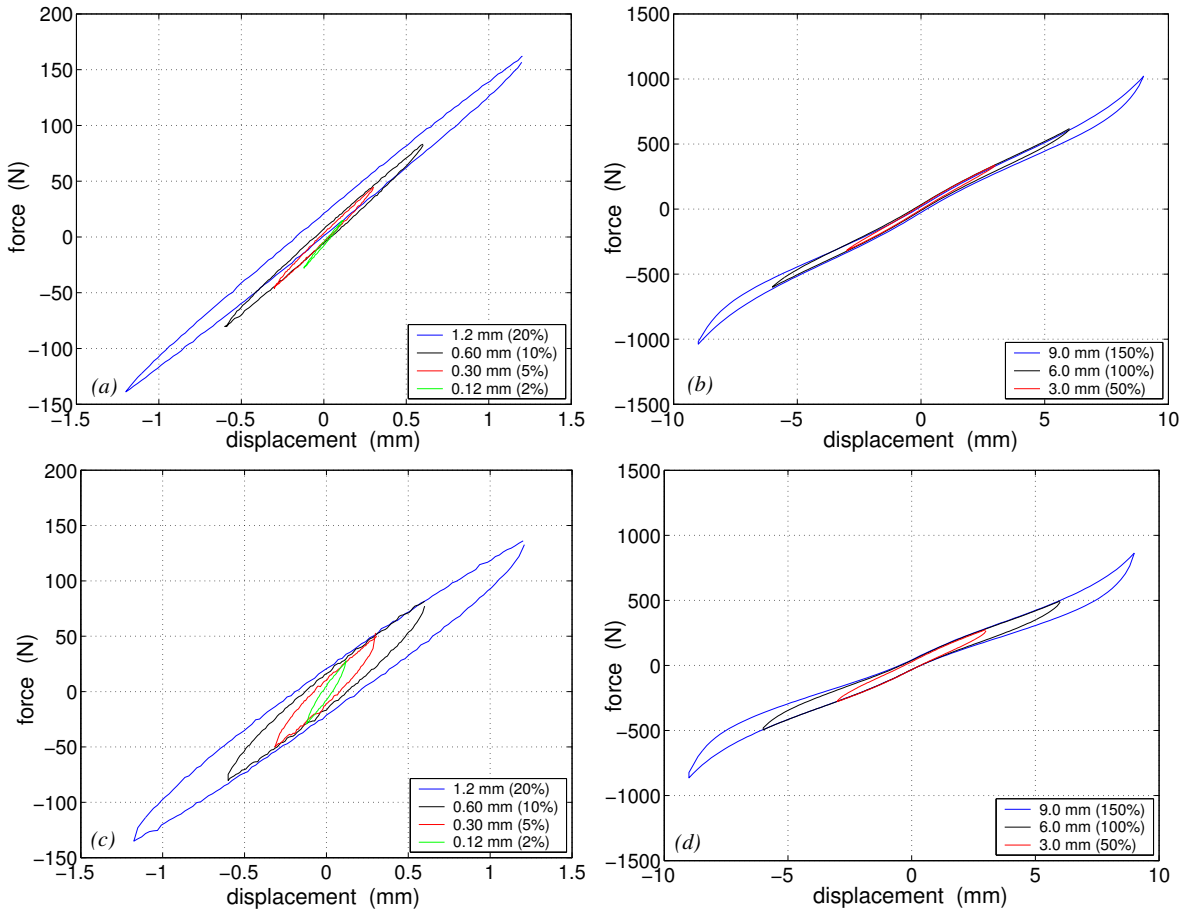

Figure 4.5: *Static characteristics for double shear specimens. Hysteresis loops for amplitudes between 0.12 and 9.0 mm. Low filled specimen A in (a) and (b), high filled specimen B in (c) and (d). Corresponding shear strain is given for each amplitude.*

Phase angle as function of amplitude is plotted in Figure 4.7(b) and (d). The phase angle increases with amplitude for the lowest amplitudes, whereas it decreases with amplitude for the other amplitudes.

The frequency dependence of the shear specimens can be seen in Figure 4.8 where 2-D plots of dynamic stiffness and phase angle as function of frequency are shown. Increasing frequency results in increasing dynamic stiffness and phase angle due to the viscous damping. The frequency dependence of the two shear components are very similar, but somewhat stronger for the high filled specimen B. Figure 4.7 and 4.8 indicate that the frequency and amplitude dependence are separated from each other, i.e. uncoupled. This important conclusion can be drawn since all the curves within each plot in Figure 4.7 and 4.8 can be established by translating one of the curves in the plots.

Hysteresis loops are plotted force-displacement relationships as mentioned in Chapter 1. These plots contain information about dynamic stiffness and phase angle. The dynamic stiffness is given by the slope of the hysteresis loop. A steep

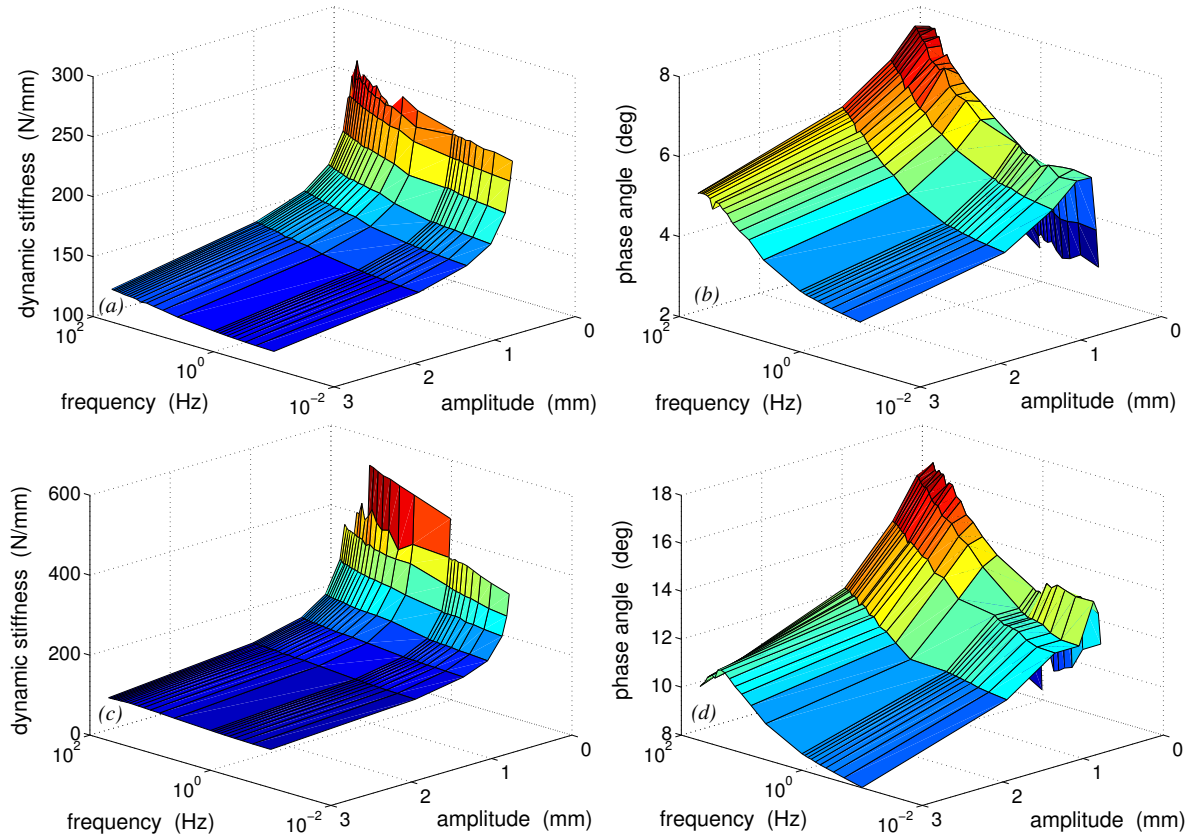

Figure 4.6: *Steady state harmonic dynamic characteristics for the double shear specimens. Dynamic stiffness and phase angle as function of amplitude and frequency. Low filled specimen A in (a) and (b), high filled specimen B in (c) and (d).*

hysteresis corresponds to a high stiffness. The phase angle is proportional to the enclosed area of the hysteresis. Hysteresis loops are plotted in Figure 4.9. The amplitude dependence is very clear, especially for shear specimen B. The frequency dependence is more indistinct, but dynamic stiffness and phase angle increase with frequency. The same set of hysteresis loops as in Figure 4.9 but for the amplitudes 0.60, 1.2, and 3.0 mm can be seen in Figure 4.10. They show the same behaviour as is seen for the lower amplitudes.

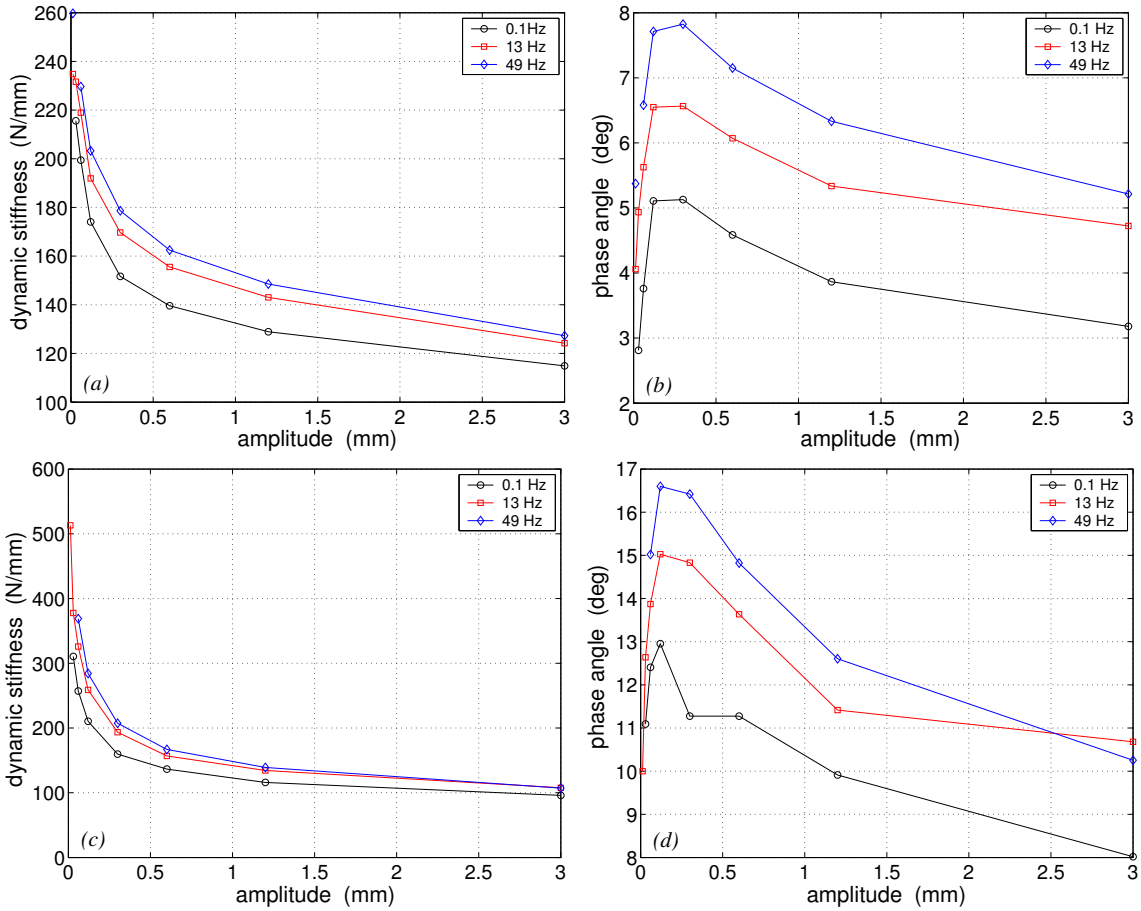

Figure 4.7: *Steady state harmonic dynamic characteristics for the double shear specimens. Dynamic stiffness and phase angle as function of amplitude for some specific frequencies (0.1, 13, 49 Hz). Low filled specimen A in (a) and (b), high filled specimen B in (c) and (d).*

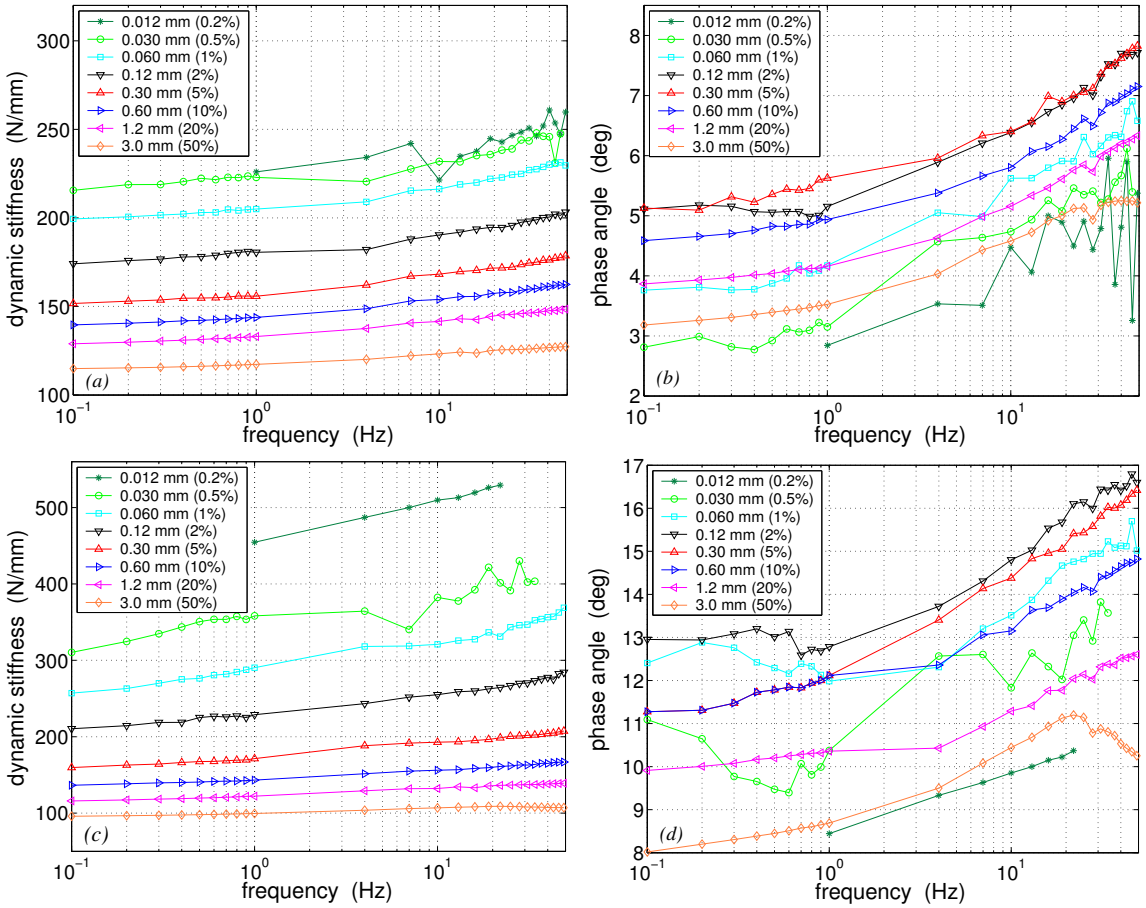

Figure 4.8: *Steady state harmonic dynamic characteristics for the double shear specimens. Dynamic stiffness and phase angle as function of frequency for different amplitudes. Low filled specimen A in (a) and (b), high filled specimen B in (c) and (d). Corresponding shear strain is given for each amplitude.*

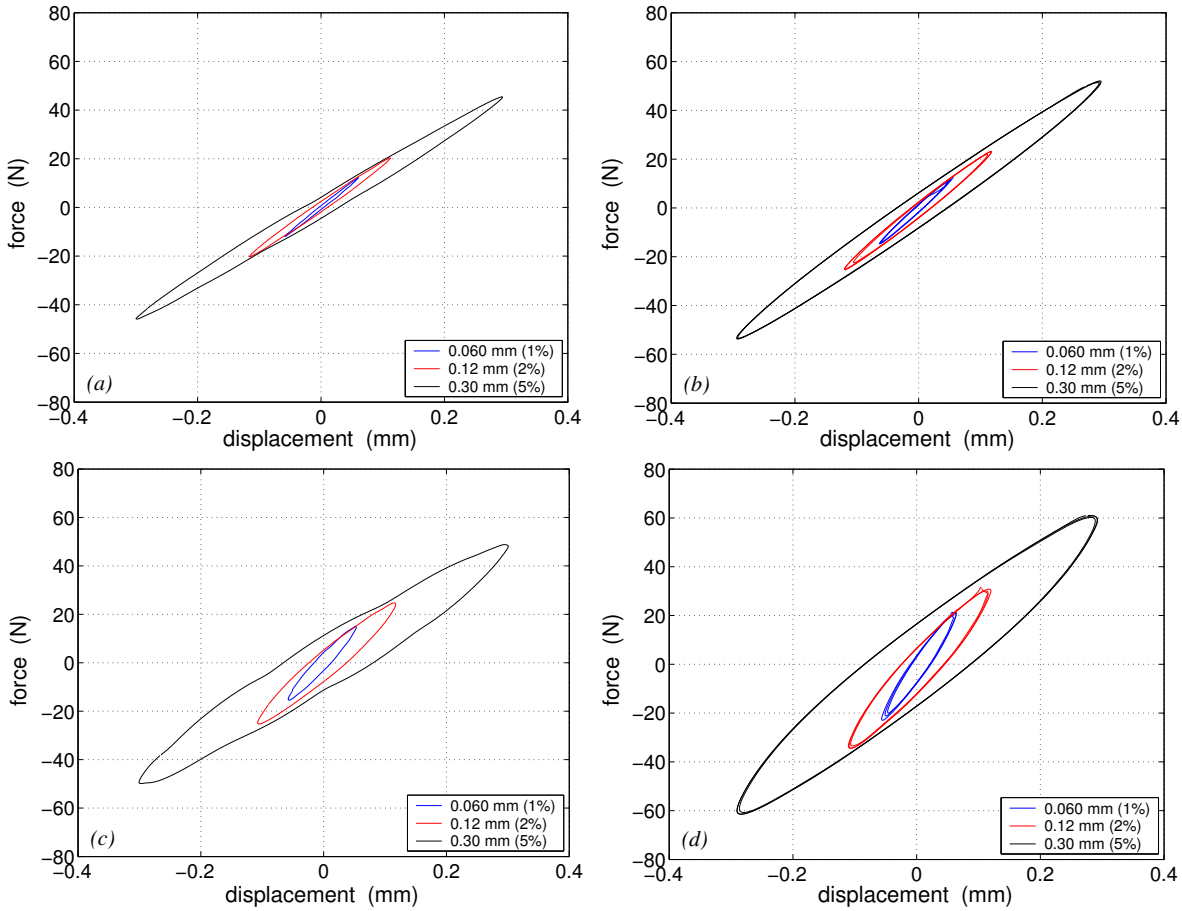

Figure 4.9: *Steady state harmonic dynamic characteristics for the double shear specimens. Hysteresis loops for some different amplitudes at 0.3 Hz ((a) and (c)) and at 49 Hz ((b) and (d)). Low filled specimen A in (a) and (b), high filled specimen B in (c) and (d). Corresponding shear strain is given for each amplitude.*

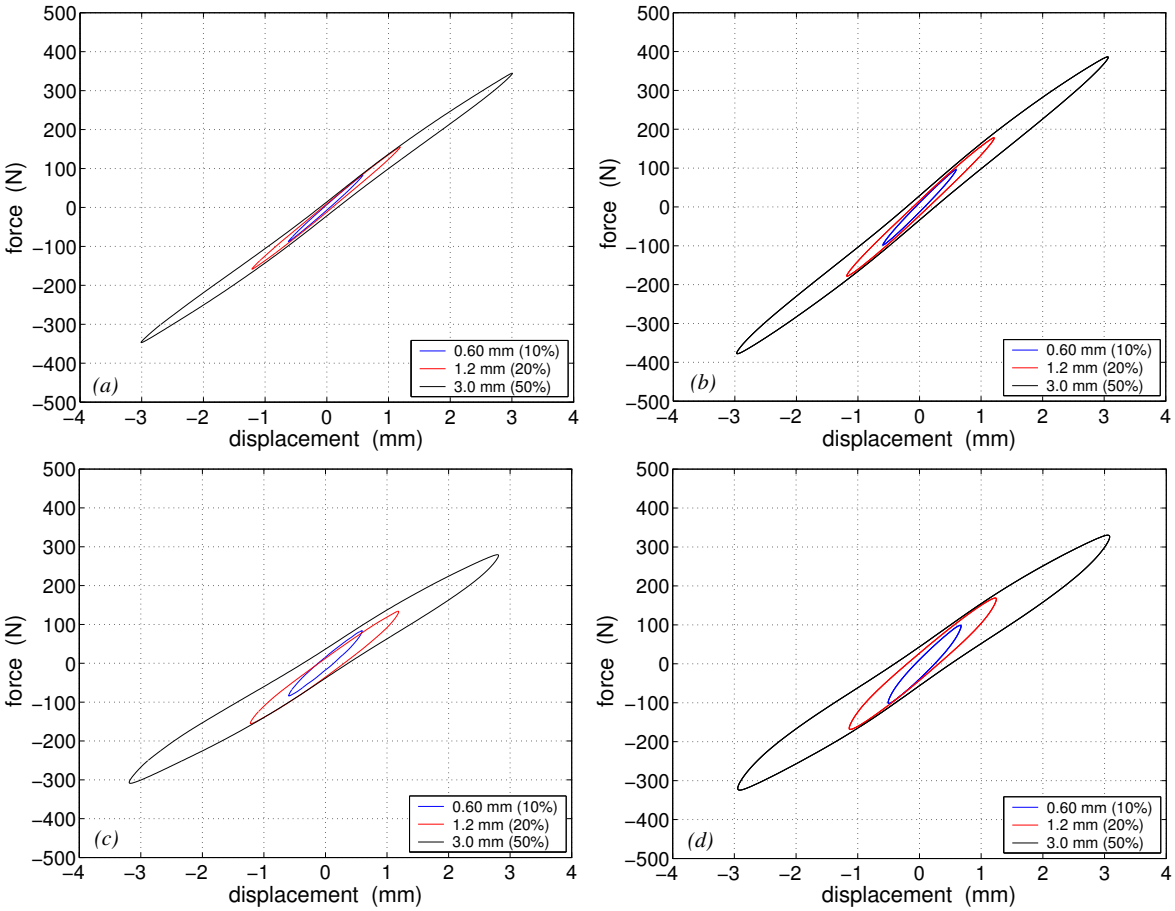

Figure 4.10: *Steady state harmonic dynamic characteristics for the double shear specimens. Hysteresis loops for some different amplitudes at 0.3 Hz ((a) and (c)) and at 49 Hz ((b) and (d)). Low filled specimen A in (a) and (b), high filled specimen B in (c) and (d). Corresponding shear strain is given for each amplitude.*

4.4.2 Cylindrical bushings

The cylindrical bushings are studied in this section. The static tests are first presented, thereafter the quasi-static tests and finally the steady state harmonic dynamic tests. As mentioned earlier in this chapter, the tests are performed in radial direction.

Static tests

Static test results are shown in Figure 4.11. Influence of non-linear elasticity can be seen for the highest amplitude. The amplitude dependence for the lowest amplitudes is strong, resulting in increasing stiffness for decreasing amplitude cf. Figure 4.11(c).

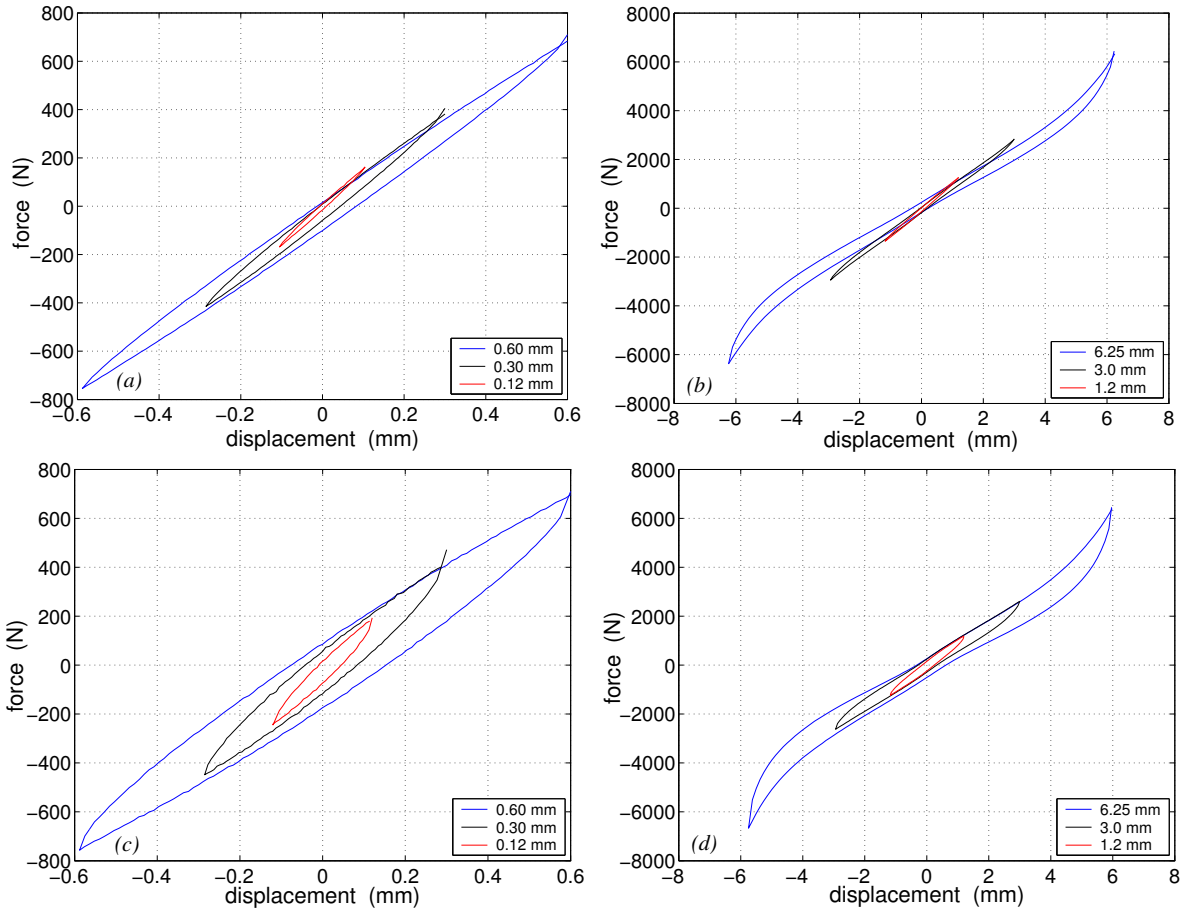

Figure 4.11: *Static characteristics for the cylindrical bushings. Hysteresis loops for amplitudes between 0.12 and 6.25 mm. Low filled specimen C in (a) and (b), high filled specimen D in (c) and (d).*

Quasi-static tests

Quasi-static test results are given in Figure 4.12. The hysteresis loop for the highest amplitude is non-linear, which is caused by a combination of non-linear elasticity and frictional damping. As pointed out in Chapter 1, the hysteresis for a linear viscoelastic material has an elliptical shape. The highest amplitude in Figure 4.12(e) and (f) has more of a parallelogram-shaped hysteresis. The hysteresis loops for the lower amplitudes are more elliptical-shaped.

Steady state harmonic dynamic tests

As for the shear specimens, steady state harmonic dynamic tests have been performed to analyse the amplitude and frequency dependence. The results are presented in 3-D plots cf. Figure 4.13 to give an overview of the dynamic behaviour. The amplitude and frequency dependence are studied in detail by 2-D plots of dynamic stiffness and phase angle as function of amplitude (for some specific frequencies) and frequency (for different amplitudes) cf. Figure 4.14 and 4.15.

The dynamic testing was successful for all frequencies and amplitudes. From Figure 4.13 it is obvious that the dynamic stiffness and phase angle are dependent on amplitude and frequency. The high filled cylindrical bushing has as expected a strong amplitude dependence with respect to dynamic stiffness and phase angle. Cylindrical bushing C has also a strong amplitude dependence, which is quite unexpected since it has a low filler content (the amplitude dependence originates from the filler).

2-D plots of the amplitude dependence are shown in Figure 4.14. The dynamic stiffness and phase angle decrease with increasing amplitude, except for the lowest amplitude where the phase angle for some cases increases with increasing amplitude.

Dynamic stiffness and phase angle are as expected higher for the high filled specimen D. Note the decrease in dynamic stiffness as the amplitude increases from 0.20 to 3.0 mm. The stiffness is reduced by a factor of 2 for specimen D and significantly reduced for specimen C. The two cylindrical bushings have the same dynamic stiffness for an amplitude of 1.5 mm, see Figure 4.14(a) and (c).

The frequency dependence is shown in Figure 4.15. Both dynamic stiffness and phase angle generally increase with increasing frequency. The two cylindrical bushings have a very similar frequency dependence. Just as for the shear specimens, Figure 4.14 and 4.15 indicate that the frequency and amplitude dependence are separated from each other, i.e. uncoupled. This important conclusion can be drawn since all the curves within each plot in Figure 4.14 and 4.15 can be established by translating one of the curves in the plots.

Hysteresis loops are plotted in Figure 4.16. The amplitude dependence is very clear, especially for the high filled cylindrical bushing D. The frequency dependence is more indistinct, but dynamic stiffness and phase angle increase with frequency. As earlier mentioned, the dynamic stiffness is given by the slope of the hysteresis loop and the phase angle is proportional to the enclosed area of the loop. The same set of hysteresis loops as in Figure 4.16 but for the amplitudes 1.5, 2.0, and 3.0 mm can be seen in Figure 4.17.

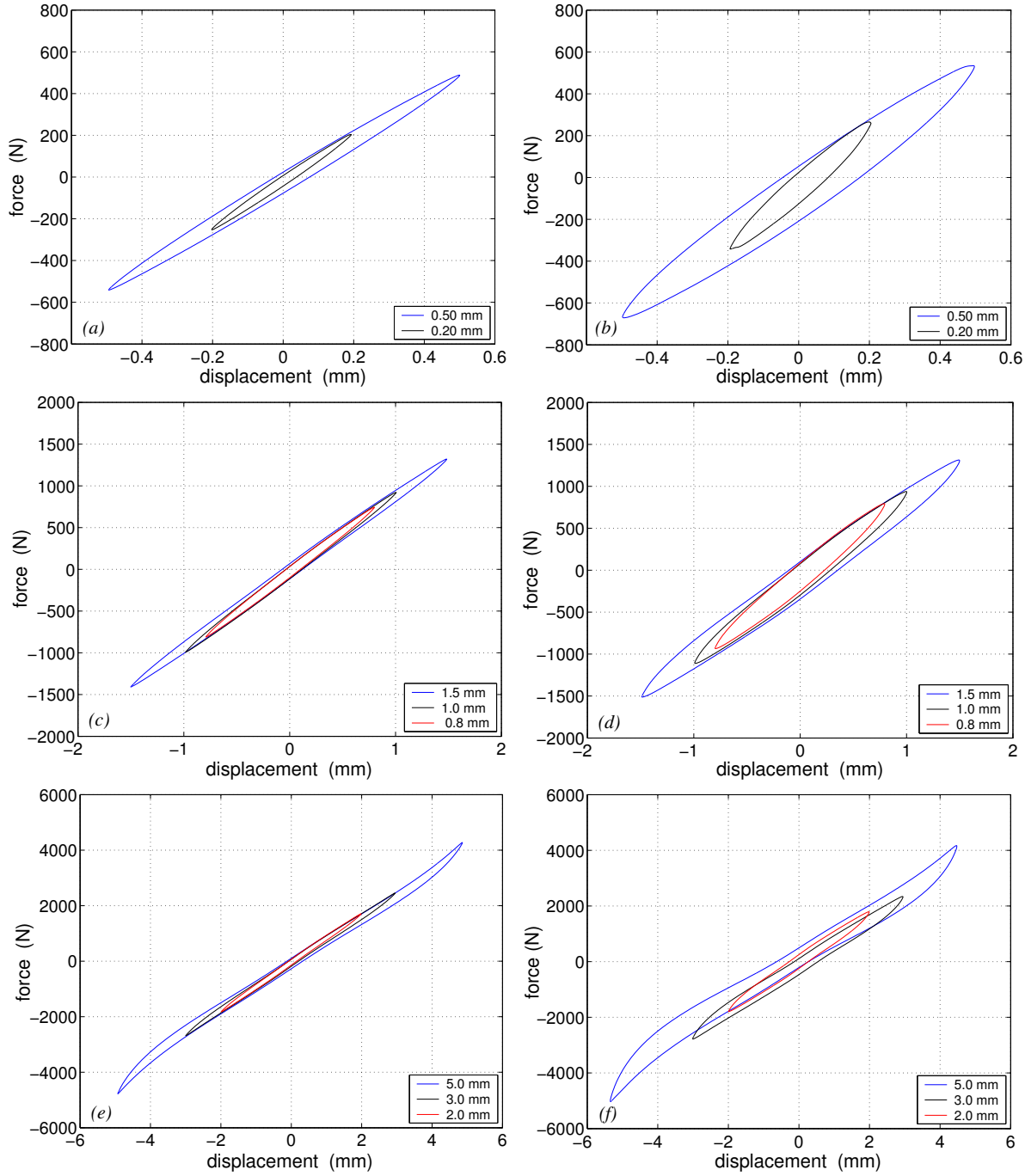

Figure 4.12: *Quasi-static characteristics for the cylindrical bushings. Hysteresis loops for some different amplitudes at 0.03 Hz. Low filled specimen C in (a), (c), and (e), and high filled specimen D in (b), (d), and (f).*

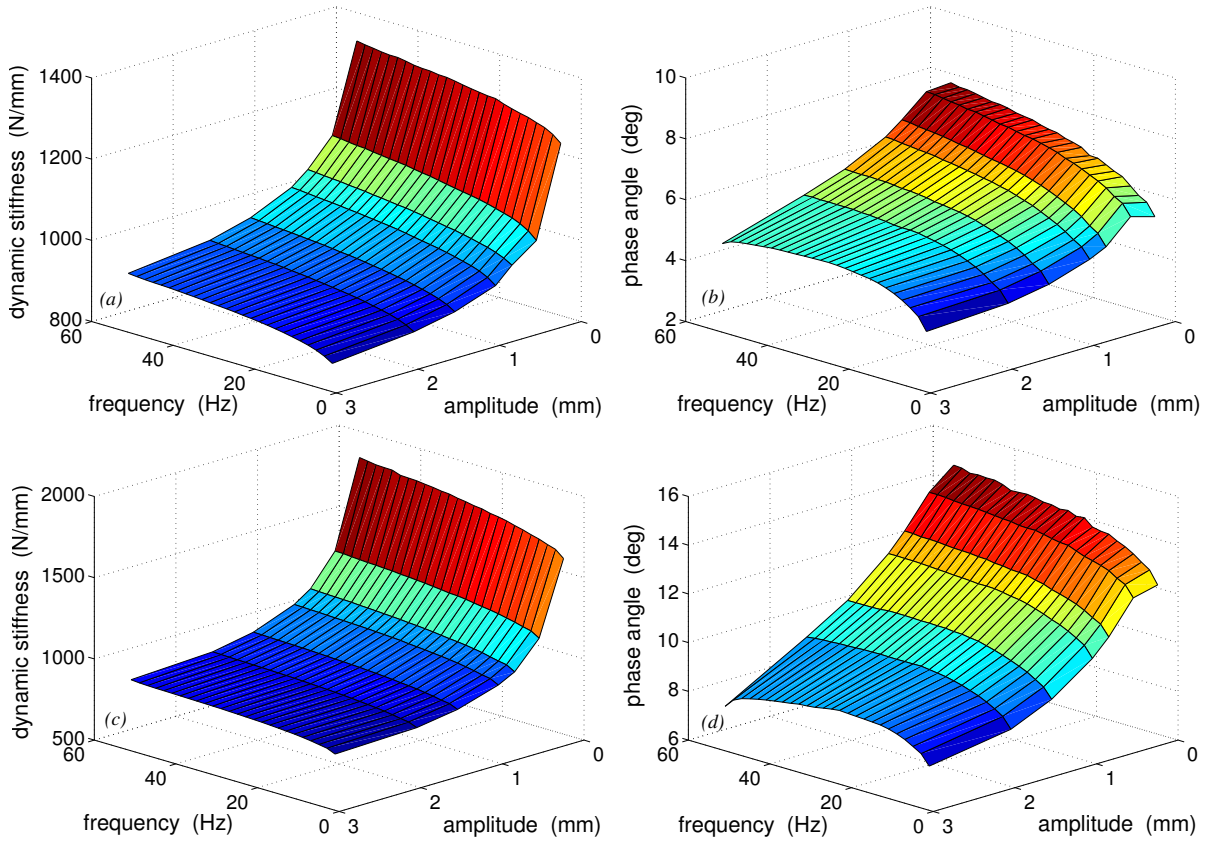

Figure 4.13: *Steady state harmonic dynamic characteristics for the cylindrical bushings. Dynamic stiffness and phase angle as function of amplitude and frequency. Low filled specimen C in (a) and (b), high filled specimen D in (c) and (d).*

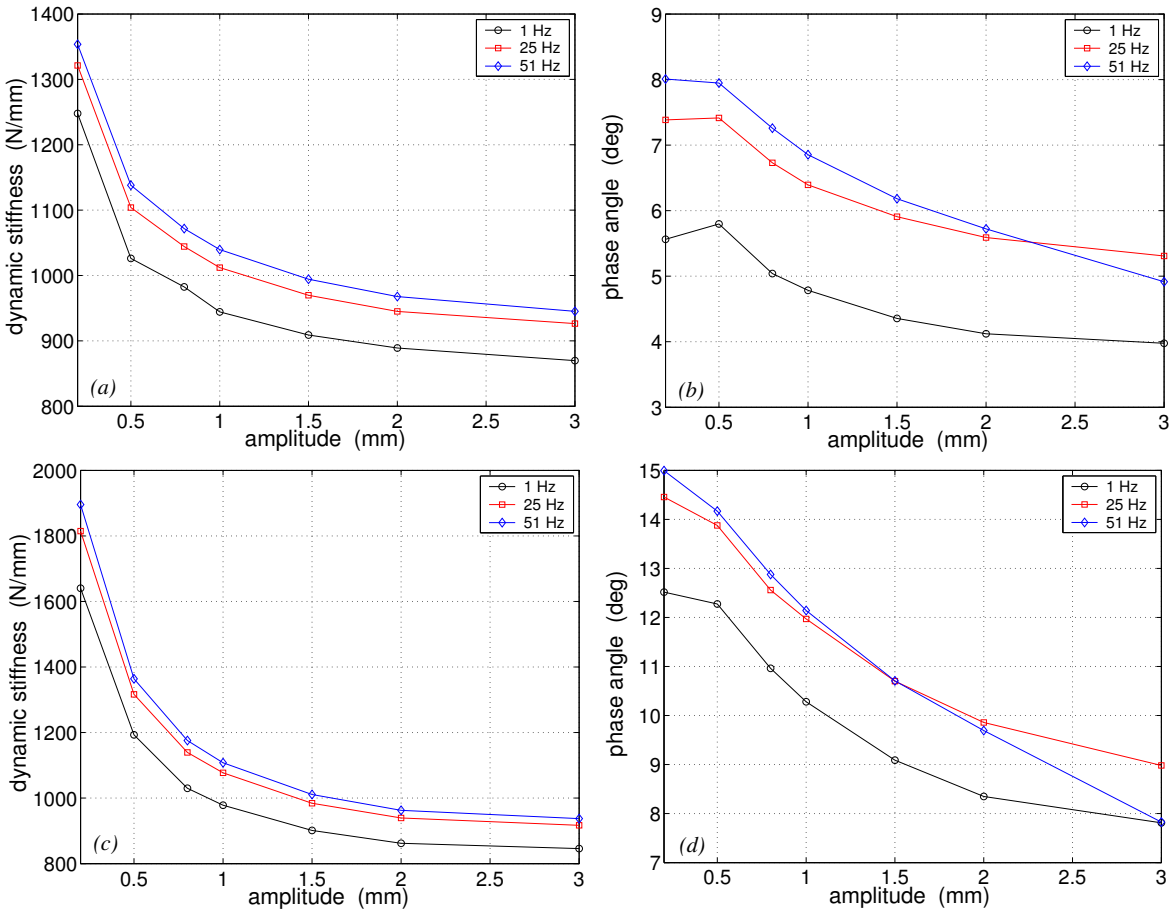

Figure 4.14: *Steady state harmonic dynamic characteristics for the cylindrical bushings. Dynamic stiffness and phase angle as function of amplitude for some specific frequencies (1, 25, and 51 Hz). Low filled specimen C in (a) and (b), high filled specimen D in (c) and (d).*

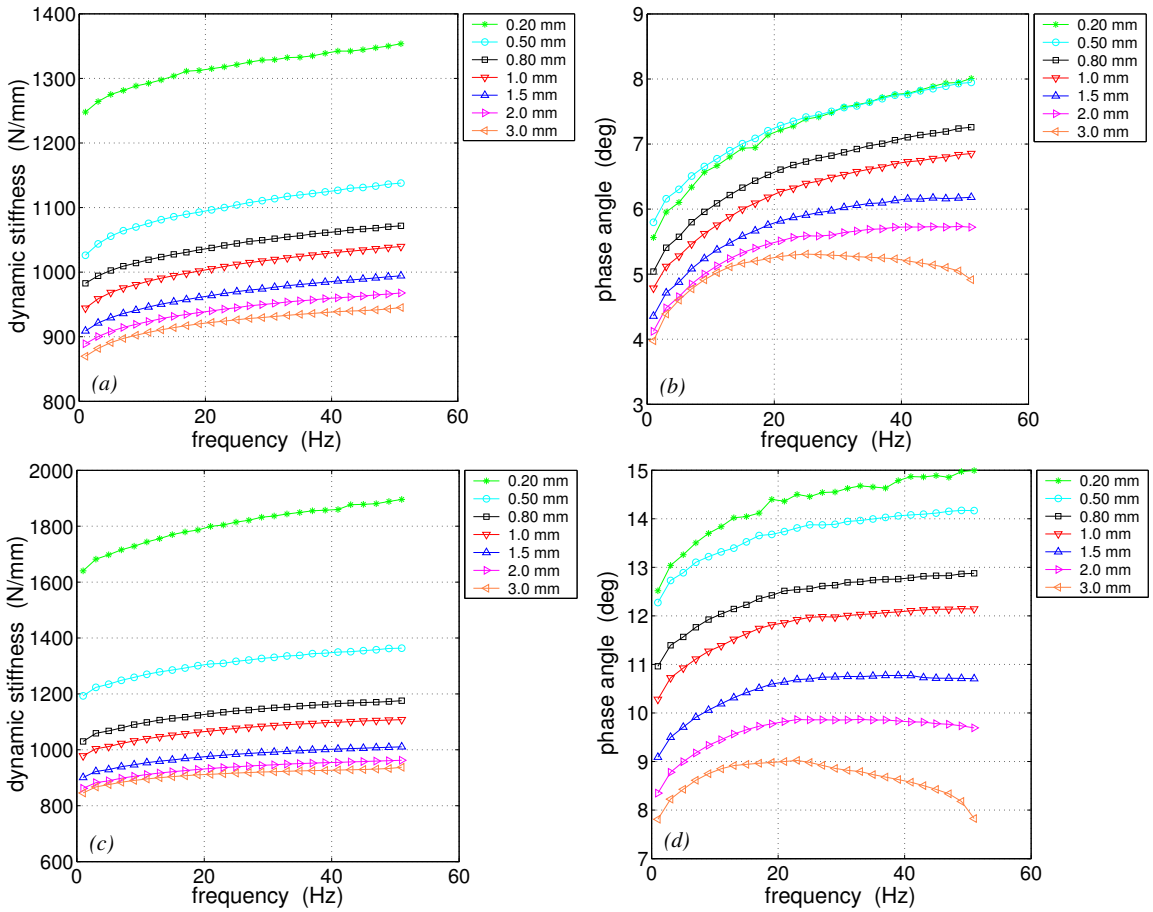

Figure 4.15: *Steady state harmonic dynamic characteristics for the cylindrical bushings. Dynamic stiffness and phase angle as function of frequency for different amplitudes. Low filled specimen C in (a) and (b), high filled specimen D in (c) and (d).*

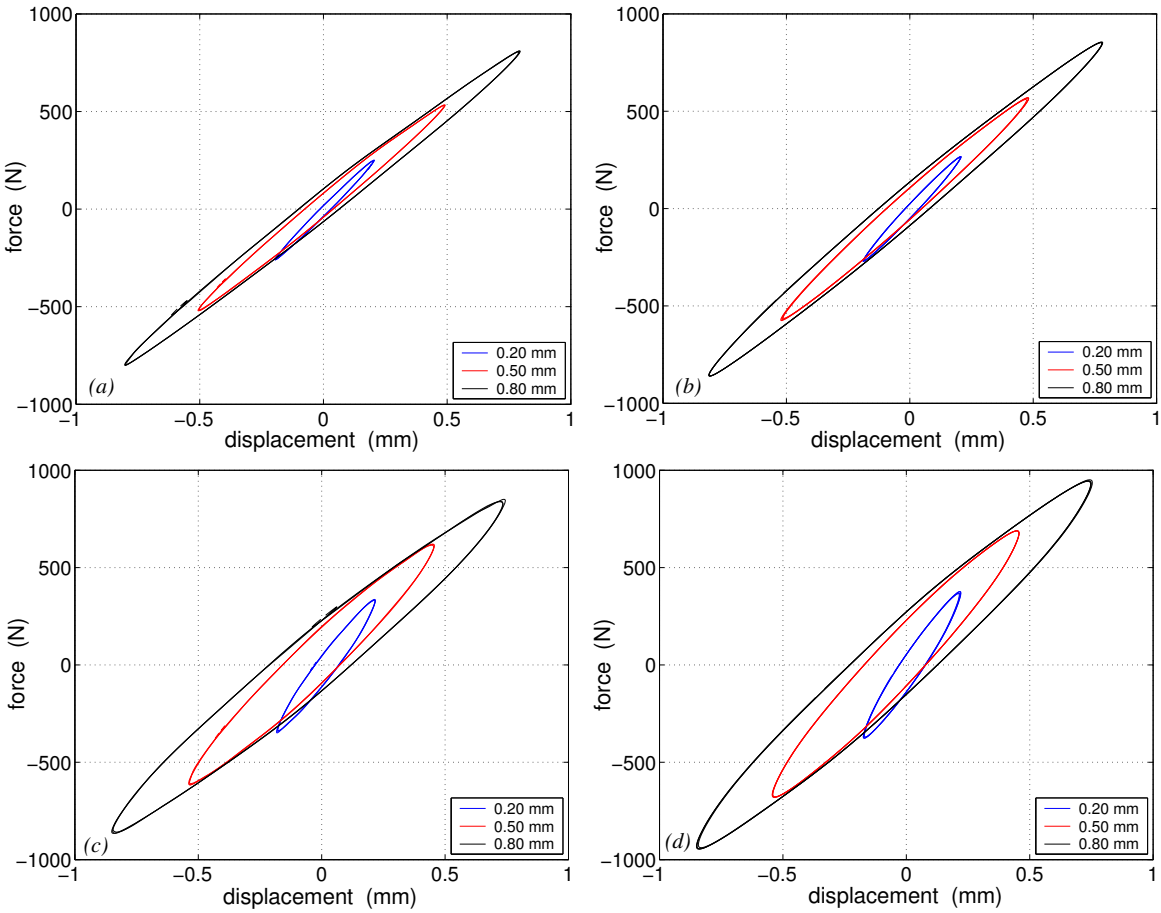

Figure 4.16: *Steady state harmonic dynamic characteristics for the cylindrical bushings. Hysteresis loops for some different amplitudes at 5 Hz ((a) and (c)) and at 51 Hz ((b) and (d)). Low filled specimen C in (a) and (b), high filled specimen D in (c) and (d).*

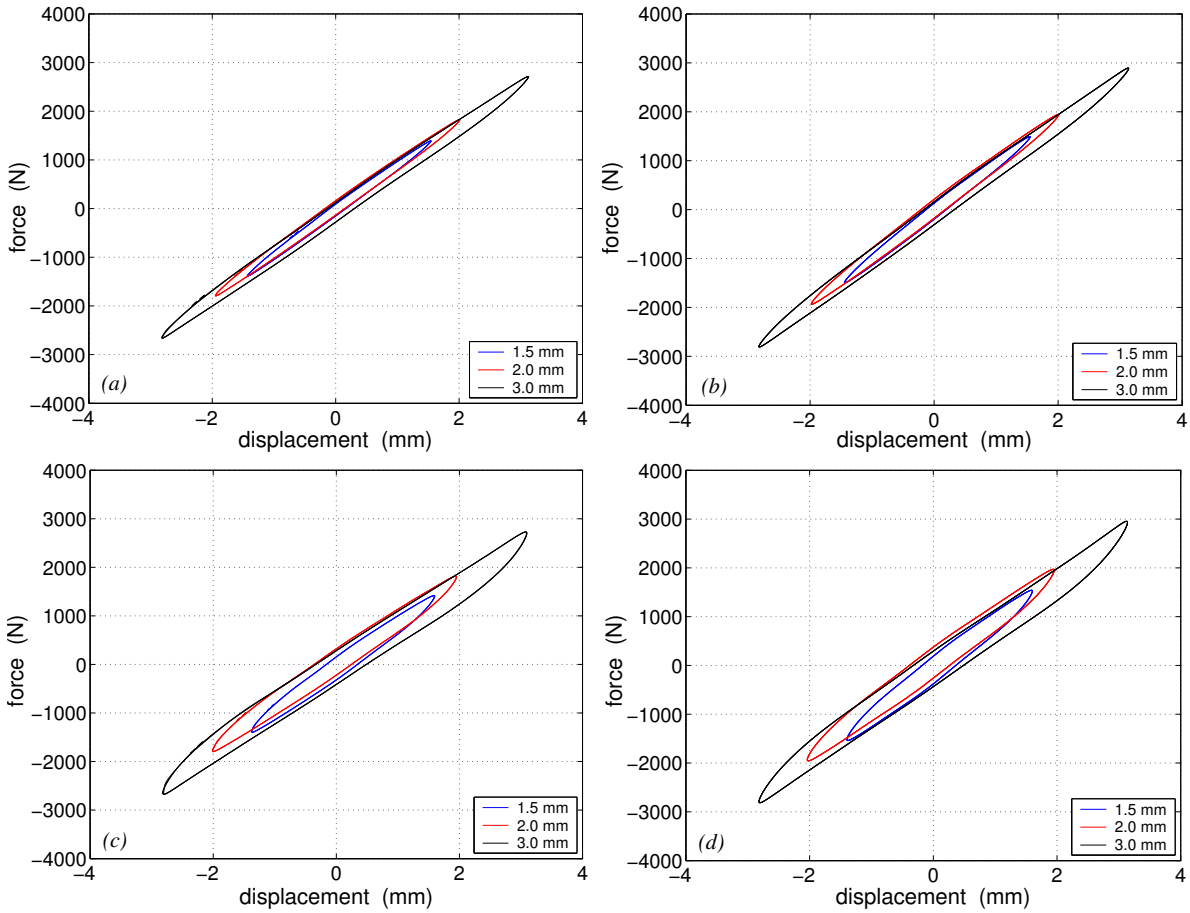

Figure 4.17: *Steady state harmonic dynamic characteristics for the cylindrical bushings. Hysteresis loops for some different amplitudes at 5 Hz ((a) and (c)) and at 51 Hz ((b) and (d)). Low filled specimen C in (a) and (b), high filled specimen D in (c) and (d).*

4.4.3 Hydrobushing

The hydrobushing (used in a Volvo car) is studied in this section. The results from the experiments are presented in the same manner as for the cylindrical bushings, i.e. the static tests are first presented, thereafter the quasi-static tests and finally the steady state harmonic dynamic tests. The tests are, as mentioned earlier, performed in radial direction.

Static tests

Static test results are given in Figure 4.18. Amplitude dependence in the form of frictional damping can be seen in Figure 4.18(a), where increasing amplitude gives decreasing stiffness. The amplitude dependence for large displacements in Figure 4.18(c) is due to non-linear elasticity.

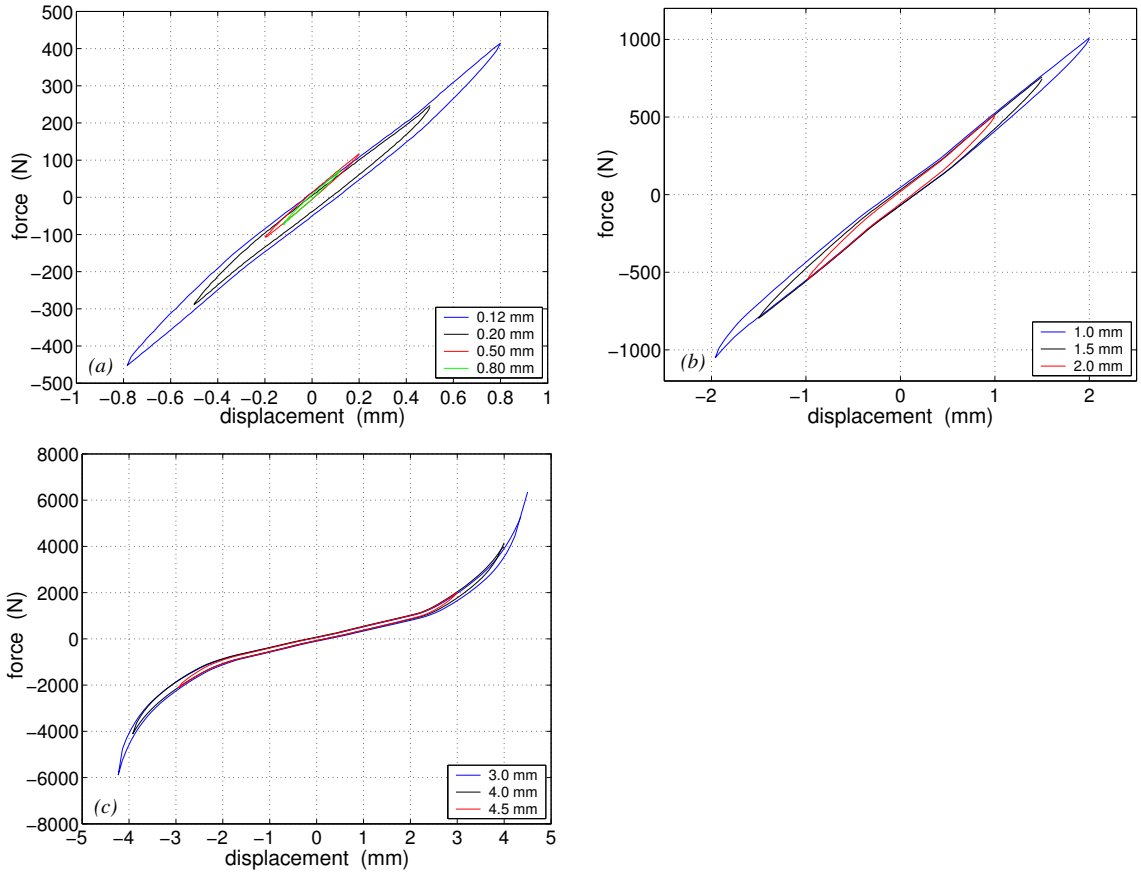

Figure 4.18: *Static characteristics for the hydrobushing.*

Quasi-static tests

Quasi-static test results are given in Figure 4.19. A weak amplitude dependence can be observed in Figure 4.19(a). The non-linearities after 2.0 mm displacement in Figure 4.19(b) are caused by non-linear elasticity.

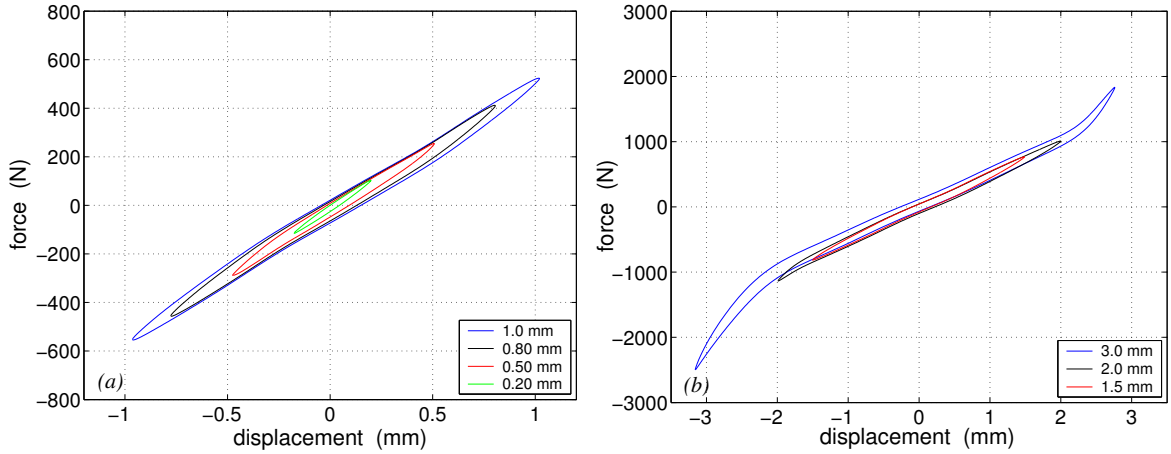

Figure 4.19: *Quasi-static characteristics for the hydrobushing. Hysteresis loops for some different amplitudes at 0.03 Hz.*

Steady state harmonic dynamic tests

The results are illustrated in the same manner as for the shear specimens and the cylindrical bushings, i.e. with 3-D plots first and thereafter 2-D plots to illustrate the amplitude and frequency dependence in more detail.

Dynamic stiffness and phase angle as function of amplitude and frequency are plotted in Figure 4.20. The amplitude and frequency dependence are different for the hydrobushing compared to the cylindrical bushings. The general dynamic behaviour of the cylindrical bushings is that dynamic stiffness and phase angle decrease with increasing amplitude, whereas they increase with increasing frequency. The hydrobushing is as earlier mentioned designed to give a high vibration isolation for low amplitudes (typically 0.10-0.20 mm) and a specific frequency (typically 15-20 Hz), see Figure 4.20(b) and 4.21(b).

The dynamic stiffness of the hydrobushing has a strong amplitude and frequency dependence for small amplitudes cf. Figure 4.20(a).

The maximum phase angle in Figure 4.20(b) is much higher than for the cylindrical bushings. The frequency dependence of the hydrobushing is shown in Figure 4.21. The dynamic stiffness and phase angle have a very strong frequency dependence for small amplitudes. Dynamic stiffness and phase angle as function of amplitude are given in Figure 4.22. The amplitude dependence of dynamic stiffness and phase angle is weak for higher amplitudes, especially for the dynamic stiffness, cf. Figure 4.22.

The dynamic characteristics of the hydrobushing have a very strong frequency dependence, which is logical since there is a fluid contained in it.

It has been concluded that the amplitude and frequency dependence of the shear specimens and cylindrical bushings are uncoupled. As for the hydrobushing, Figure 4.20 and 4.21 show that the amplitude and frequency dependence are coupled.

Hysteresis loops are plotted in Figure 4.23. The strong frequency dependence is clearly seen comparing Figure 4.23(a) to (b) and Figure 4.23(c) to (d).

The non-linearities in Figure 4.23(b) and (d) are mainly due to viscous damping, compare for example the hysteresis loop for 0.50 mm in Figure 4.23(a) to (b).

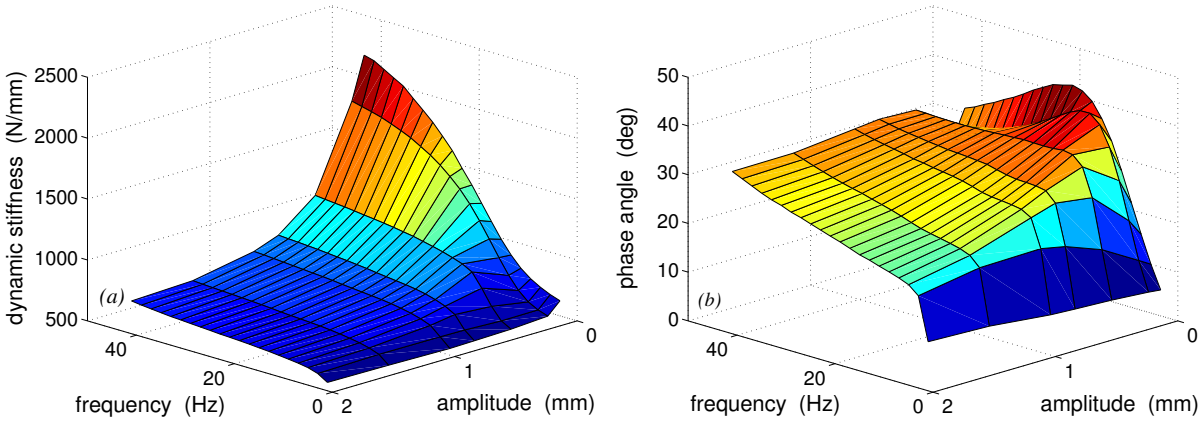

Figure 4.20: *Steady state harmonic dynamic characteristics for the hydrobushing. Dynamic stiffness and phase angle as function of amplitude and frequency.*

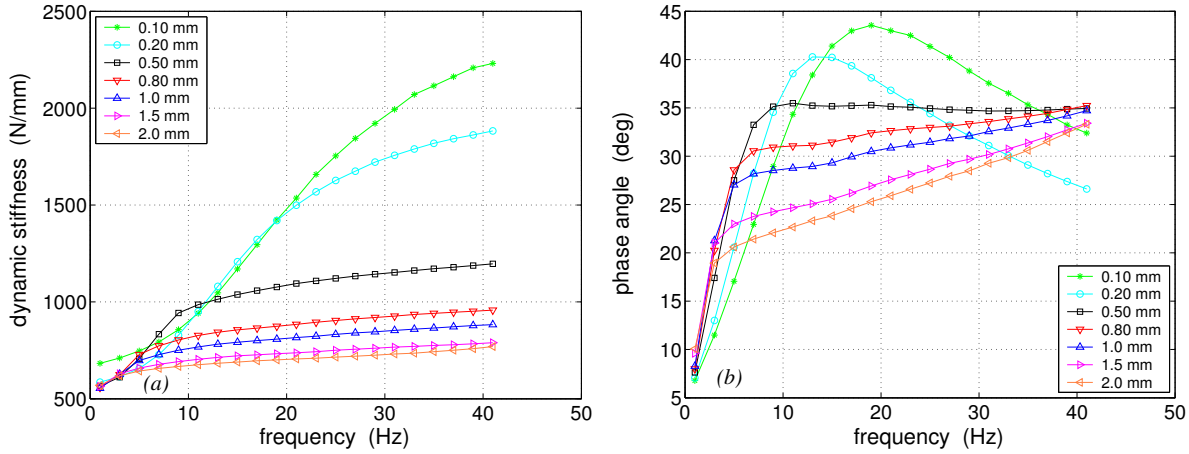

Figure 4.21: *Steady state harmonic dynamic characteristics for the hydrobushing. Dynamic stiffness and phase angle as function of frequency for different amplitudes.*

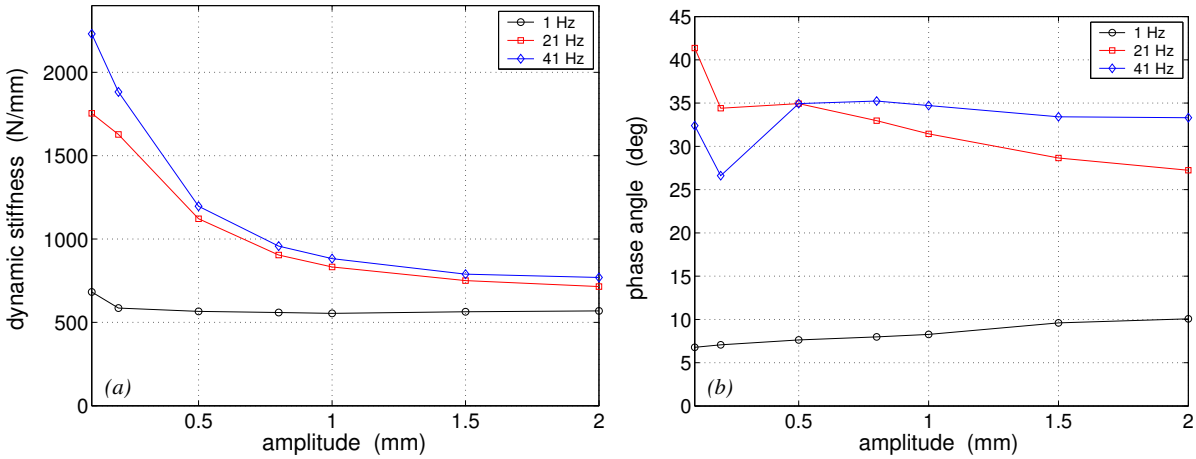

Figure 4.22: *Steady state harmonic dynamic characteristics for the hydrobushing. Dynamic stiffness and phase angle as function of amplitude for some specific frequencies (1, 21, and 41 Hz).*

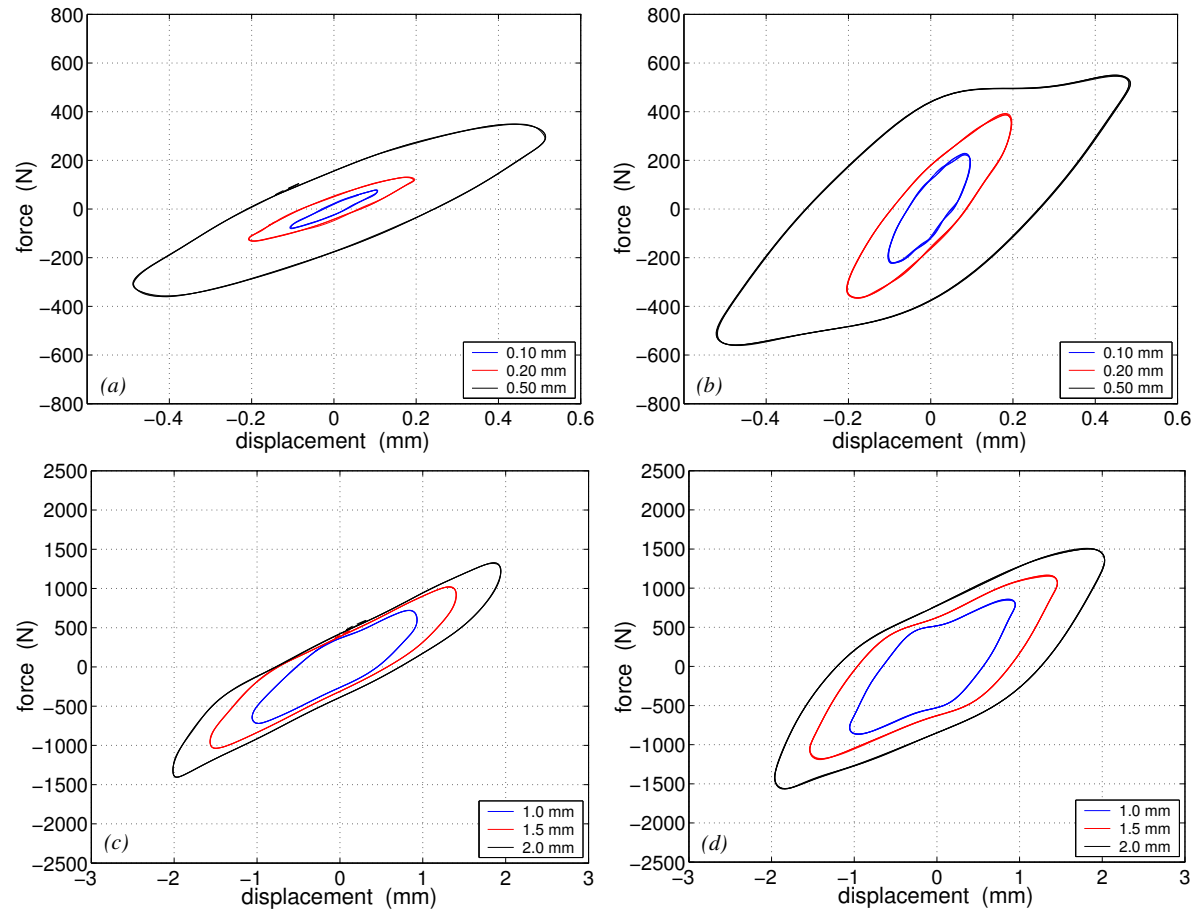

Figure 4.23: *Steady state harmonic dynamic characteristics for the hydrobushing. Hysteresis loops for some different amplitudes at 5 Hz ((a) and (c)) and at 41 Hz ((b) and (d)).*

4.4.4 Summary of experimental test results

Findings from the analysis of experimental data are listed in this section. Conclusions regarding the amplitude and frequency dependence, the rubber materials, and the specific components are drawn.

- High filled natural rubber has higher dynamic stiffness and phase angle than low filled natural rubber.
- High filled natural rubber has a stronger amplitude dependence than low filled natural rubber.
- All the components show amplitude and frequency dependence with respect to dynamic stiffness and phase angle.
- The general dynamic behaviour of the rubber components, i.e. shear specimens and cylindrical bushings, is that dynamic stiffness and phase angle decrease with increasing amplitude, whereas they increase with increasing frequency. (The phase angle increases with increasing amplitude for some low amplitudes).
- The hydrobushing consists of natural rubber and cavities partly filled with a fluid (glycol). It is designed to give a high vibration isolation for low amplitudes (typically 0.1-0.2 mm) and a specific frequency (typically 15-20 Hz), see Figure 4.20(b) and 4.21(b). The dynamic characteristics of the hydrobushing have a very strong frequency dependence, which is logical since there is a fluid in the bushing. The maximum damping (phase angle) for the hydrobushing is much higher than for the other components.
- The shear specimens are linear elastic up to about 100% shear strain and slightly non-linear elastic for higher strains. The cylindrical bushings and hydrobushing show a strong non-linear elastic behaviour for large displacements.
- The amplitude and frequency dependence of the rubber components, i.e. shear specimens and cylindrical bushings are uncoupled. However, the amplitude and frequency dependence are coupled for the hydrobushing.

Chapter 5

Fitting procedures

In order to obtain the unknown model parameters from experimental data an optimization approach is adopted. Optimization means searching for a minima or a maxima for a certain function in a certain interval with or without any specified constraints.

5.1 The optimization approach

The fitting procedure can be viewed as a minimization of the relative error of the component model compared to the experimental data. For this purpose an error function ϕ is established

$$\phi = \sum_{i=1}^{n}((\frac{K^i_{dyn,theor}}{K^i_{dyn,exp}} - 1)^2 + (\frac{d^i_{theor}}{d^i_{exp}} - 1)^2) \tag{5.1}$$

This function expresses the sum of the relative error of the component model compared to the experimental data. ϕ is a function of the unknown component parameters. To find a minima of the error function, already existing algorithms developed at Structural Mechanics (Lund University) [3] in *Matlab* have been used. In order to find the best fit, the error function ϕ has to be calculated repeatedly for all amplitudes and frequencies where measurements have been made.

Matlab uses iterative numerical methods to determine the minima of functions. The iterative methods start with assumed initial values. On the basis of the first values the search goes on for new values closer to the function minima. The multidimensional line search algorithm *fmincon* provided by the optimization tool-box in *Matlab* has been used to find the minimum of the error function (5.1).

The experimental data is evaluated for certain displacement pairs of angular frequency and displacement amplitude in sinusoidal displacement control i.e.

$$[(\omega_1, \hat{u}_1), \ldots, (\omega_n, \hat{u}_n)]$$

For every pair $(\omega_i, \hat{u}_i)$ the dynamic stiffness $K_{dyn,exp}$ and the phase angle δ_{exp} are

measured. That gives n values for $K_{dyn,exp}$ and n values for δ_{exp} i.e.

$$[K^1_{dyn,exp},\ \ldots\ , K^n_{dyn,exp}]$$

and

$$[\delta^1_{exp},\ \ldots\ , \delta^n_{exp}]$$

Further the function ϕ expresses the sum of the relative error of the component model compared to the experimental data, and certain values of the unknown component parameters will minimize the function ϕ. The relative error format (5.1) makes it possible to compare stiffness and loss angle although they are numerically of unequal magnitude, giving equal weight to stiffness and damping. Evaluating the unknown component parameters is therefore a pure optimization problem.

5.2 Generalized linear elastic viscoelastic elastoplastic model

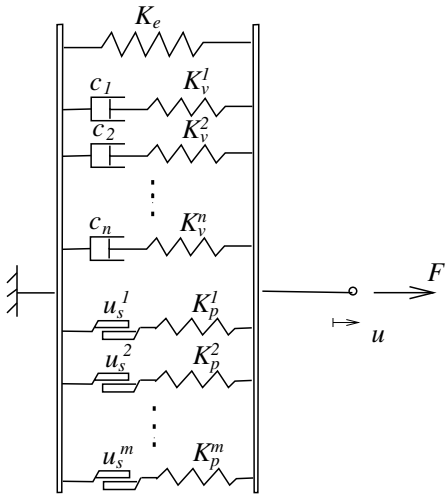

Figure 5.1: *Generalized linear elastic viscoelastic elastoplastic model.*

The generalized linear elastic viscoelastic elastoplastic model contains several Maxwell and basic frictional elements cf. Figure 5.1. This component model is able to model both frequency and amplitude dependent material behaviour. The error function for the viscoelastic and elastoplastic parts are discussed separetely in Appendix C.

5.2.1 Fitting algorithm

The analytical part of the following fitting algorithm (Table 5.1) is based on an analytical approximation (see next Section 5.2.2). The analytical approximation is based on an assumption that the dynamic stiffness can be expressed as the sum of

the constant elastic stiffness, the viscous stiffness, and the frictional stiffness and that the normalized damping can be expressed as a weighted sum of viscous and frictional damping. However, the poor accuracy of this approach yields a model with poor fit to experimental data. It turns out that the most correct way to simulate the component model is to use a time-stepping algorithm [3]. This is, however a time-consuming procedure, especially if the optimization algorithm is such that the error function ϕ needs to be evaluated repeatedly. For an increasing number of experimental data and component parameters this approach will be very slow compared to an analytical fitting approach. An efficient compromise between the two approaches is to use the analytical approach for repeated evaluations and to use the time stepping algorithm to calibrate the analytical expression with certain intervals. The evaluated $K^i_{dyn,theor}$ and d^i_{theor} according to the analytical approximation are used together with the evaluated $K^{num.i}_{dyn,theor}$ and $d^{num.i}_{theor}$ calculated from the time-stepping algorithm, (see section 5.2.3), to set up the following relations

$$corr^i_{dyn} = \frac{K^{num.i}_{dyn,theor}}{K^i_{dyn,theor}} \tag{5.2}$$

and

$$corr^i_{\delta} = \frac{d^{num.i}_{theor}}{d^i_{theor}} \tag{5.3}$$

Expression (5.2) and (5.3) are then used to calibrate the error function ϕ according to

$$\phi_{corr} = \sum_{i=1}^{k}((\frac{K^i_{dyn,theor} corr^i_{dyn}}{K^i_{dyn,exp}} - 1)^2 + (\frac{d^i_{theor} corr^i_{\delta}}{d^i_{exp}} - 1)^2) \tag{5.4}$$

The analytical part of the algorithm (Table 5.1) is then used again together with the modified error function ϕ_{corr} to obtain new component parameters. The new obtained component parameters will give a model with better fit to experimental data.

Experimental data is given as:

k denotes the number of measurements

$[(\omega_1, \hat{u}_1), (\omega_2, \hat{u}_2), \ldots, (\omega_k, \hat{u}_k)]$ $(rad/s,\ m)$

$[K^1_{dyn,exp}, K^2_{dyn,exp}, \ldots, K^k_{dyn,exp}]$ (N/m)

$[\delta^1_{exp}, \delta^2_{exp}, \ldots, \delta^k_{exp}]$ (rad)

Analytical part

search for the unknown component parameters > 0 *which will minimize the function* ϕ

$$\phi = \sum_{i=1}^{k}((\frac{K^i_{dyn,theor}}{K^i_{dyn,exp}} - 1)^2 + (\frac{d^i_{theor}}{d^i_{exp}} - 1)^2)$$

end Analytical part

Numerical part

from time-stepping algorithm compute

$$K^{num.i}_{dyn,theor} = \frac{\hat{F}_i}{\hat{u}_i}$$

$$d^{num.i}_{theor} = \frac{U^i_s}{\pi \hat{F}_i \hat{u}_i}$$

compute correction factors according to

$$corr^i_{dyn} = \frac{K^{num.i}_{dyn,theor}}{K^i_{dyn,theor}}$$

$$corr^i_d = \frac{d^{num.i}_{theor}}{d^i_{theor}}$$

end Numerical part

calibrated Analytical part

search for the unknown component parameters > 0 *which will minimize the function* ϕ_{corr}

$$\phi_{corr} = \sum_{i=1}^{k}((\frac{K^i_{dyn,theor} corr^i_{dyn}}{K^i_{dyn,exp}} - 1)^2 + (\frac{d^i_{theor} corr^i_d}{d^i_{exp}} - 1)^2)$$

end calibrated Analytical part

Table 5.1: *Algorithm to fit generalized linear elastic viscoelastic elastoplastic model to experimental data.*

5.2.2 Analytical approximation

Consider for instance a solid model represented by a spring, one Maxwell element, and one basic frictional element in parallel. Since the largest force for the total elastoplastic contribution does not occur at the same time as for the viscoelastic contribution, adding the contributions from all elements in the model becomes com-

plicated. Therefore two approximations are made when calculating dynamic stiffness and phase angle. The contribution to the dynamic stiffness in the complex plane including the frictional contribution can be approximately represented by the basic Fourier component of the response as an equivalent complex stiffness. This yields an interpretation of the total dynamic stiffness illustrated in Figure 5.2.

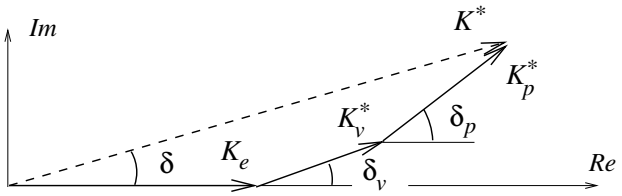

Figure 5.2: *The equivalent complex modulus including elastic, viscous, and frictional contributions.*

The total dynamic stiffness $K_{dyn} = |K^*|$ is the length of the vector in the complex plane and the length of $|K^*|$ can approximately be expressed as

$$K_{dyn} \approx K_e \cos(\delta) + K^v_{dyn}(\omega)\cos(\delta_v - \delta) + K^p_{dyn}(\hat{u})\cos(\delta_p - \delta) \tag{5.5}$$

by projections of each component. For reasonable values of the phase angle δ corresponding to, say $\delta < 0.4\ rad\ (\approx 23^o)$, the approximation $d = sin\,\delta \approx tan\,\delta \approx \delta$ and $cos\,\delta = 1$ can be used and the dynamic stiffness can approximately be expressed as a sum of elastic, viscous, and frictional stiffness

$$K_{dyn} \approx K_e + K^v_{dyn}(\omega) + K^p_{dyn}(\hat{u}) \tag{5.6}$$

i.e. the total dynamic stiffness is the sum of the constant elastic stiffness, the frequency dependent viscous stiffness, and the amplitude dependent frictional stiffness.

The damping is also found approximately from Figure 5.2 as

$$d = \sin(\delta) \approx \frac{K^v_{dyn}(\omega)\sin(\delta_v) + K^p_{dyn}(\hat{u})\sin(\delta_p)}{K_{dyn}} \tag{5.7}$$

i.e. the total normalized damping d can be expressed as a weighted sum of viscous and frictional damping. As it was mentioned above for reasonable values of the damping it is concluded that equation (5.7) also can be written as

$$d = sin(\delta) \approx \delta \approx \frac{K^v_{dyn}(\omega)\delta_v + K^p_{dyn}(\hat{u})\delta_p}{K_{dyn}} \tag{5.8}$$

The discussion above of the component model which only contains one Maxwell element and one basic frictional element is easily generalized to contain more than

one Maxwell and frictional element. For a solid model which contains n Maxwell elements and m basic frictional elements K_{dyn} is given as

$$K_{dyn} \approx K_e + K_{dyn}^{v.1}(\omega) + \ ... \ + K_{dyn}^{v.n}(\omega) + K_{dyn}^{p.1}(\hat{u}) + \ ... \ + K_{dyn}^{p.m}(\hat{u}) \tag{5.9}$$

and the total damping d as

$$d \approx \frac{K_{dyn}^{v.1}(\omega)\delta_v^1 + \ ... \ + K_{dyn}^{v.n}(\omega)\delta_v^n + K_{dyn}^{p.1}(\hat{u})\delta_p^1 + \ ... \ + K_{dyn}^{p.m}(\hat{u})\delta_p^m}{K_{dyn}} \tag{5.10}$$

Based on the above discussed analytical approximations, an analytical fitting approach for a generalized linear elastic viscoelastic elastoplastic model which contains one spring with constant stiffness K_e, n Maxwell element, and m basic frictional element in parallel (cf. Figure 5.1) is now discussed. As already mentioned, viscoelastic elastoplastic models are able to model both frequency and amplitude dependent material behaviour and therefore the experimental data are given as

$$\{(\omega_i, \hat{u}_i)\} = [(\omega_1, \hat{u}_1),\ (\omega_2, \hat{u}_2),\ \ldots, (\omega_k, \hat{u}_k)] \qquad (rad/s,\ m)$$

$$\{K_{dyn,exp}^i\} = [K_{dyn,exp}^1,\ K_{dyn,exp}^2,\ \ldots, K_{dyn,exp}^k] \qquad (N/m)$$

and

$$\{\delta_{exp}^i\} = [\delta_{exp}^1, \delta_{exp}^2,\ \ldots, \delta_{exp}^k] \qquad (rad)$$

Every pair of $(\omega_i, \hat{u}_i)$ corresponds to the measured $K_{dyn,exp}^i$ and δ_{exp}^i, the amplitude and frequency can therefore be chosen arbitrary.

In order to calculate the total dynamic stiffness $K_{dyn,theor}$ and damping d_{theor} for the entire model, dynamic stiffness and damping are calculated for each of the elements. Starting with the Maxwell element and making use of the derived expression for complex modulus E^* in Appendix B and making a transition from material level to structural level leads to

$$K_{v.j}^*(\omega) = K_v^j \frac{j\omega t_{r.j}}{1 + j\omega t_{r.j}} \tag{5.11}$$

where $t_{r.j} = c_j/K_v^j$. From Appendix B it is concluded that $|K_{v.j}^*(\omega)| = K_{dyn}^{v.j}(\omega)$ and $arg(K_{v.j}^*(\omega)) = \delta_v^j$ which give the following relations

$$K_{dyn}^{v.j}(\omega) = K_v^j \frac{\omega^2 t_{r.j}^2}{1 + \omega^2 t_{r.j}^2} \tag{5.12}$$

and

$$d_v^j = \sin(\delta_v^j) = \frac{1}{\sqrt{1 + \omega^2 t_{r.j}^2}} \tag{5.13}$$

Summing up the total dynamic contribution from all the viscoelastic elements j and the elastic element results in the following expression

$$K_{dyn}^{v} = \sqrt{(K_e + \sum_{j=1}^{n} K_{dyn}^{v.j} \cos(\delta_v^j))^2 + (\sum_{j=1}^{n} K_{dyn}^{v.j} \sin(\delta_v^j))^2} \tag{5.14}$$

where δ_v^j is the phase angle according to equation (5.13). In a similar manner the total viscous damping can be expressed as

$$d_v = \sin(\delta_v) = \frac{1}{K_{dyn}^{v}} \sum_{j=1}^{n} \frac{K_{dyn}^{v.j}}{\sqrt{1 + \omega^2 t_{r.j}^2}} \tag{5.15}$$

The behaviour of the basic frictional element q depends on whether it is plastic or not, i.e. whether the displacement $\hat{u}$ is larger than the yield displacement u_s^q. From Section C.2.1 it is concluded that the dynamic stiffness in a basic frictional element q can be expressed as

$$K_{dyn}^{p.q} = \begin{cases} \frac{K_p^q u_s^q}{\hat{u}} & \text{if } u_s^q < \hat{u} \\ K_p^q & \text{otherwise} \end{cases} \tag{5.16}$$

and the hysteretic work is given by

$$U_s^q = \begin{cases} 4K_p^q u_s^q (\hat{u} - u_s^q) & \text{if } u_s^q < \hat{u} \\ 0 & \text{otherwise} \end{cases} \tag{5.17}$$

Summing up the total dynamic contribution from all elastoplastic elements q results in the following expression

$$K_{dyn}^{p} = \sum_{q=1}^{m} K_{dyn}^{p.q} \tag{5.18}$$

The total plastic damping is calculated according to

$$d_p = \sin(\delta_p) = \frac{\sum_{q=1}^{m} U_s^q}{\pi \hat{u} \sum_{q=1}^{m} K_p^q u_s^q} \tag{5.19}$$

As already discussed two approximations were introduced in order to calculate the dynamic stiffness and damping for a generalized linear elastic viscoelastic elastoplastic model. The total dynamic stiffness can approximately be expressed as the sum of the constant elastic stiffness, the frequency dependent viscous stiffness, and the amplitude dependent frictional stiffness. The normalized damping can approximately be expressed as a weighted sum of viscous and frictional damping. Combining the two approximations (5.9) and (5.10) gives the following expressions for the theoretical dynamic stiffness and normalized damping for every measurement i

$$K_{dyn,theor}^{i} \approx K_{dyn}^{v.i} + K_{dyn}^{p.i} \tag{5.20}$$

$$d^i_{theor} = \sin(\delta^i_{theor}) \approx \frac{K^{v.i}_{dyn}\sin(\delta^i_v) + K^{p.i}_{dyn}\sin(\delta^i_p)}{K^i_{dyn,theor}} \tag{5.21}$$

Note that $K^{v.i}_{dyn}$ also contains the elastic contribution K_e.
Using equation (5.20) and equation (5.21) it is now possible to evaluate the approximative error function ϕ. The unknown component parameters are then obtained from the analytical part of the algorithm (Table 5.1).

5.2.3 Numerical evaluation

A time-stepping algorithm for the Maxwell element can be found in Chapter 2 Section 2.2. For small time steps Δt and using an approximation according to the trapezoidal rule, the force for the viscoelastic element j can be expressed in an incremental form as

$$\Delta F^v_j = F^v_j(e^{-\Delta t_i/t^j_r} - 1) + \frac{K^j_v \Delta u_i}{2}(1 + e^{-\Delta t_i/t^j_r}) \tag{5.22}$$

A time-stepping algorithm for the basic frictional element can be found in Chapter 2 Section 2.4, and it is concluded that the force for the elastoplastic element q can be expressed in the following incremental form

$$\Delta F^p_q = \begin{cases} K^q_p \Delta u_i & \text{if elastic} \\ 0 & \text{otherwise} \end{cases} \tag{5.23}$$

The total incremental force for the whole generalized linear elastic viscoelastic elastoplastic model is then obtained by adding all incremental force contributions from all elements for the time-step Δt_i i.e.

$$\Delta F_i = K_e \Delta u_i + \sum_{j=1}^{n} \Delta F^v_j + \sum_{q=1}^{m} \Delta F^p_q \tag{5.24}$$

The total force for the whole model is then obtained from

$$\begin{aligned} &i = 1, 2, 3 \ldots \\ &\quad \Delta F_i = K_e \Delta u_i + \textstyle\sum_{j=1}^{n} \Delta F^v_j + \sum_{q=1}^{m} \Delta F^p_q \\ &\quad F_i = F_{i-1} + \Delta F_i \end{aligned} \tag{5.25}$$

With knowledge of the applied displacement history together with the evaluated component parameters from the analytical part of the algorithm (Table 5.1) it is possible to calculate the dynamic stiffness and damping from (5.25) according to

$$K^{num.i}_{dyn,theor} = \frac{\hat{F}_i}{\hat{u}_i} \tag{5.26}$$

and

$$d_{theor}^{num.i} = \sin(\delta_{theor}^{num.i}) = \frac{U_s^i}{\pi \hat{F}_i \hat{u}_i} \tag{5.27}$$

where index num denotes quantities evaluated based on (5.25). Hence, the error function ϕ_{corr} can be numerically evaluated.

5.3 Modified fitting procedure for non-linear behaviour

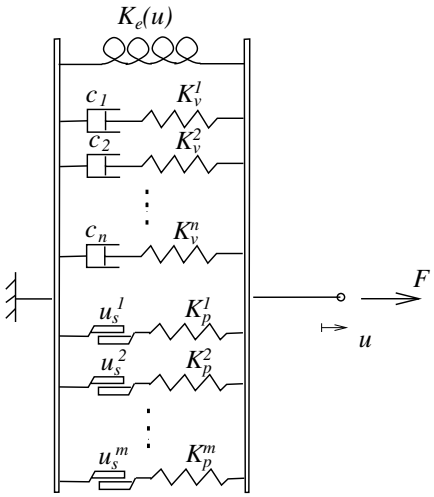

Figure 5.3: *Generalized non-linear viscoelastic elastoplastic model.*

The applied amplitude $\hat{u}$ is larger in the static and quasi-static tests than in the steady state harmonic dynamic tests, see Chapter 4. The largest amplitudes in the static and quasi-static tests give rise to a non-linear behaviour, as can be seen in the hysteresis loops in Chapter 4.

The generalized linear elastic viscoelastic elastoplastic model is unable to model such behaviour. It is therefore necessary to replace the spring with constant stiffness K_e by a non-linear spring with stiffness $K_e(u)$, i.e. the stiffness is a function of the applied displacement. However, it is concluded in Chapter 4 that the amplitudes in the dynamic tests are not large enough to show any non-linear elastic behaviour. The static or quasi-static tests are however conducted with an amplitude large enough to show non-linear elastic behaviour.

5.3.1 Correction for the non-linear elastic behaviour

A method to take the non-linear elastic behviour into account is presented. The method is based on experimental data that fulfil the above discussion concerning large displacement amplitudes.

First step

A generalized linear elastic viscoelastic elastoplastic model fitted to experimental data obtained from a dynamic test gives values of K_e, $K_v^1, \ldots, K_v^n$, $c_1, \ldots, c_n$, $K_p^1, \ldots, K_p^m$, and $u_s^1, \ldots, u_s^m$ where n denotes the number of Maxwell element and m denotes the number of basic frictional element that have been used. In order

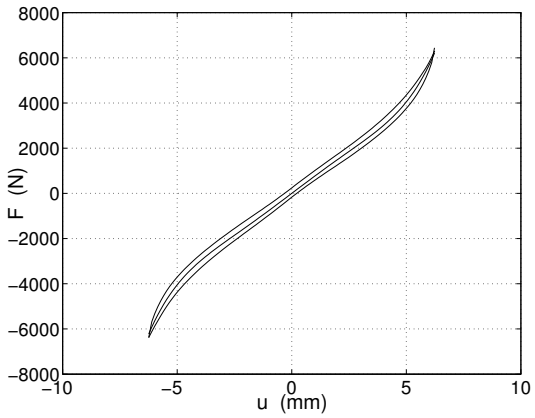

Figure 5.4: *The middle curve is the mean shape* $F_{mean}(u_{mean})$.

to capture the non-linear elastic behaviour, the mean shape $F_{mean} = F_{mean}(u_{mean})$ is used cf. Figure 5.4 where the mean shape $F_{mean}(u_{mean})$ is the middle curve.

Second step

The next step is to find a force-displacement relation according to $f = K_e(u)u$. Make use of the force-displacement relationship (3.3) in Chapter 3 Section 3.2 which is a theoretical expression for the mean shape according to Figure 5.4. Equation (3.3) can also be expressed in matrix notation, i.e.

$$F_{theor} = [2u\ 4u^3\ 6u^5][D_{10}\ D_{20}\ D_{30}]^T \tag{5.28}$$

The main task is to find D_{10}, D_{20}, and D_{30} such that

$$F^i_{theor} = [2u_{mean.i}\ 4u^3_{main.i}\ 6u^5_{mean.i}][D_{10}\ D_{20}\ D_{30}]^T \approx F^i_{mean} \tag{5.29}$$

or

$$\mathbf{F}_{theor} = \mathbf{Ad} \approx \mathbf{F}_{mean} \tag{5.30}$$

Equation (5.30) is an overdetermined system of equations which can be solved by using the operation

$$\mathbf{A}^T\mathbf{Ad} \approx \mathbf{A}^T\mathbf{F}_{mean} \tag{5.31}$$

This operation transforms the overdetermined system of equations to an ordinary system of equations with three equations and three unknowns and the D-constants are computed according to

$$\mathbf{d} = (\mathbf{A}^T\mathbf{A})^{-1}\mathbf{A}^T\mathbf{F}_{mean} \tag{5.32}$$

The obtained D-constants are constants which give the best fit according to equation (5.30) in a least squares sense.

With the evaluated D-constants from equation (5.32) the following relations are obtained

$$A = \frac{D_{20}}{D_{10}}\ \ and\ \ B = \frac{D_{30}}{D_{10}} \tag{5.33}$$

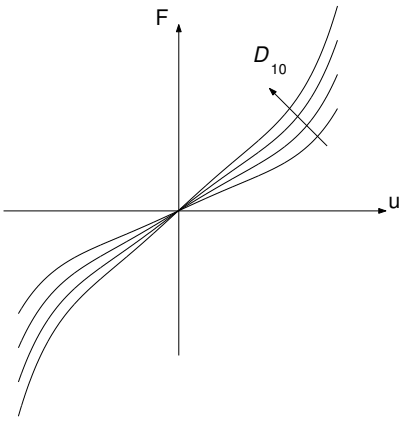

Figure 5.5: *The dependence on D_{10} of the curve shape. Larger value of D_{10} gives a stiffer material.*

Hence, the shape of the middle curve in Figure 5.4 is remained also when D_{10} is multiplied by other values, i.e. $D_{20} = D_{10}A$ and $D_{30} = D_{10}B$. The dependence on D_{10} of the curve shape is illustrated in Figure 5.5.

Third step

The force-displacement relationship is according to equation (3.3). For small displacements the equation (3.3) can approximately be written as

$$F_{theor} \approx 2D_{10}u \tag{5.34}$$

From equation (5.34) it is concluded that a good approximation for D_{10} is

$$D_{10} \approx \frac{K_e}{2} \tag{5.35}$$

where K_e is the stiffness according to a generalized linear elastic viscoelastic elasto-plastic model fitted to experimental data obtained from a dynamic test. The spring with the constant stiffness K_e in the generalized linear elastic viscoelastic elasto-plastic model is now replaced with a non-linear spring with stiffness $K_e(u)$, i.e.

$$K_e(u) = K_e + 4AD_{10}u^2 + 6BD_{10}u^4 \tag{5.36}$$

where $D_{10} = K_e/2$, A and B according to (5.33).

Forth step

The time-stepping algorithm (5.25) in Section 5.2.3 is then modified according to

$$\begin{aligned} &i = 1, 2, 3 \ldots \\ &\Delta F_i = (K_e + 4AD_{10}\Delta u_i^2 + 6BD_{10}\Delta u_i^4)\Delta u_i + \textstyle\sum_{j=1}^{n} \Delta F_j^v + \sum_{q=1}^{m} \Delta F_q^p \\ &F_i = F_{i-1} + \Delta F_i \end{aligned} \tag{5.37}$$

A generalized non-linear elastic viscoelastic elastoplastic model obtained by this method is validate by comparing theoretical force-displacement curves created by the modified time-stepping algorithm (5.37) to experimental force-displacement curves.

5.4 Changing weight between stiffness and damping

As already discussed, the fitting procedure can be viewed as a minimization of the relative error of the component model compared to the experimental data. For this purpose an error function ϕ was proposed.

$$\phi = \sum_{i=1}^{n} (k(\frac{K^i_{dyn,theor}}{K^i_{dyn,exp}} - 1)^2 + (1-k)(\frac{d^i_{theor}}{d^i_{exp}} - 1)^2) \tag{5.38}$$

In the above expression the factor k is introduced. By choosing the scale factor k, it is possible to decide whether to emphasize a correct modelling of the dynamic stiffness K_{dyn} or a correct modelling of the damping d.

Chapter 6

Validation

The one dimensional models presented in Chapter 2 and Appendix B are validated for static, quasi-static, and steady state harmonic dynamic loading in this chapter. The model behaviour for the shear specimens, the cylindrical bushings, and the hydrobushing have been validated. Three viscoelastic models have been validated, namely Kelvin-Voigt, Zener, and generalized Maxwell. However, the main validation concerned the generlized viscoelastic elastoplastic (viscoplastic) model. The viscoelastic models are, as mentioned in Appendix B, unable to capture the inelastic amplitude dependence (frictional damping) of natural rubber. They are as a consequence of that only briefly evaluated. The generalized viscoelastic elastoplastic model is more carefully evaluated since it captures both the amplitude and frequency dependence.

6.1 Expectation on the validation

It was concluded in Chapter 4 that the evaluated components are amplitude and frequency dependent. The amplitude and frequency dependence are uncoupled for the rubber components (i.e. shear specimens and cylindrical bushings) and coupled for the hydrobushing. None of the validated models has coupled amplitude and frequency dependence, i.e. the behaviour of the hydrobushing can not be captured. The viscoelastic models lack the ability to model inelastic amplitude dependence (frictional damping) and are therefore expected to correlate poorly. The generalized viscoelastic elastoplastic model is however expected to correlate well for the shear specimens and cylindrical bushings [3].

6.2 Validation method

Calculated and measured hysteresis loops for different amplitudes and frequencies have been plotted and compared. Identity of hysteresis loops gives identical dynamic stiffness and phase angle, but the inverse is not necessarily true. An adequate way to evaluate the behaviour of the models is thus to compare measured and

calculated hysteresis loops. Moreover have the dynamic stiffness and phase angle been validated. Measured and calculated values for dynamic stiffness and phase angle have been compared in 2-D and 3-D plots. The 2-D plots show dynamic stiffness and phase angle as function of frequency for some specific amplitudes. An overview of the validation is given in Table 6.1.

	Static behaviour	Quasi-static behaviour	Steady state harmonic dynamic behaviour
Shear specimens Viscoelastic models:			-2-D plots of dynamic stiffness and phase angle
Generalized viscoelastic elastoplastic model:	-Hysteresis loops		-Hysteresis loops -2-D plots of dynamic stiffness and phase angle -3-D plots of dynamic stiffness and phase angle
Cylindrical bushings Viscoelastic models:			-2-D plots of dynamic stiffness and phase angle
Generalized viscoelastic elastoplastic model:	-Hysteresis loops	-Hysteresis loops	-Hysteresis loops -2-D plots of dynamic stiffness and phase angle -3-D plots of dynamic stiffness and phase angle
Hydrobushing Viscoelastic models:			
Generalized viscoelastic elastoplastic model:			-Hysteresis loops -2-D plots of dynamic stiffness and phase angle -3-D plots of dynamic stiffness and phase angle

Table 6.1: *Validation of the viscoelastic models and the viscoelastic elastoplastic model.*

6.3 Validation results

The validation results are presented and discussed in this section. The double shear specimens are first validated, thereafter the cylindrical bushings and finally the hydrobushing. The double shear specimens and the cylindrical bushings have been modelled by viscoelastic models and the generalized non-linear elastic viscoelastic elastoplastic model. The generalized linear elastic viscoelastic elastoplastic model has been used for the hydrobushing.

6.3.1 Double shear specimens

The models of shear specimen A and B are validated in this section. In Chapter 4 it was concluded that the amplitudes 0.012 and 0.030 mm were unsuccessfully measured. These amplitudes are consequently not used in the validation. The viscoelastic models are first discussed and then the generalized non-linear elastic viscoelastic elastoplastic model.

Viscoelastic models

Three viscoelastic models (i.e. amplitude independent) are validated with measurements in Figure 6.1, namely Kelvin-Voigt, Zener, and generalized Maxwell. The Kelvin-Voigt and Zener model are fitted to the measured data with the use of Matlab function fmins, whereas the generalized Maxwell model is fitted with fmincon [3]. The viscoelastic models are unable to describe amplitude dependence and are therefore fitted to the mean value of the dynamic stiffness and the phase angle for the largest and smallest amplitude.

Figure 6.1 shows that the calculated and measured responses correlate poorly. The Kelvin-Voigt model gives an almost constant dynamic stiffness as function of frequency and a phase angle linearly dependent of frequency. The linear relationship between phase angle and frequency is seen in the equation $tan(\delta) = \frac{\eta}{E}\omega$ which is discussed in Appendix B. The Zener model underestimates the dynamic stiffness for low frequencies and overestimates the dynamic stiffness for high frequencies. Just as the Kelvin-Voigt model is the Zener model unable to capture the frequency dependence of the phase angle. The generalized Maxwell model describes the frequency dependence of the dynamic stiffness and phase angle fairly well with respect to the mean value. The fitting curve for the generalized Maxwell model in Figure 6.1(b) and (d) can be understood to be discontinuous. This is a phenomena from the plotting, smaller frequency step will give continuous curves, i.e. the model is continuous. The viscoelastic model that describes the behaviour of the shear specimens most accurate is the generalized Maxwell model.

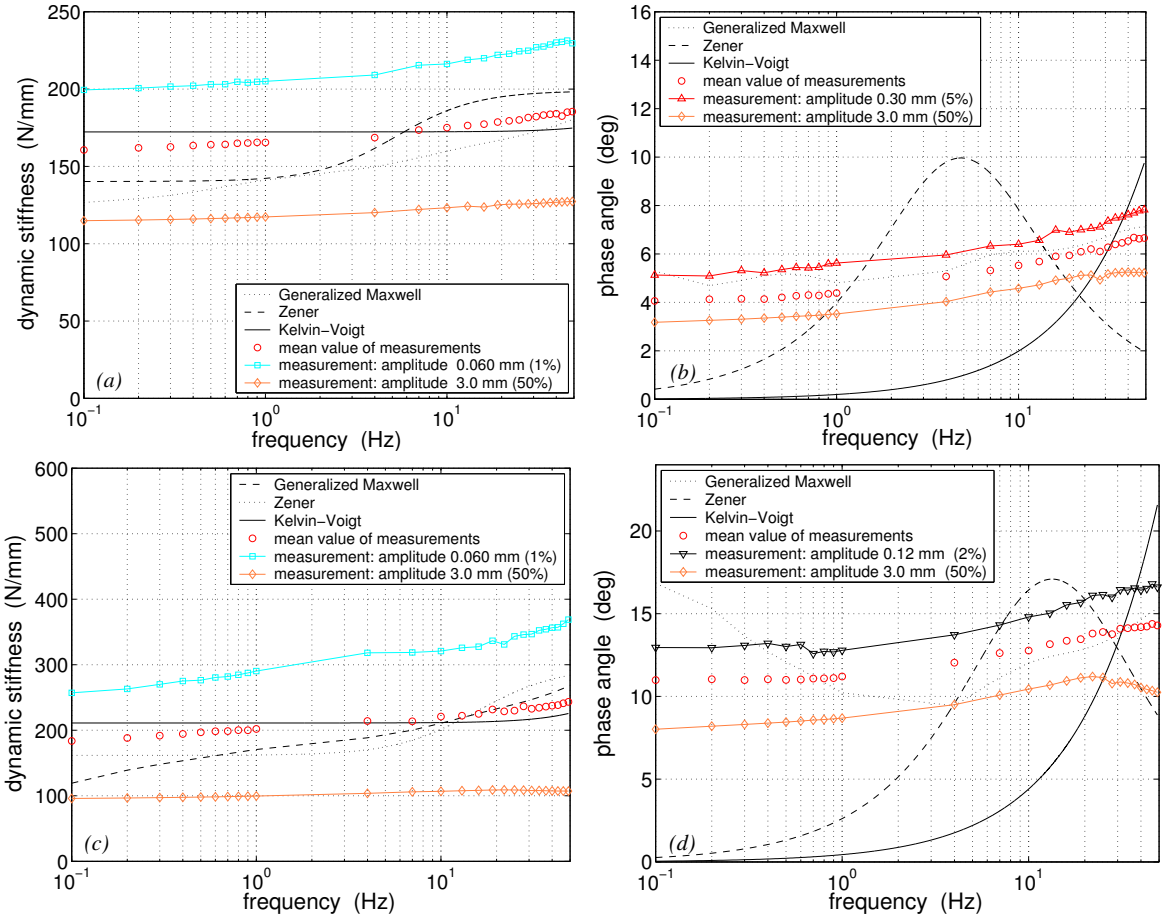

Figure 6.1: *Validation of the viscoelastic models of the double shear specimens for steady state harmonic dynamic behaviour. Low filled specimen A in (a) and (b), high filled specimen B in (c) and (d). The generalized Maxwell model of specimen A and B has five and four elements respectively.* ***Note:*** *The generalized Maxwell models have the phase angle 0 degrees at 0 Hz. It is first at 0.1 Hz that the phase angle has the value that is shown in (b) and (d). Corresponding shear strain is given for each amplitude.*

Generalized non-linear elastic viscoelastic elastoplastic model

The static behaviour is first validated and then the harmonic dynamic behaviour. Shear specimen A has been modelled by three Maxwell and four frictional elements, whereas shear specimen B has been modelled by one Maxwell and four frictional elements. It is possible to get more accurate models by increasing the number of elements, but the improvement is hardly noticeable. The relative error *(err)* as function of number of Maxwell and frictional elements is plotted in Figure 6.2. The relative error *(err)* is defined as

$$err = \frac{1}{n}\sqrt{\phi} \tag{6.1}$$

ϕ is defined in equation (5.1) and n is the number of measured points.

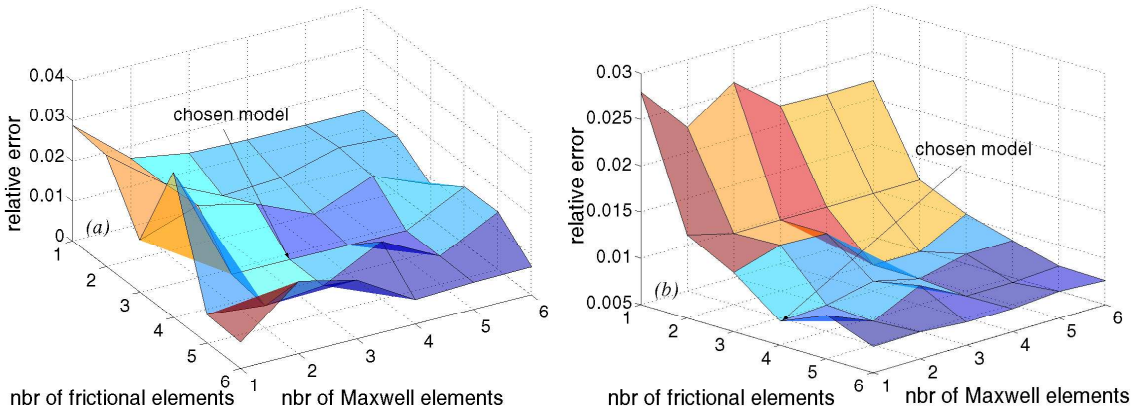

Figure 6.2: *Relative error as function of number of frictional and Maxwell elements. The relative error is established from steady state harmonic dynamic tests. Low filled specimen A in (a) and high filled specimen B in (b).*

Static behaviour

The generalized non-linear elastic viscoelastic elastoplastic model describes the overall static behaviour of specimen A and B in a satisfying manner, see Figure 6.3. The hysteresis loops with linear elastic behaviour are calculated very accurately, whereas the hysteresis loop with non-linear elastic behaviour shows significant discrepancies for the non-linear elastic parts of the hysteresis loop. These discrepancies are caused by the adopted strategy to fit the frictional elements to experimental data. The frictional elements have been fitted to steady state harmonic dynamic test data (linear elastic), so the frictional damping for amplitudes corresponding to non-linear elastic behaviour have not been identified. The lack of frictional damping for the non-linear

elastic parts of the hysteresis loop with 9.0 mm amplitude is clear. The hysteresis loops for the low amplitudes presented in Chapter 4 have been left out since they have linear elastic behaviour and therefore are as accurately calculated as the hysteresis loops for 3.0 and 6.0 mm.

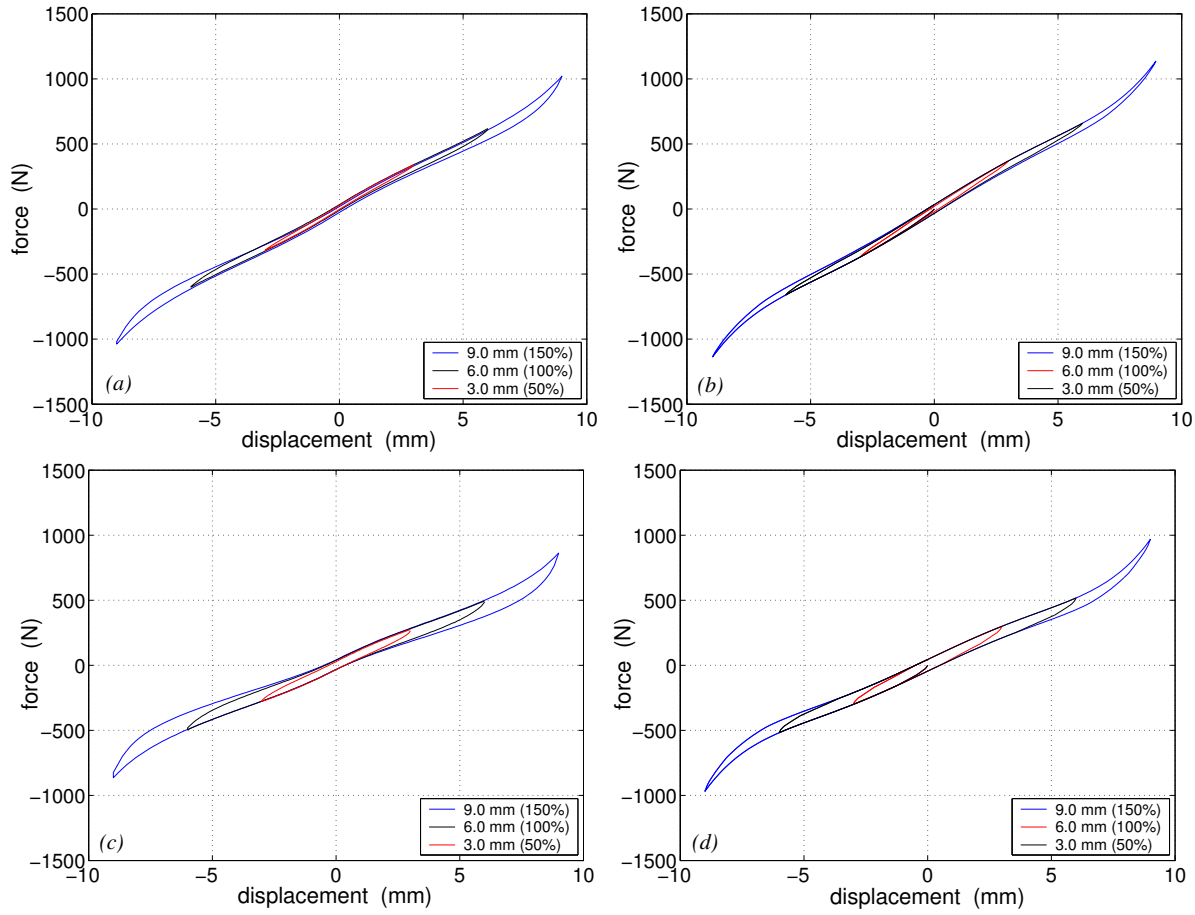

Figure 6.3: *Validation of the generalized non-linear elastic viscoelastic elastoplastic models of the double shear specimens for static behaviour. Low filled specimen A in (a) and (b), high filled specimen B in (c) and (d). Measured responses in (a) and (c), calculated responses in (b) and (d). Corresponding shear strain is given for each amplitude.*

Steady state harmonic dynamic behaviour

The model of shear specimen A (three viscoelastic and four elastoplastic elements) is validated in Figure 6.4, 6.5, and 6.6. The 3-D plots in Figure 6.4(a) and (b) give an overview of the calculated and measured behaviour, whereas the 2-D plots in Figure 6.4(c) and (d) give more detailed information. The generalized non-linear elastic viscoelastic elastoplastic model is not able to capture the frequency dependence perfectly. The model typically overestimates the dynamic stiffness for low frequencies and underestimates the dynamic stiffness for high frequenies, see Figure 6.4(c). The amplitude 0.060 mm seems to be the most difficult amplitude to model with respect to both dynamic stiffness and phase angle. By studying the phase angle in Figure 6.4(d) it can be seen that shear specimen A is modelled with great accuracy for frequencies between 0.1-25 Hz and that the correlation is worse for higher frequencies.

Measured and calculated hysteresis loops for low amplitudes at 0.3 Hz and at 49 Hz are plotted in Figure 6.5. The slope and enclosed area of the hysteresis loops seems to be quite accurately modelled. The calculated hysteresis loops are sharp edged for low amplitudes cf. Figure 6.5(b) and (d). This phenomena appears since only one frictional element is working. Hysteresis loops for high amplitudes are validated in Figure 6.6. Figure 6.6(a) and (b) illustrate just like Figure 6.4(c) that the generalized non-linear elastic viscoelastic elastoplastic model overestimates the dynamic stiffness for low frequencies. Calculated and measured hysteresis loops show good agreement for high amplitudes cf. Figure 6.6. To sum up it can be concluded that the model describes the behaviour of shear specimen A with satisfying accuracy.

The model of shear specimen B (one viscoelastic and four elastoplastic elements) is validated in Figure 6.7, 6.8, and 6.9. The behaviour for high amplitudes is predicted more accurate than the behaviour for low amplitudes, see Figure 6.7.

The slope and enclosed area of the hysteresis loops correlate well cf. Figure 6.8 and 6.9. As for shear specimen A, the calculated hysteresis loops are sharp edged for low amplitudes, see Figure 6.8(b) and (d). The model captures the behaviour of shear specimen B with satisfying accuracy.

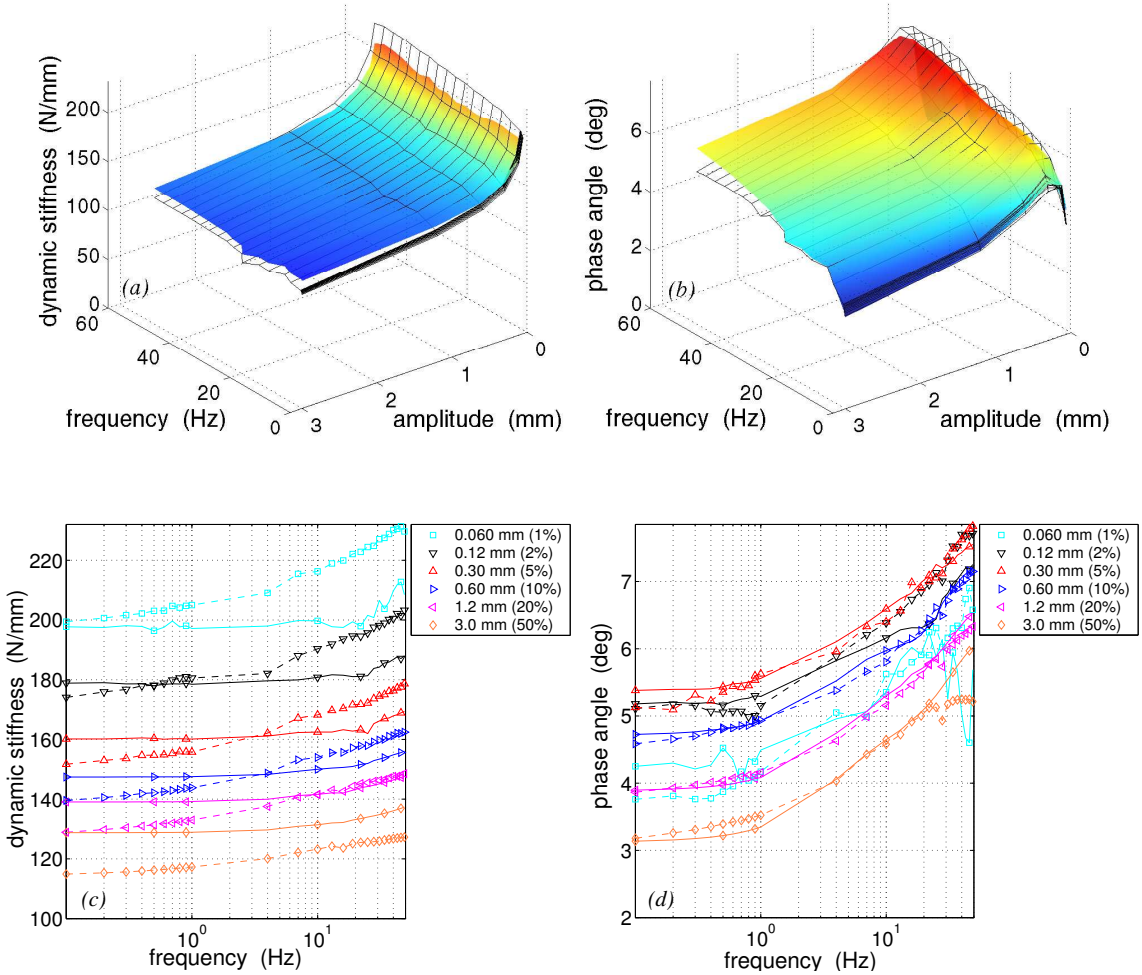

Figure 6.4: *Validation of the generalized non-linear elastic viscoelastic elastoplastic model of shear specimen A for steady state harmonic dynamic behaviour. The model has three Maxwell and four frictional elements. Solid lines and surfaces are calculated responses, dashed lines and grid surfaces are measured responses. Corresponding shear strain is given for each amplitude.*

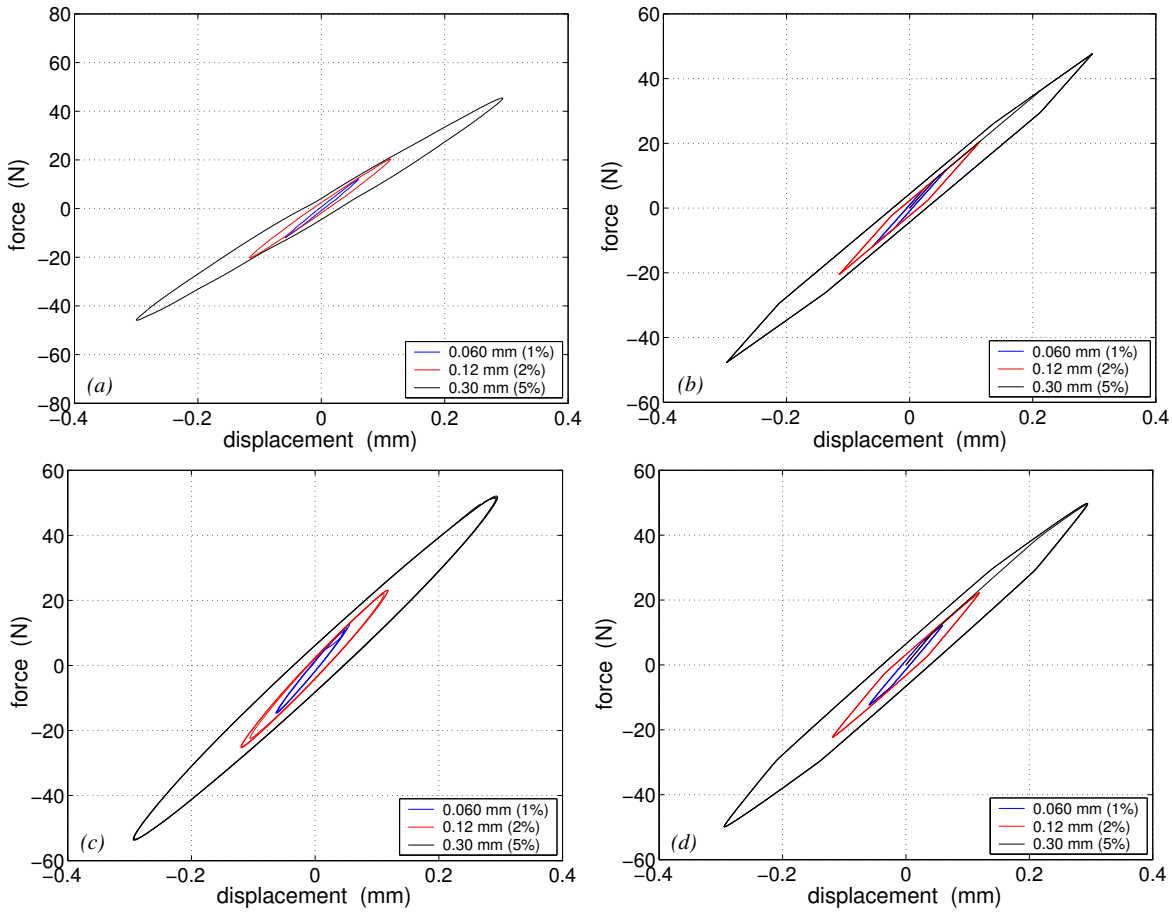

Figure 6.5: *Calculated and measured hysteresis loops for low amplitudes at 0.3 Hz ((a) and (b)) and at 49 Hz ((c) and (d)), shear specimen A. The model has three Maxwell and four frictional elements. Measured responses in (a) and (c), calculated responses in (b) and (d). Corresponding shear strain is given for each amplitude.*

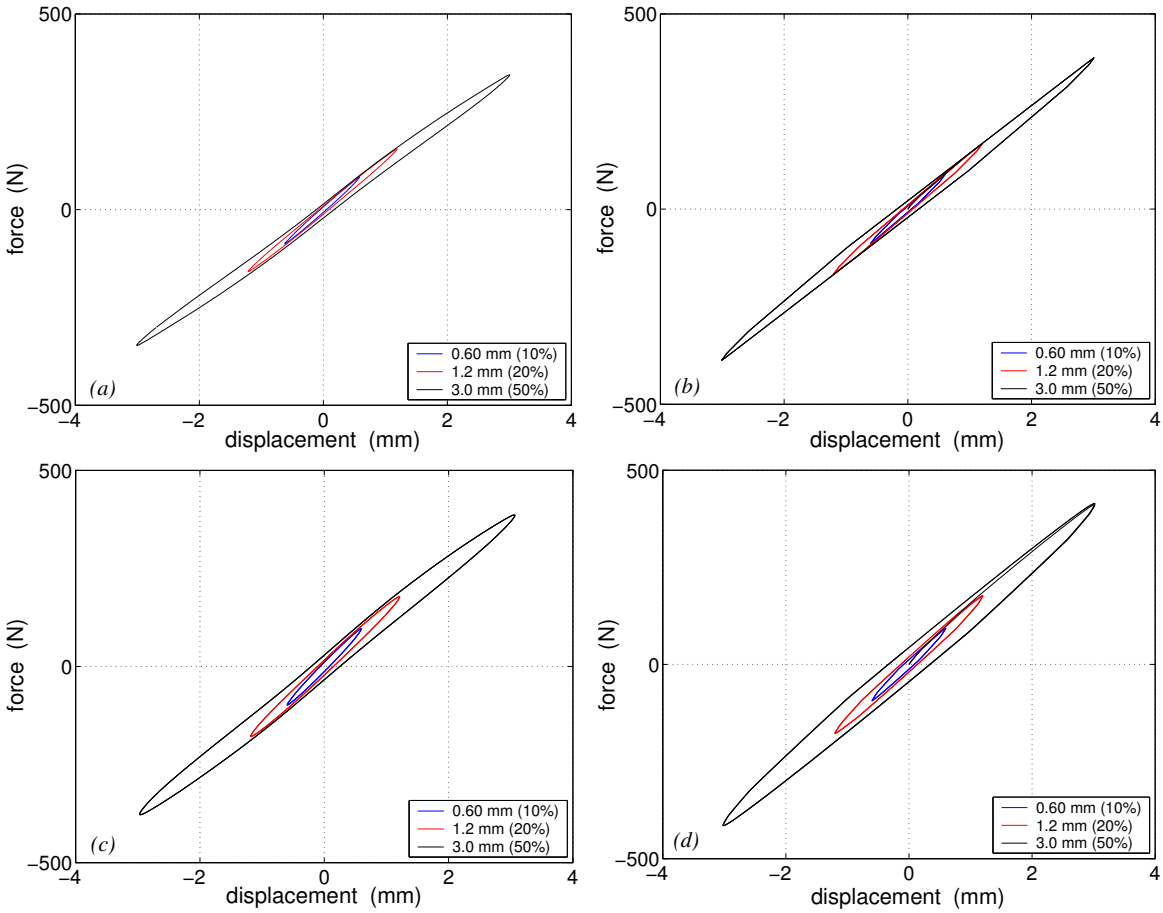

Figure 6.6: *Calculated and measured hysteresis loops for high amplitudes at 0.3 Hz ((a) and (b)) and at 49 Hz ((c) and (d)), shear specimen A. The model has three Maxwell and four frictional elements. Measured responses in (a) and (c), calculated responses in (b) and (d). Corresponding shear strain is given for each amplitude.*

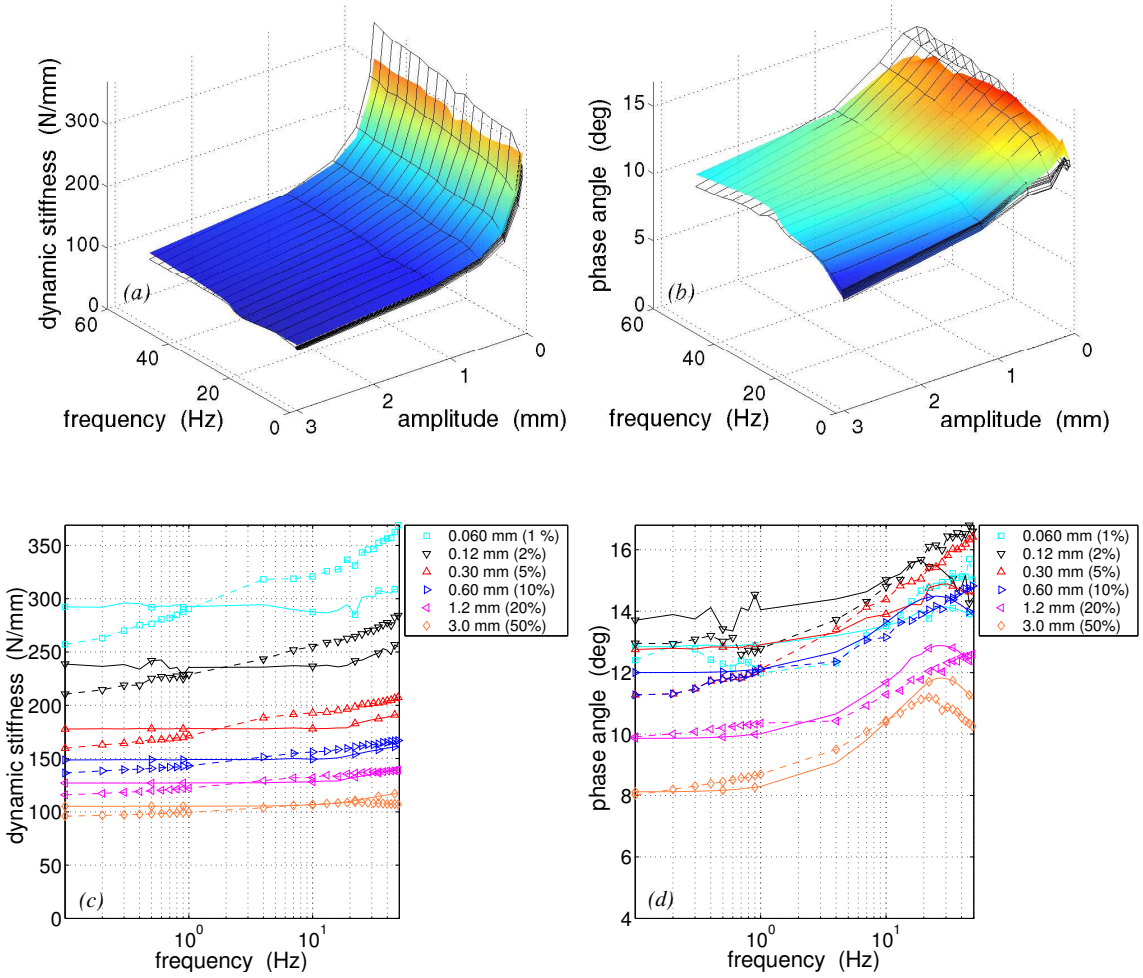

Figure 6.7: *Validation of the generalized non-linear elastic viscoelastic elastoplastic model of shear specimen B for steady state harmonic dynamic behaviour. The model has one Maxwell and four frictional elements. Solid lines and surfaces are calculated responses, dashed lines and grid surfaces are measured responses. Corresponding shear strain is given for each amplitude.*

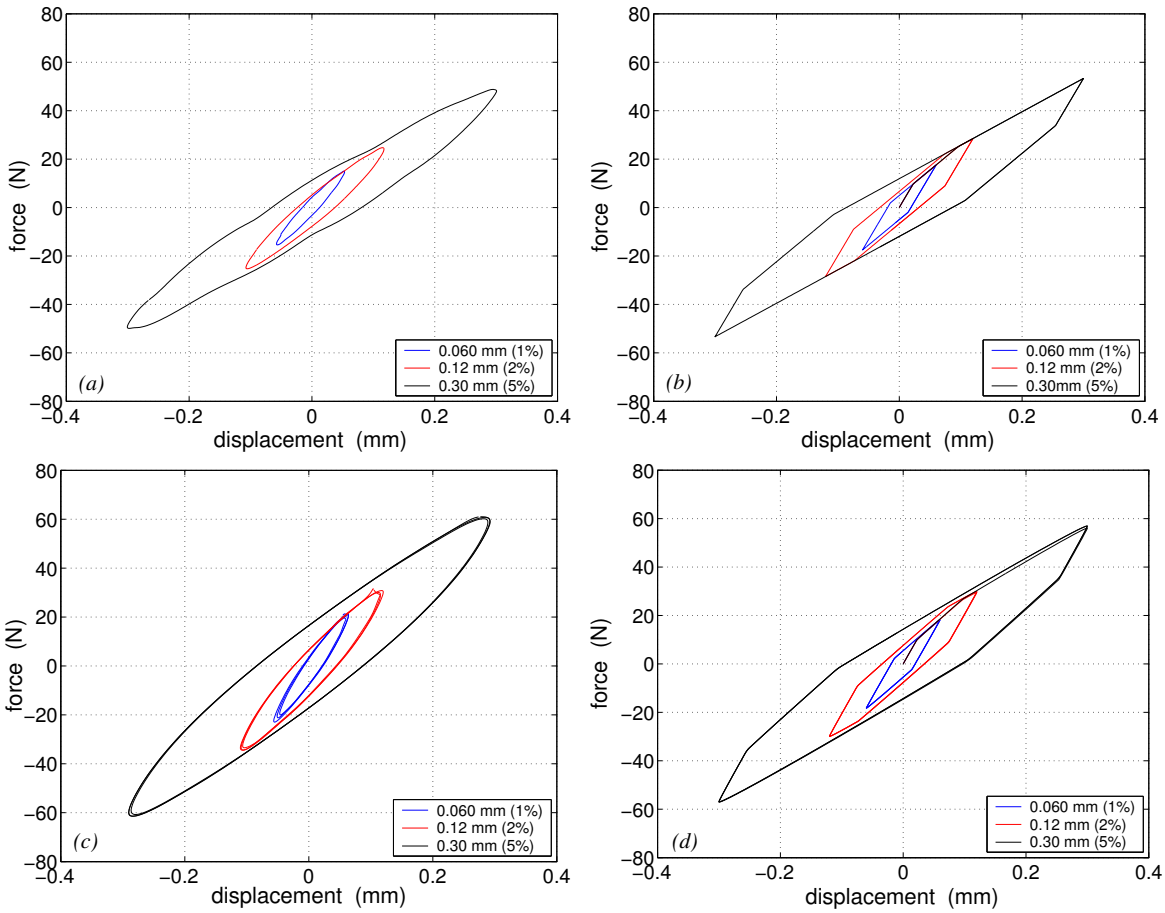

Figure 6.8: *Calculated and measured hysteresis loops for low amplitudes at 0.3 Hz ((a) and (b)) and at 49 Hz ((c) and (d)), shear specimen B. The model has one Maxwell and four frictional elements. Measured responses in (a) and (c), calculated responses in (b) and (d). Corresponding shear strain is given for each amplitude.*

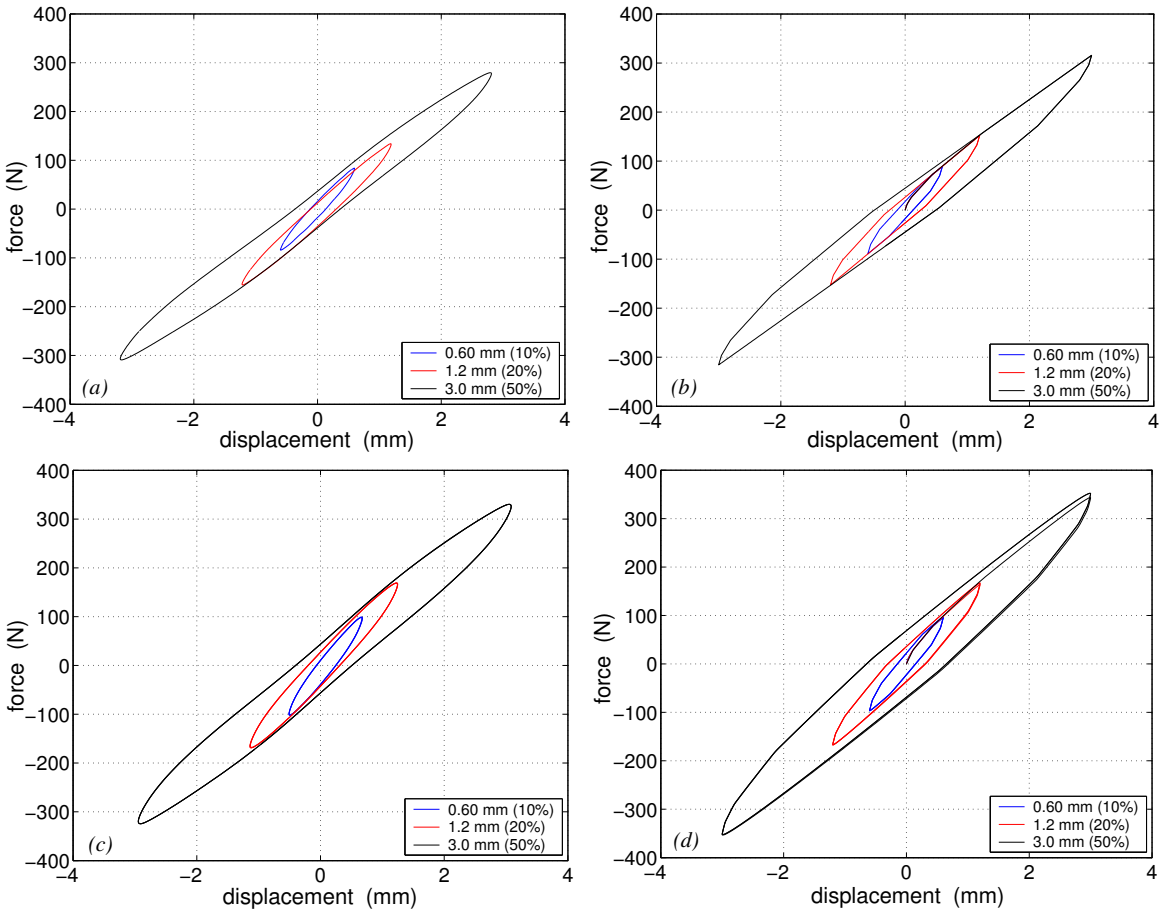

Figure 6.9: *Calculated and measured hysteresis loops for high amplitudes at 0.3 Hz ((a) and (b)) and at 49 Hz ((c) and (d)), shear specimen B. The model has one Maxwell and four frictional elements. Measured responses in (a) and (c), calculated responses in (b) and (d). Corresponding shear strain is given for each amplitude.*

6.3.2 Cylindrical bushings

The models of cylindrical bushing C and D are validated in this section. The viscoelastic models are first discussed and then the generalized non-linear elastic viscoelastic elastoplastic model.

Viscoelastic models

The viscoelastic models (Kelvin-Voigt, Zener, generalized Maxwell) are validated with measurements in Figure 6.10. The Kelvin-Voigt and Zener model are fitted to the measured data with the Matlab function fmins, whereas the generalized Maxwell model is fitted with fmincon [3]. The viscoelastic models are unable to describe amplitude dependence and are therefore fitted to the mean value of the dynamic stiffness and phase angle for the largest and smallest amplitude. Just as for the shear specimens, the calculated and measured responses correlate poorly cf. Figure 6.10.

The Kelvin-Voigt model gives an almost constant dynamic stiffness as function of frequency and a phase angle linearly dependent on frequency. The Zener model underestimates the dynamic stiffness for low frequencies and overestimates the dynamic stiffness for high frequencies. The Kelvin-Voigt and Zener model are unable to capture the frequency dependence of the phase angle. The generalized Maxwell model describes the frequency dependence of the dynamic stiffness and phase angle fairly well with respect to the mean value. The fitting curve for the generalized Maxwell model in Figure 6.10(b) and (d) can be understood to be discontinuous. This is a phenomena from the plotting, a smaller frequency step will give continuous curves, i.e. the model is continuous. The viscoelastic model that describes the behaviour of the cylindrical bushings most accurate is the generalized Maxwell model.

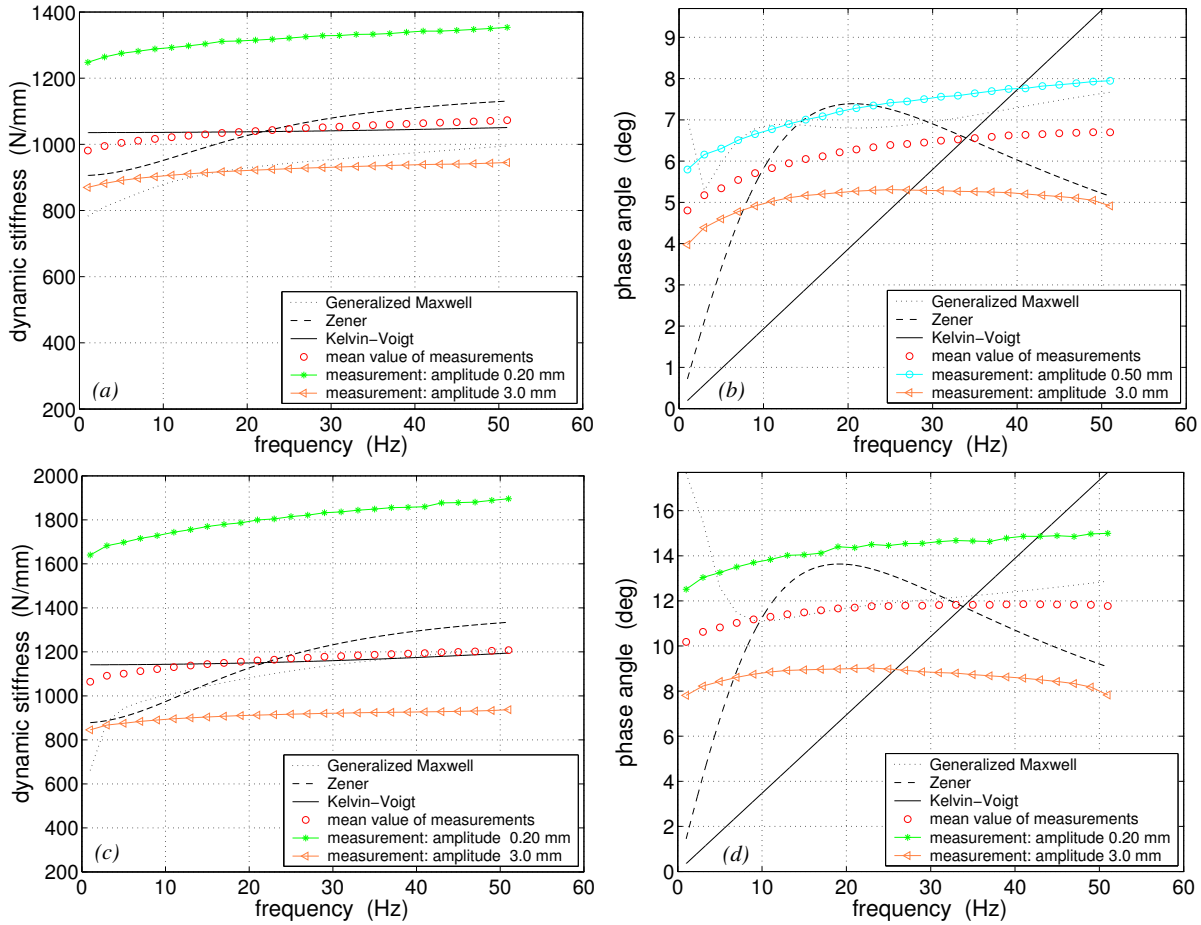

Figure 6.10: *Validation of the viscoelastic models of the cylindrical bushings for steady state harmonic dynamic behaviour. Low filled specimen C in (a) and (b), high filled specimen D in (c) and (d). The generalized Maxwell model of bushing C and D has three and four Maxwell elements respectively.* ***Note:*** *The generalized Maxwell models have the phase angle 0 degrees at 0 Hz. It is first at 1 Hz that the phase angle has the value that is shown in (b) and (d).*

Generalized non-linear elastic viscoelastic elastoplastic model

The static behaviour is first validated, thereafter the harmonic dynamic behaviour, and finally the quasi-static behaviour. Three Maxwell and three frictional elements are needed to get an accurate modelling of bushing C. Bushing D is modelled by one Maxwell and six frictional elements. Just as for the shear specimens it is possible to get more accurate models by increasing the number of elements, but the improvement is hardly noticeable. The relative error *(err)* defined in equation (6.1) as function of number of Maxwell and frictional elements is plotted in Figure 6.11.

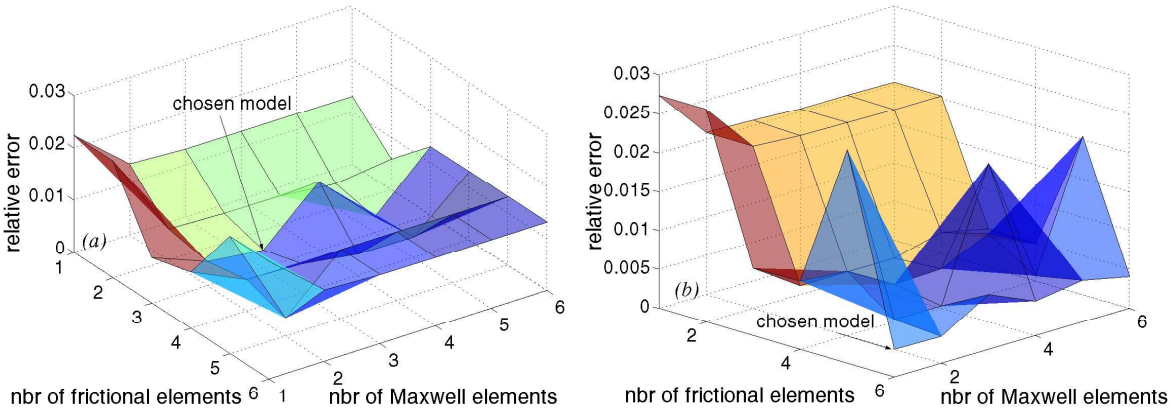

Figure 6.11: *Relative error as function of number of frictional and Maxwell elements. The relative error is established from steady state harmonic dynamic tests. Low filled bushing C in (a) and high filled bushing D in (b).*

Static behaviour

The generalized non-linear elastic viscoelastic elastoplastic model describes the overall static behaviour of bushing D in a satisfying manner, see Figure 6.12. In Figure 6.12(a) it can be seen that damage is appearing in cylindrical bushing C. The damage is presumable an effect from the measurements. The bushing might have been at rest long enough so the stiffness could recover. Damage can not be described by the models presented in this Master's thesis. The hysteresis loops for bushing D with linear elastic behaviour are calculated very accurately, whereas the hysteresis loop for bushing D with non-linear elastic behaviour shows significant discrepancies for the non-linear elastic parts of the hysteresis loop. These discrepancies are caused by the adopted strategy to fit the frictional elements. The frictional elements have been fitted to steady state harmonic dynamic test data (linear elastic), so the frictional damping for amplitudes corresponding to non-linear elastic behaviour have not been identified. The lack of frictional damping for the non-linear elastic parts of the hysteresis loop with 6.25 mm amplitude is clear. The hysteresis loops for the low amplitudes presented in Chapter 4 have been left out since they have linear elastic behaviour and therefore are as accurately calculated as the hysteresis loops for 1.2 and 3.0 mm.

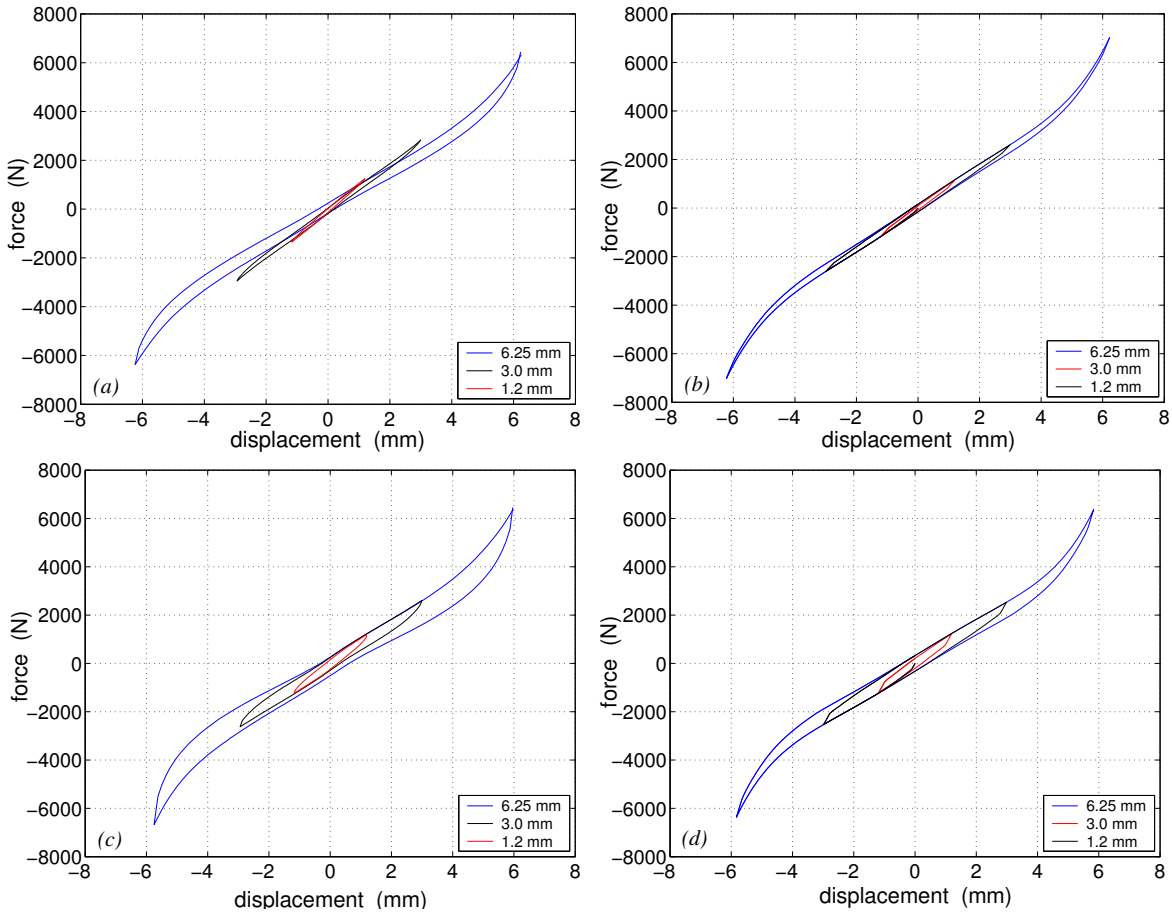

Figure 6.12: *Validation of the generalized non-linear elastic viscoelastic elastoplastic models of the cylindrical bushings for static behaviour. Low filled bushing C in (a) and (b), high filled bushing D in (c) and (d). Measured responses in (a) and (c), calculated responses in (b) and (d).*

Steady state harmonic dynamic behaviour

The model of cylindrical bushing C (three Maxwell and three frictional elements) is validated in Figure 6.13, 6.14, and 6.15. The 3-D plots in Figure 6.13(a) and (b) give an overview of the calculated and measured behaviour, whereas the 2-D plots in Figure 6.13(c) and (d) give more detailed information. The generalized non-linear elastic viscoelastic elastoplastic model correlates well for dynamic stiffness cf. Figure 6.13(c). The dynamic stiffness is however mostly overestimated and the behaviour for 0.20 mm amplitude is not perfectly modelled. The dynamic stiffness is most accurately modelled for 15 Hz and higher frequencies. Furthermore, the model describes the phase angle with high accuracy cf. Figure 6.13(d). The largest discrepancies for the phase angle are for the 3.0 mm amplitude.

Hysteresis loops for low amplitudes at 5 Hz and at 51 Hz are validated in Figure 6.14. As concluded earlier the slope and enclosed area of the hysteresis loops are accurately modelled, but as for the shear specimens, the hysteresis loops are sharp edged for low amplitudes. The calculated and measured hysteresis loops for high amplitudes show good agreement (cf. Figure 6.15). The model describes the behaviour of bushing C with satisfying accuracy.

The model of cylindrical bushing D (one Maxwell and six frictional elements) is validated in Figure 6.16, 6.17, and 6.18. The largest discrepancies for dynamic stiffness and phase angle are for 0.20 and 3.0 mm amplitude respectively, see Figure 6.16(c) and (d). The hysteresis loops in Figure 6.17 and 6.18 are sharp edged, but the dynamic stiffness and phase angle are accurately modelled. The model captures the behaviour of bushing D with satisfying accuracy.

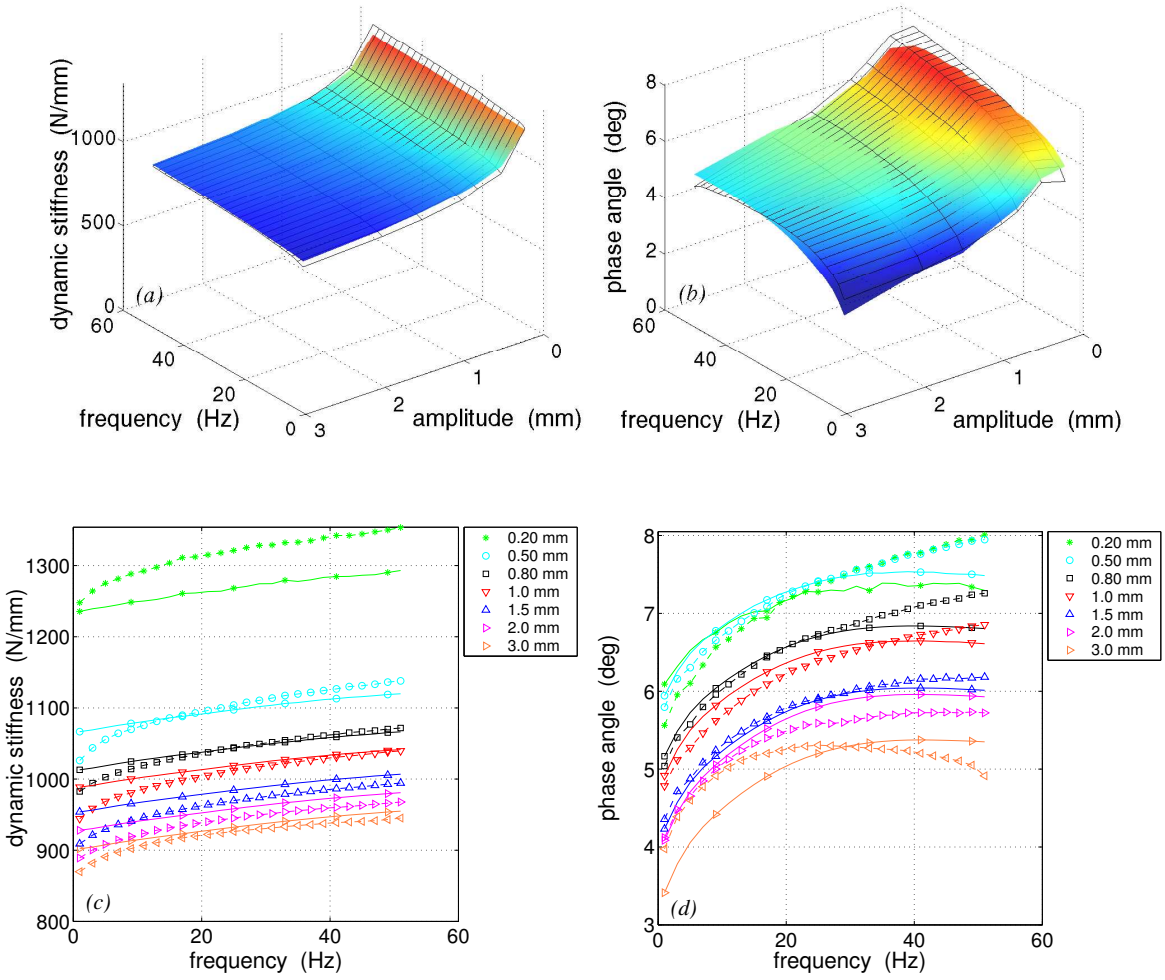

Figure 6.13: *Validation of the generalized non-linear elastic viscoelastic elastoplastic model of bushing C for steady state harmonic dynamic behaviour. The model has three Maxwell and three frictional elements. Solid lines and surfaces are calculated responses, dashed lines and grid surfaces are measured responses.*

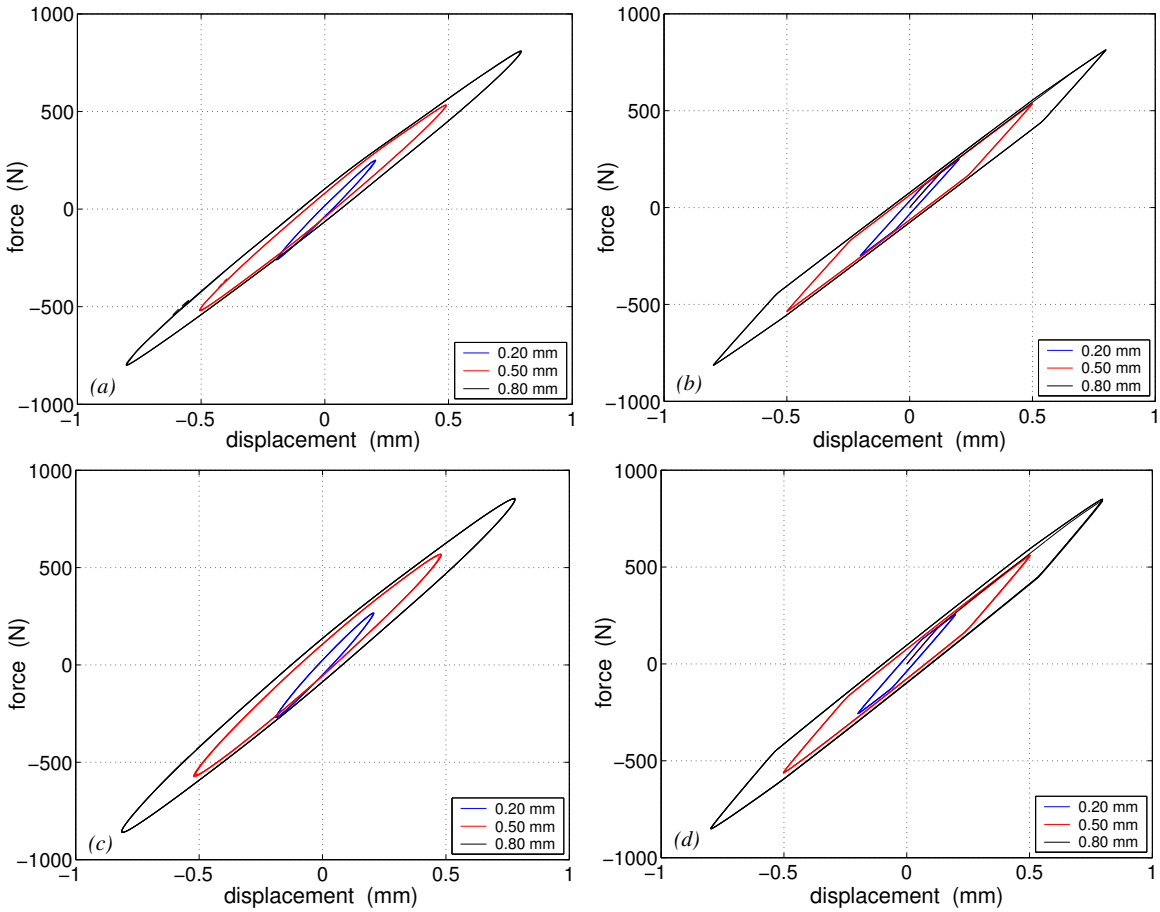

Figure 6.14: *Calculated and measured hysteresis loops for low amplitudes at 5 Hz ((a) and (b)) and at 51 Hz ((c) and (d)), bushing C. The model has three Maxwell and three frictional elements. Measured responses in (a) and (c), calculated responses in (b) and (d).*

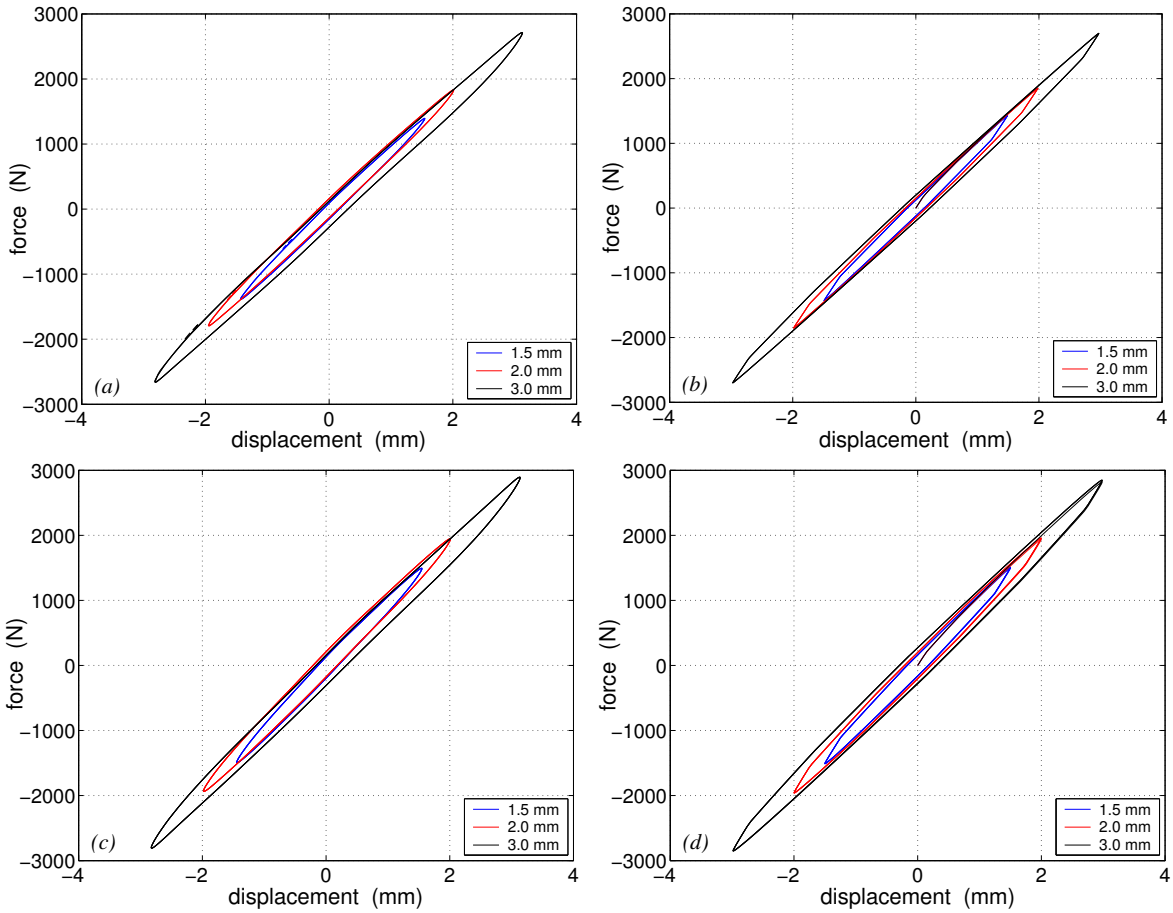

Figure 6.15: *Calculated and measured hysteresis loops for high amplitudes at 5 Hz ((a) and (b)) and at 51 Hz ((c) and (d)), bushing C. The model has three Maxwell and three frictional elements. Measured responses in (a) and (c), calculated responses in (b) and (d).*

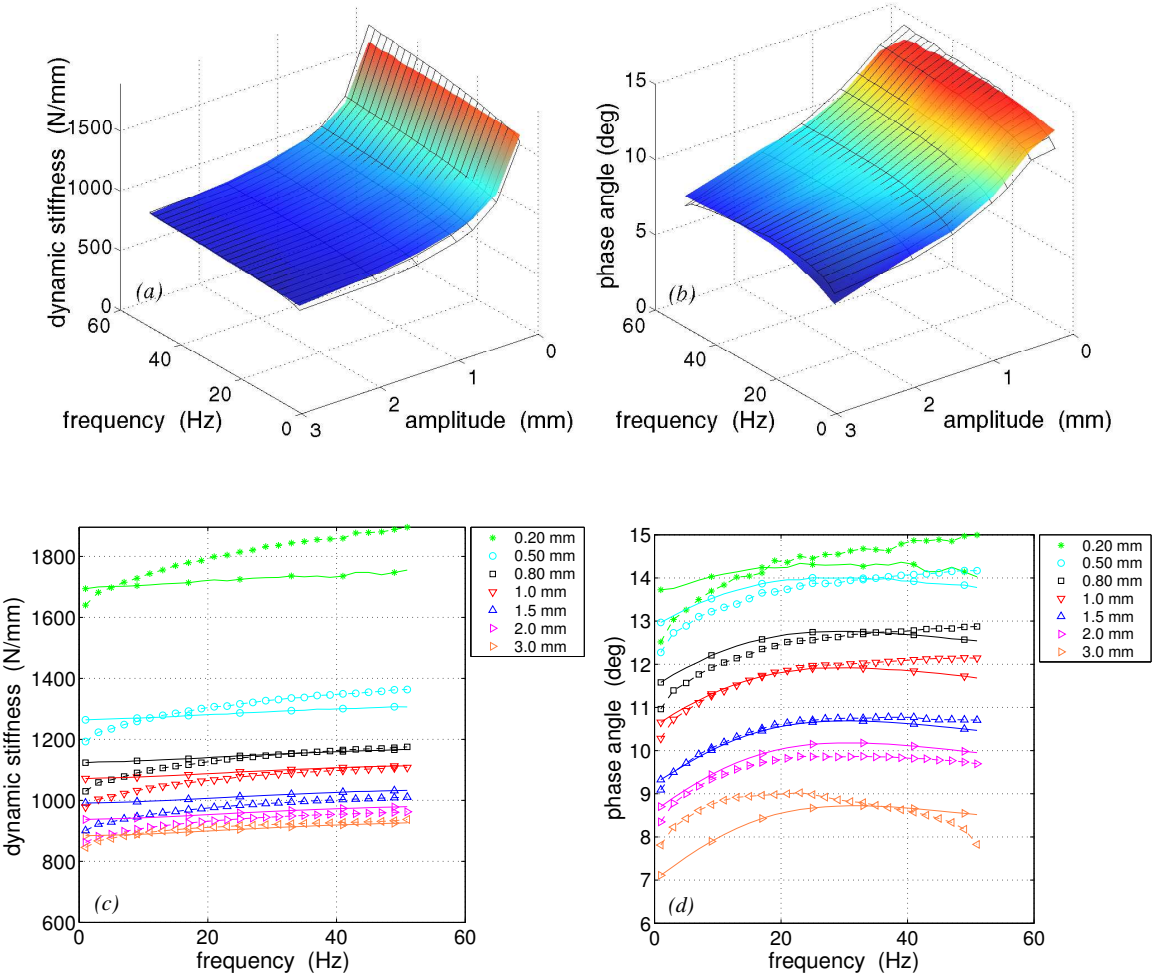

Figure 6.16: *Validation of the generalized non-linear elastic viscoelastic elastoplastic model of bushing D for steady state harmonic dynamic behaviour. The model has one Maxwell and six frictional elements. Solid lines and surfaces are calculated responses, dashed lines and grid surfaces are measured responses.*

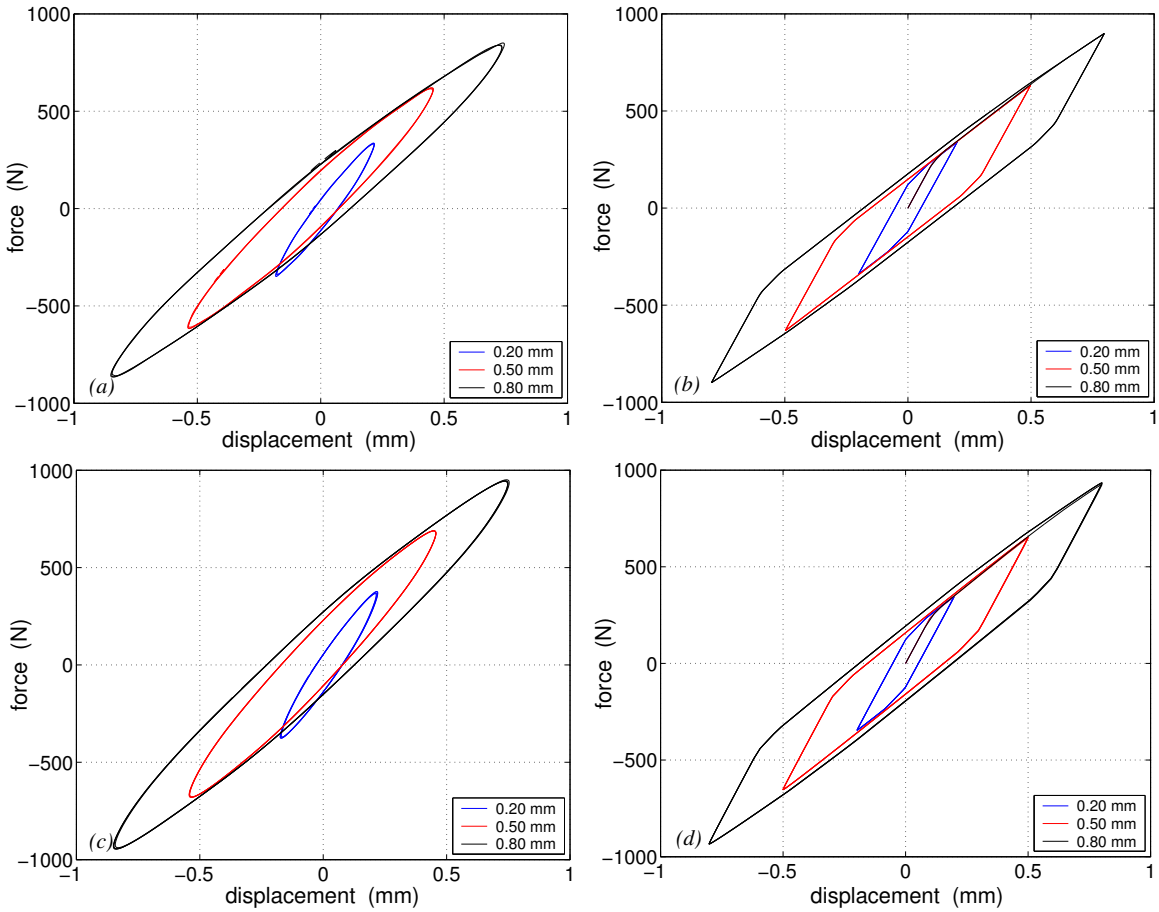

Figure 6.17: *Calculated and measured hysteresis loops for low amplitudes at 5 Hz ((a) and (b)) and at 51 Hz ((c) and (d)), bushing D. The model has one Maxwell and six frictional elements. Measured responses in (a) and (c), calculated responses in (b) and (d).*

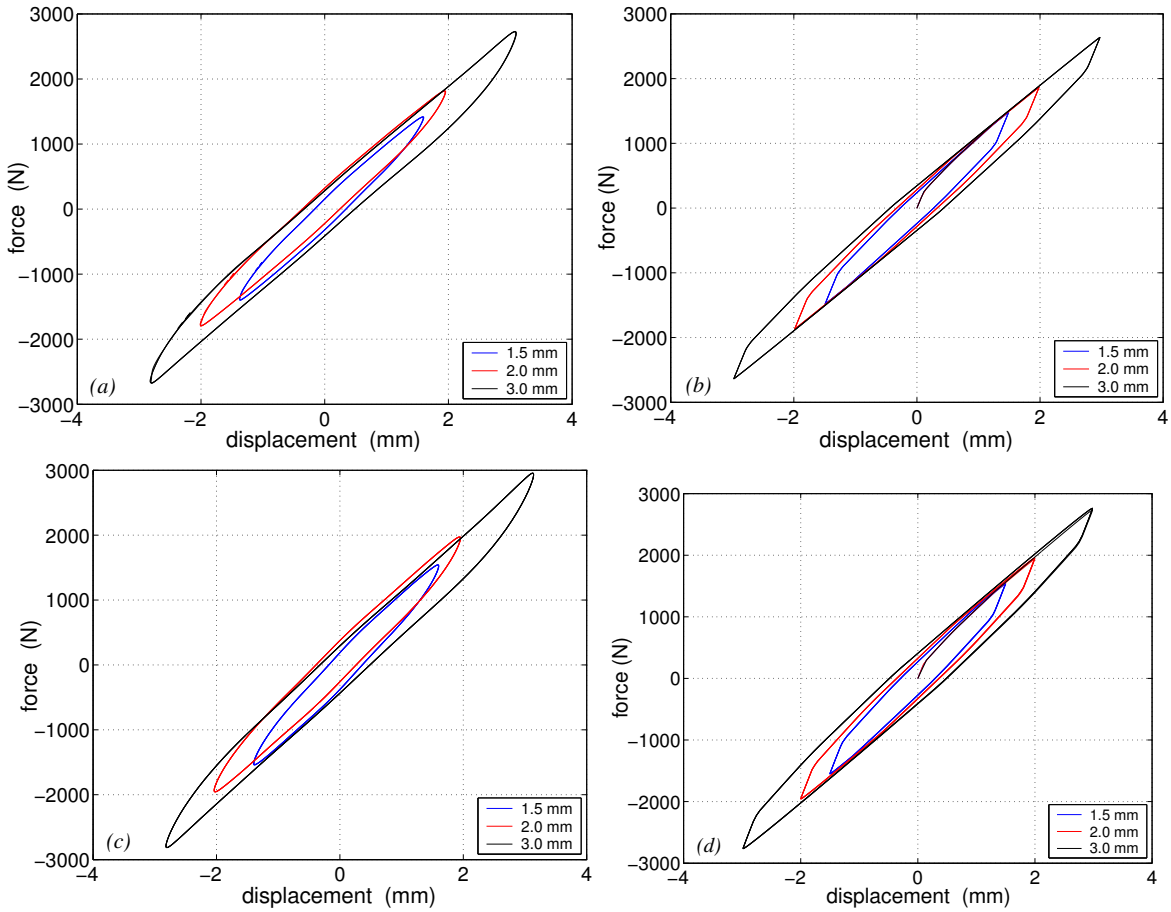

Figure 6.18: *Calculated and measured hysteresis loops for high amplitudes at 5 Hz ((a) and (b)) and at 51 Hz ((c) and (d)), bushing D. The model has one Maxwell and six frictional elements. Measured responses in (a) and (c), calculated responses in (b) and (d).*

Quasi-static behaviour

The generalized non-linear elastic viscoelastic elastoplastic model describes the overall quasi-static behaviour of bushing C and D well, see Figure 6.19. The significant discrepancies for the non-linear elastic parts of the hysteresis loops are caused by the adopted strategy to fit the frictional elements to experimental data, see the discussion for static behaviour on page 74.

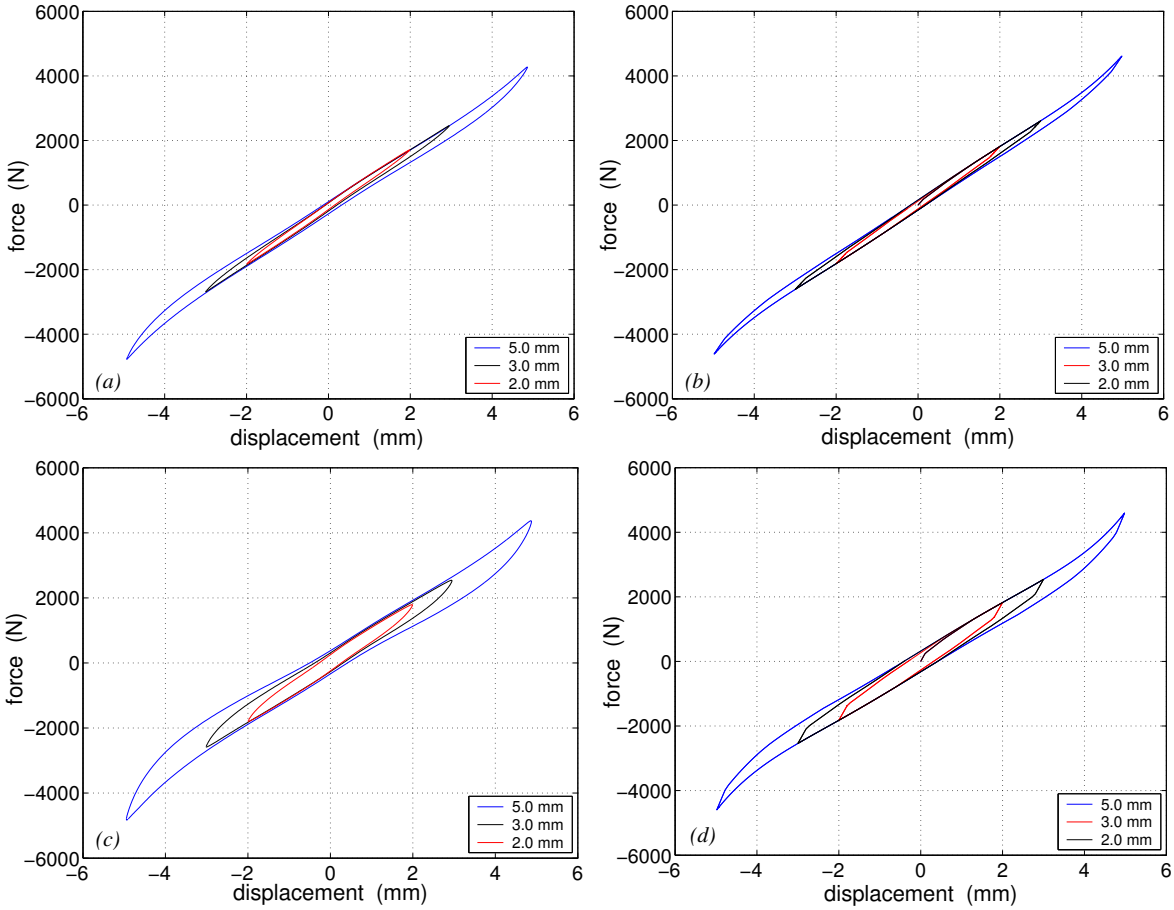

Figure 6.19: *Validation of the generalized non-linear elastic viscoelastic elastoplastic models of the cylindrical bushings for quasi-static behaviour. Low filled bushing C in (a) and (b), high filled bushing D in (c) and (d). Measured responses in (a) and (c), calculated responses in (b) and (d).*

6.3.3 Hydrobushing

The measurements for the hydrobushing show that the amplitude and frequency dependence are coupled. All the presented models in this dissertation have however uncoupled amplitude and frequency dependence. The modelling of the hydrobushing is therefore expected to correlate poorly. A generalized linear elastic viscoelastic elastoplastic model has been validated for steady state harmonic dynamic behaviour.

Generalized linear elastic viscoelastic elastoplastic model

The hydrobushing has been modelled by two Maxwell and four frictional elements. The relative error *(err)* defined in equation (6.1) as function of number of Maxwell and frictional elements is plotted in Figure 6.20. It can be seen that the number of elements has a weak influence on the quality of the model. The inability of the model to describe coupled amplitude and frequency dependence is clearly seen in Figure 6.21, 6.22, and 6.23. A proposed one dimensional model that presumably could describe the behaviour of the hydrobushing more accurately is discussed Chapter 9.

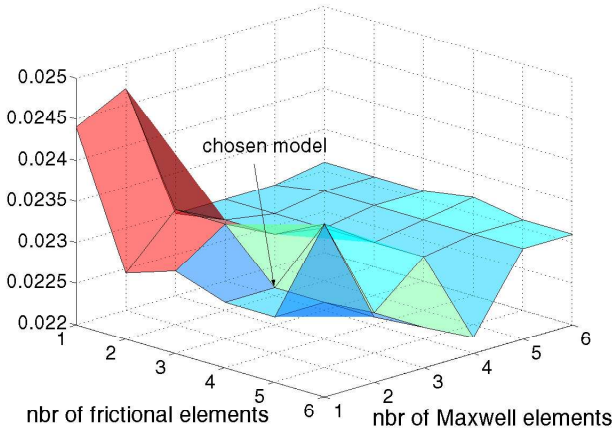

Figure 6.20: *Relative error as function of number of frictional and Maxwell elements. The relative error is established from steady state harmonic dynamic tests.*

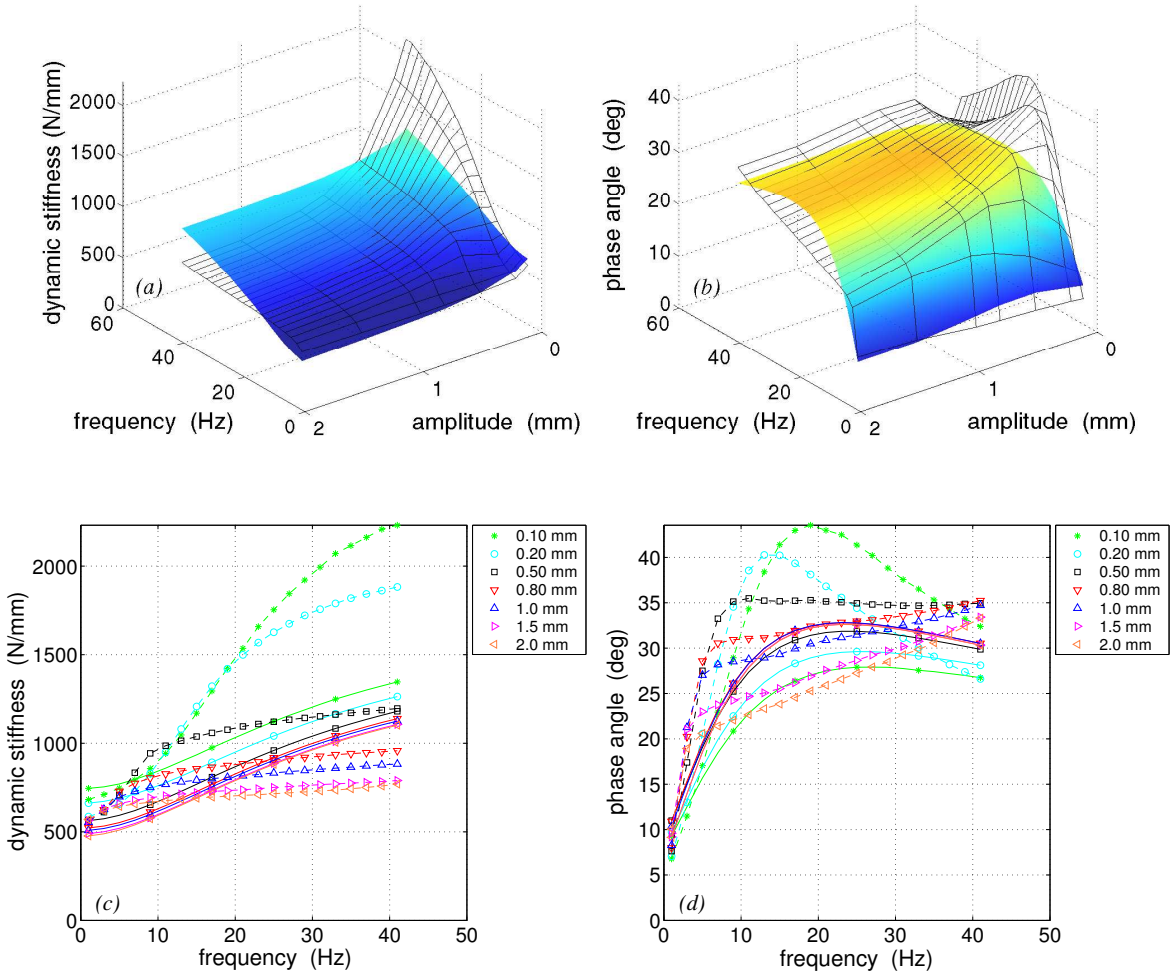

Figure 6.21: *Validation of the generalized linear elastic viscoelastic elastoplastic model of the hydrobushing for steady state harmonic dynamic behaviour. The model has two Maxwell and four frictional elements. Solid lines and surfaces are calculated responses, dashed lines and grid surfaces are measured responses.*

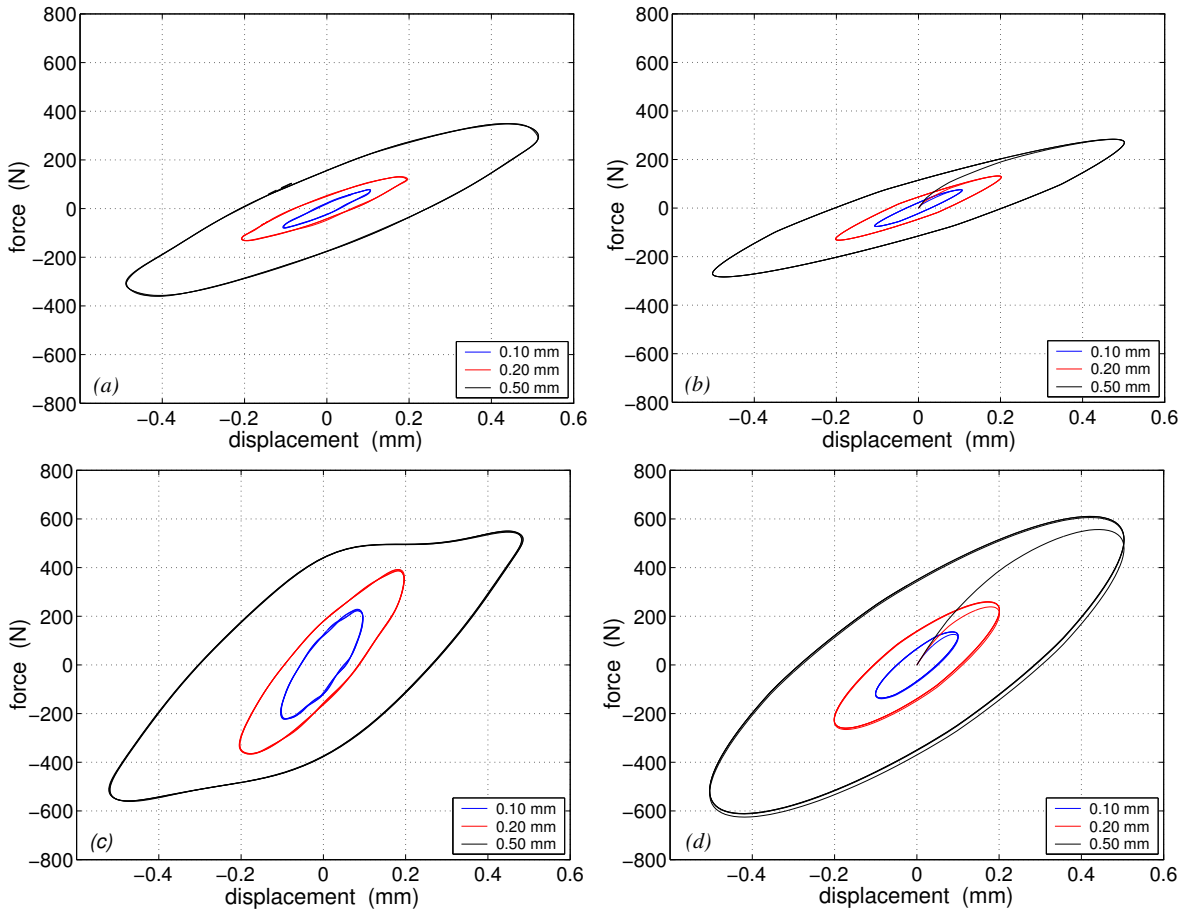

Figure 6.22: *Calculated and measured hysteresis loops for low amplitudes at 5 Hz ((a) and (b)) and at 41 Hz ((c) and (d)), hydrobushing. The model has two Maxwell and four frictional elements. Measured responses in (a) and (c), calculated responses in (b) and (d).*

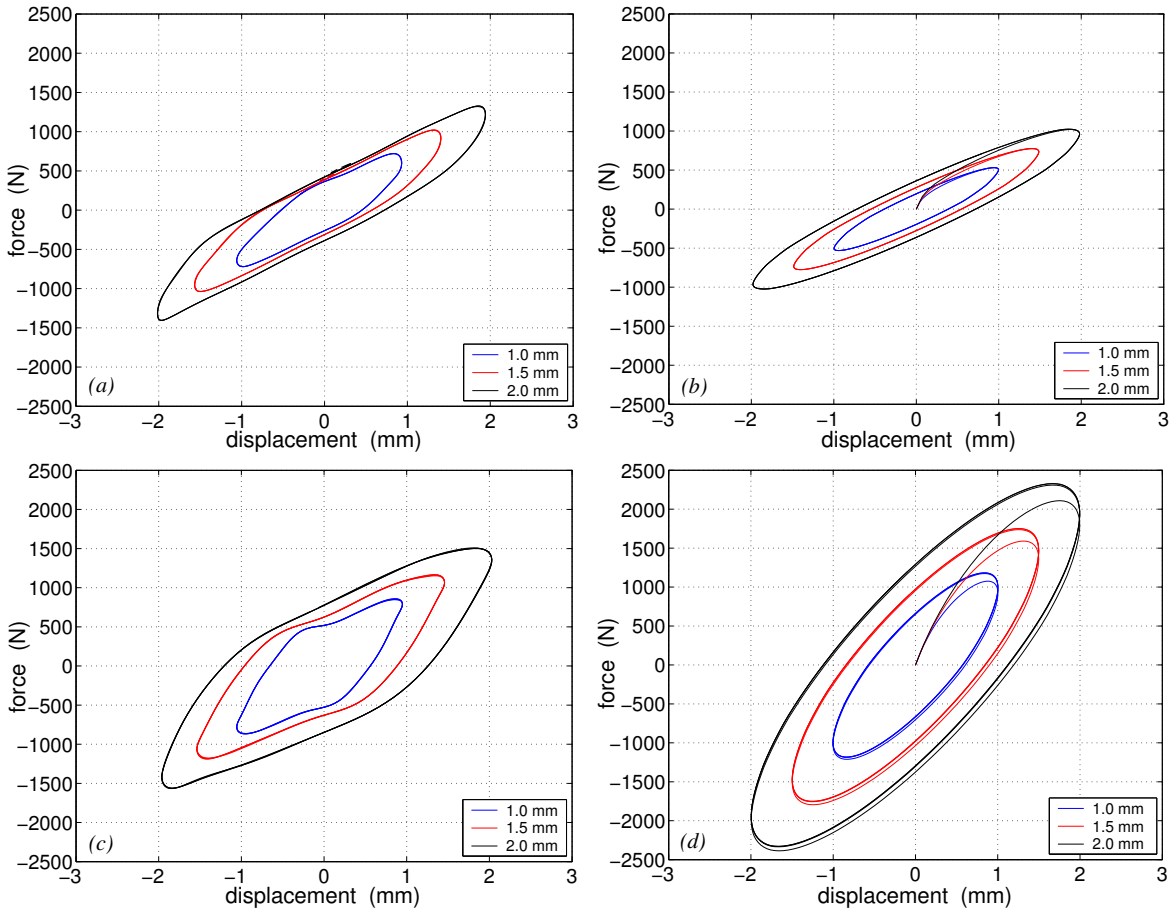

Figure 6.23: *Calculated and measured hysteresis loops for high amplitudes at 5 Hz ((a) and (b)) and at 41 Hz ((c) and (d)), hydrobushing. The model has two Maxwell and four frictional elements. Measured responses in (a) and (c), calculated responses in (b) and (d).*

6.3.4 Summary of the validation

Important findings from the validation are summarized here. Limitations, advantages, and possibilities of the models are noted.

- The inability to capture amplitude dependence limits the use of viscoelastic models such as Kelvin-Voigt, Zener, and generalized Maxwell. The Kelvin-Voigt and Zener model describe the component behaviours very poorly. The generalized Maxwell model correlates best of the viscoelastic models. The strong amplitude dependence is however not taken into account, which is a severe limitation.

- The rubber components with uncoupled amplitude and frequency dependence (i.e. the shear specimens and cylindrical bushings) have been successfully modelled with the generalized non-linear elastic viscoelastic elastoplastic model for static as well as quasi-static and steady state harmonic dynamic loading.

- The hysteresis loops for the cylindrical bushings with linear elastic behaviour are calculated very accurately with the generalized non-linear elastic viscoelastic elastoplastic model, whereas the hysteresis loops with non-linear elastic behaviour show significant discrepancies for the non-linear elastic parts of the hysteresis loops. These discrepancies are caused by the adopted strategy to fit the frictional elements to experimental data. The frictional elements have been fitted to steady state harmonic dynamic test data (linear elastic), so the frictional damping for amplitudes corresponding to non-linear elastic behaviour have not been identified. The lack of frictional damping for the non-linear elastic parts of the hysteresis loops is clearly seen in the plots.

- The generalized linear elastic viscoelastic elastoplastic model is not able to describe the coupled amplitude and frequency dependence of the hydrobushing.

- The behaviour for low amplitudes at steady state harmonic dynamic excitation is most difficult to describe for the generalized non-linear elastic viscoelastic elastoplastic models.

- The calculated hysteresis loops are sharp edged for low amplitudes. This is an effect of the Coulumb friction in combination with few active frictional elements for low amplitudes.

Chapter 7

Practical aspects of the viscoplastic model

There are some general aspects that should be considered when formulating a mathematical model which is intended to be used in computer simulations. In this chapter, these aspects are discussed together with aspects concerning the proposed generalized viscoplastic (viscoelastic elastoplastic) model.

The construction of the model is a compromise between retaining all factors that could likely have a bearing on the validity of the model and keeping the mathematical model sufficiently simple so it is solvable using the tools at hand. As an example of this the proposed model is 1-D and will not be able to predict any potential coupling effects that can arise in combined axial and radial load cases.

Another aspect of the model is that the number of frictional and Maxwell elements are chosen so that the physics of the bushing can sufficiently be predicted. This will put the requirement on the implementation in ADAMS that this feature can be utilized without any extra effort. This means that the number of fractions in the implemented model should not be fixed. Another aspect of the model is that the number of frictional and Maxwell elements are chosen so that the model correlates well with the experimental data. The implementation in ADAMS has to have this feature, i.e. the number of fractions in the implemented model can not be fixed.

A crucial requirement on the mathematical formulation of the model is that it must be stable for the numerical methods that are provided in commercial MBS packages. Furthermore, the solutions obtained must be as accurate as necessary. As for this, the formulation of the frictional element is critical. Friction has the intrisic property of being highly non-linear, and especially the Coulomb friction model which also is discontinuous. In general, predictor-corrector integrators are not suitable for discontinuities and if a multi-step method is used the order of the integrator must probably be reduced in order to continue the solution. The formulation must also be suitable for integrators which make use of variable step size, i.e. a time-stepping

algorithm for fixed step sizes is not possible. Taking the mentioned aspects into consideration, it is necessary to work out another formulation for the frictional element than the Coulomb model.

One of the major considerations besides accuracy in the development of mathematical models is efficiency. By this we mean the amount of effort, both human and computer, required to solve a given problem. With this in mind and what have been mentioned above we can identify some issues that will have impact on efficiency:

- In order to get model parameters we have to perform extensive testing
- The fitting procedure make use of closed-form solutions which may not be possible to use for a new friction formulation
- The friction formulation will have an effect on the effort needed by the integrator
- The number of frictional and Maxwell elements

Besides this issues conserning mathematical formulation and efficiency, we are rather convinced that the proposed viscoplastic model, although with some further development, together with the fitting procedure have the potential to be an important part in vehicle dynamic simulations.

Chapter 8

Summary and conclusions

The main objectives of this Master's thesis have been to:

- Gain further insight in material characteristics and dynamic properties of rubber components.
- Analyse and determine the validity of different bushing models.
- Develop a methodology for model parameter identification from physical component tests.
- Give directions for rubber bushing modelling in MBS models.

Physical testing has been conducted to give information about the material characteristics and dynamic properties of rubber components. High filled natural rubber has higher dynamic stiffness and phase angle than low filled natural rubber. Furthermore, high filled natural rubber has a stronger amplitude dependence than low filled natural rubber.

The general dynamic behaviour of the rubber components (i.e. shear specimens and cylindrical bushings) is that dynamic stiffness and phase angle decrease with increasing amplitude, whereas they increase with increasing frequency. (The phase angle increases with increasing amplitude for some low amplitudes). Non-linear elasticity appears at large displacements.

The hydrobushing consists of natural rubber and cavities partly filled with a fluid (glycol). It is designed to give high vibration isolation for low amplitudes (typically 0.1-0.2 mm) and a specific frequency (typically 15-20 Hz). The dynamic characteristics of the hydrobushing have a very strong frequency dependence, which is logical since there is a fluid in the bushing. The maximum damping (phase angle) for the hydrobushing is much higher than for the other components.

An important conclusion from the physical testing is that the amplitude and frequency dependence of the rubber components (i.e. shear specimens and cylindrical bushings) are uncoupled. However, the amplitude and frequency dependence are coupled for the hydrobushing.

Different bushing models have been validated against physical test data. The viscoelastic models (Kelvin-Voigt, Zener, and generalized Maxwell) describe the behaviour of the components very poorly, because the inability to show amplitude dependence.

The non-linear elastic generalized viscoelastic elastoplastic model captures the behaviour of the rubber components (i.e. shear specimens and cylindrical bushings) in a satisfying manner. The linear elastic generalized viscoelastic elastoplastic model is useful for displacements that show linear elastic behaviour.

The bushing models presented in this Master's dissertation are unable to accurately model the hydrobushing. The hydrobushing has as mentioned coupled amplitude and frequency dependence and the bushing models are only able to model uncoupled amplitude and frequency dependence. The hydro bushing is therefore poorly modelled. A proposed model that more accurately should describe the behaviour of the hydrobushing is discussed in Chapter 9.

Chapter 9

Future work

Suggestions for future work within the field of rubber component modelling are listed below:

- The studied approach for bushing modelling is based on model parameter identification from physical component tests. Physical measurements are expensive, it is therefore desirable to reduce the number of measurements. A method to reduce the number of measurements,which does not significantly impact the accuracy of the model, would be valuable.

- Develop a bushing model that describes coupled amplitude and frequency dependence. A proposed model that possibly could describe the behaviour of the hydrobushing more accurately is illustrated in Figure 9.1. This model has amplitude and frequency dependent elements coupled in series. The model is therefore expected to describe the coupled amplitude and frequency dependence existing in the hydrobushing.

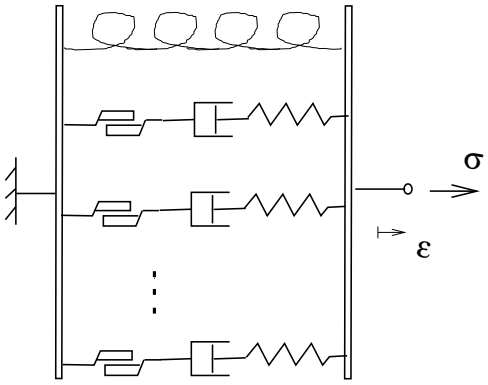

Figure 9.1: *A model consisting of non-linear elastic spring in parallel with amplitude and frequency dependent elements coupled in series.*

- Extend the 1-D bushing models to 3-D bushing models. It is desirable to develop a bushing model that describes the behaviour of the bushing in 3-D.

- Smoother friction functions in order to avoid the sharp edged hysteresis loops existing from the present frictional elements.

- Implementation of the bushing models in MBS codes such as ADAMS is necessary. It will then be possible to use the bushing models in durability, handling, and ride comfort simulations.

- The car is exposed to loads from for example the engine and road. These loads have different amplitudes and frequencies so it is necessary to study how accurate the models describe the combined loads from for example the road and engine. Evaluation of the model response for transitions between amplitudes is an important continuation of this work.

- There are so-called jounce bumpers in the wheel suspensions of a car. When driving over a rough road or a transient obstacle, the jounce bumpers are subjected to shock loads. It is important to have an accurate modelling of the jounce bumpers since the shock loads (i.e. strength load cases) play a major role in the design of the car body and chassis components. A sophisticated model to describe the impact behaviour of a jounce bumper is welcome.

Appendix A

Mechanical properties of rubber

Appendix A serves as an introduction to the behaviour of rubber material. Most of the figures and the text in this chapter can be found in the thesis [1] written by Per-Erik Austrell. Here follows a brief description of molecular structure, manufacturing process, and mechanical properties.

A.1 Molecular structure and manufacturing process

Rubber is a collective name for a broad group of materials with different chemical composition but similar molecular structure and mechanical properties. The word "rubber" originates from the pencil lead erasing property of natural gum rubber. The fact that all rubber materials are highly elastic polymers is the origin of the alternative and more descriptive name *elastomer*.

There are elastomers made from a wide variety of organic substances, but they are all polymers with very long molecular chains. The raw elastomeric material can be either natural or synthetic. In natural rubber, the sap of a tropical "rubber" tree, is coagulated in thin sheets and compressed into bales.

Natural rubber was used in the first elastomeric units manufactured, and it is still the most common material in general purpose applications. The most common synthetic rubber is made with butadiene as a base, and the main application is in car tires, because of the good abrasion resistance.

The chemical bonds between the molecular chains is of van der Waals type which is a weak chemical bond, and as a consequence the raw material is of a soft and plastic consistency. The important process of *vulcanization*, that was discovered by Charles Goodyear in 1839, converts the plastic raw elastomeric material into a solid and elastic consistency. Vulcanization is a chemical process where the long molecular chains are linked together by bonds much stronger than the van der Waals bonds, and thereby forming a stable and more solid molecular structure. The cross linking is enabled by a small amount of sulfur that is mixed with the plastic raw material. When the mixture is heated to about 170^o C the vulcanization process starts and

Figure A.1: *Molecular structure for a carbon-black-filled rubber vulcanizate. Carbon particles, polymer chains, and cross-links are schematically illustrated.*

cross-links are formed, connecting the molecular chains.

Fillers such as *carbon-black* are added in order to increase the stiffness of the material or, for some applications, to increase the resistance to wear. Carbon-black consists of very small particles of carbon (20 nm - 50 μm) that are mixed into the raw rubber base before vulcanization. The individual filler particles are stronger joined to the elastomeric material than they are joined together i.e. filler to filler. The chemical bonds between filler to filler is of van der Waal type. The filler and the elastomeric material can therefore be regarded as separated phases in the vulcanized rubber.

The rubber phase forms a continuous network, and the filler material forms agglomerates inside the rubber network. The material is thus a two-phase material made from constituents with completely different mechanical properties. Figure A.1 shows schematically the structure on a molecular level of a carbon-black-filled vulcanizate. The polymer chains are shown as solid lines and the cross-links between filler and polymer chains are shown as dashed lines.

Vulcanization and shaping are combined in the so-called *moulding* process. The rubber-filler mix is inserted into the mould cavity and heated to the appropriate temperature, and the vulcanization starts. The curing time is dependent on the temperature, the size of the unit and on how well heat is transferred to the unit.

Elastomeric units in technical applications are often composed of both rubber and steel. The attached steel parts are used to connect the rubber unit to other structures or to increase the stiffness of the unit. It is possible to attach steel parts to the rubber material in the moulding process. The steel parts are bonded, very efficiently, to the rubber. The bond is stronger than the rubber material itself in the sense that a rupture in a properly manufactured rubber-steel unit usually occurs in the rubber and not at the bonding surface between rubber and steel.

A.2 Mechanical properties

The main specific properties of elastomeric materials taken advantage of in engineering applications are the ability to sustain large straining without permanent deformation, the vibration damping property, and the resistance to wear.

The *elastic property* is the most prominent characteristic feature of vulcanized rubber. The ability to store large amounts of strain energy and to release most of it in unloading is a primary function. The molecular structure enables it to undergo large deformations and recover almost completely in unloading. However, the material becomes less elastic and more leathery as more filler is mixed into the compound.

The elasticity of rubber is due to the long tangled molecular chains and their ability to stretch and orient themselves in the direction of straining. This is possible because the repeated molecular units in the polymer can rotate freely about the bonds joining the units. Elongations of several hundred percent are possible.

Another characteristic feature of rubber is the large difference between the shear modulus and the bulk modulus. A typical carbon-black-filled rubber vulcanizate for technical applications has a shear modulus of about 1 MPa and a bulk modulus of about 2000 MPa. The large volumetric stiffness compared to the shear stiffness indicates a *nearly incompressible* behaviour. In many applications complete incompressibility is a good assumption.

Although rubber is a highly elastic material it is not perfectly elastic. A differ-

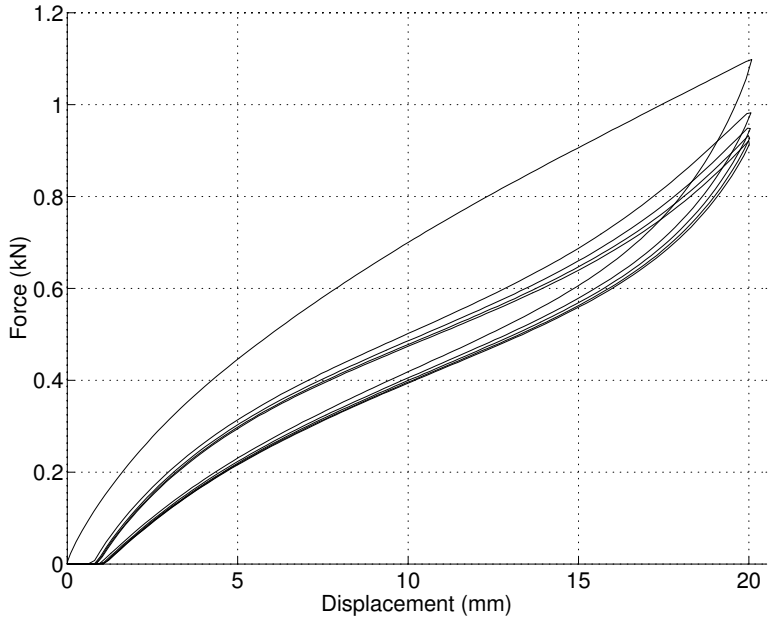

Figure A.2: *Force-displacement relations for a rubber vulcanizate exposed to cyclic loading. The so-called Mullins' effect can clearly be seen.*

ence is always observed between the loading and unloading curves in a stress-strain diagram. This phenomenon is referred to as *hysteresis*, and it is illustrated in Figure A.2 for a carbon-black-filled rubber in planar tension. In cyclic loading there is thus always a part of the energy that is not recoverable. The area enclosed by the loading and unloading curves represents energy dissipated mainly as heat. In free vibrations this causes the amplitude of the vibrations to decrease, and this material property is therefore termed *damping*. Adding fillers to the rubber compound increases the damping.

Stress softening or *Mullins'* [8] *effect* is another phenomenon which has to be considered. This decrease in stiffness by straining is seen in Figure A.2. If a previously unstrained rubber specimen is exposed to cyclic loading up to a specific strain level, the maximum stress and the distance between the loading and unloading curves will decrease in the first few load cycles. After about three to five load cycles a steady state will be reached at this specific maximum strain level. If the specimen is exposed to a new set of cyclic straining to a higher strain level, there will be a new decrease in stress and hysteresis until a new steady state is reached. The strain softening behaviour originates from a gradual breakdown of molecular crosslinks and to configurational changes in the rubber network, with increasing strain.

In order to get stationary values in the testing of rubber specimens it is thus necessary to pre-strain the specimens before conducting the actual recording of corresponding force-displacement values. This is called *mechanical conditioning*.

The filler phase has a very small stress carrying capacity as compared to the rubber phase. The filler particles can be regarded as rigid inclusions embedded in the rubber matrix. Consequently, the stress and strain in the rubber phase will reach higher levels in elastomeric units with filler added than in an equally loaded and identical unfilled unit. The filler will also affect the maximum elongation (at break), which is lowered by adding fillers. This effect of the filler on the rubber phase is called *strain amplification*.

Stiffness of a rubber vulcanizate is classified by a value of *hardness*. It is measured by an indentation test with a ball or needle with a spherical tip. A constant force is applied and the indentation depth is measured. There are two methods, the IRHD test (International Rubber Hardness Degrees) which is also the ISO standard test, and the Shore Hardness test. The scales of the tests are almost identical for rubbers in the range of 30-80 IRHD where most rubber mixes belong. The hardness test gives an indirect measure of the elastic modulus. This is sometimes the only value available for the modulus of the material. The relationship between the shear modulus G and hardness is indicated in Figure A.3. The diagram is constructed from Lindley [6] (Table 3, p. 8).

Simple shear is more linear than other homogeneous modes of deformation. The shear modulus is quite independent of the shear strain and it can therefore be regarded as a material constant at least for moderate strains. This is not the case for Young's modulus as can be seen in Figure A.4, where loading curves in compression/tension and simple shear are shown for a 60 IRHD carbon-black-filled natural

rubber vulcanizate. (The curve illustrating the uniaxial state of stress is composed of a tension test and a compression test.) The behaviour of rubber in compression is progressive. For tension and simple shear the behaviour is first degressive and then progressive for large strains.

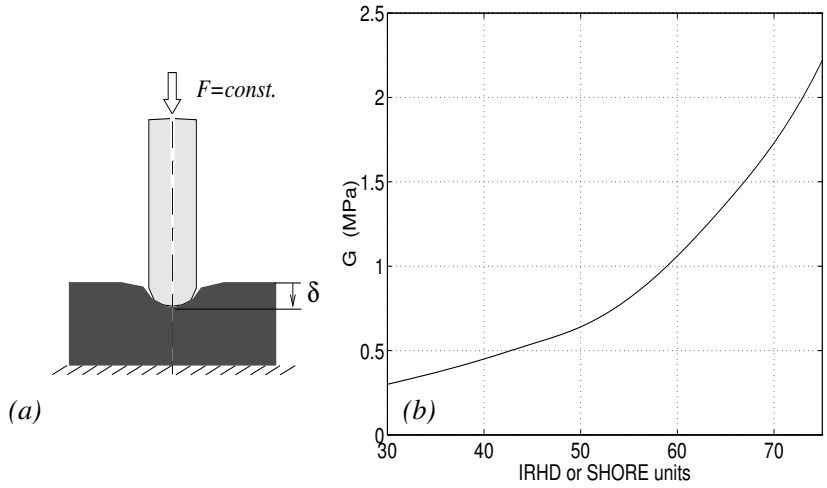

Figure A.3: *(a) An indentation test is conducted with a ball or needle with a spherical tip.(b) Relationship between the shear modulus G and the hardness in IRHD or SHORE units.*

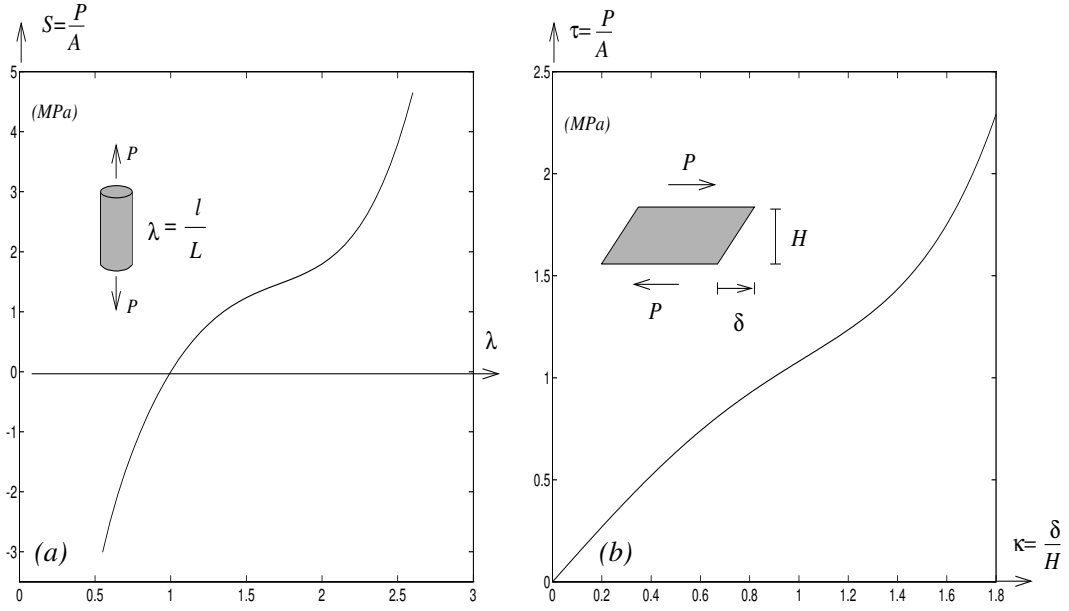

Figure A.4: *Homogeneous deformations of a 60 IRHD rubber, (a) uniaxial state of stress and (b) simple shear.*

A.3 Microstructure and dynamic properties

The origin of the damping property of rubber can be understood from the molecular structure of the material. Vulcanized rubber is made up of very long cross-linked polymer molecules. The damping is increased when filler, usually carbon-black, is added to the rubber compound. Carbon-black consists of very small particles of carbon (20 nm - 50 μm), which are mixed into the raw rubber base before vulcanization. The material is thus a two-phase material made up of constituents with completely different mechanical properties. Figure A.1 shows schematically the structure at a molecular level of a carbon-black-filled vulcanizate. The cross-links are shown as dashed lines and the carbon particles forms agglomerates inside the rubber network (solid lines).

The damping property of filled rubbers, i.e. the ability to dissipate mechanical energy into heat, is mainly due to two kinds of mechanisms. One is of viscous character - the origin of the viscous damping being the resistance in reorganization of the molecular chains within the rubber phase. This reorganization of the long molecular chains can not occur instantaneously, giving a rate dependent resistance of a viscous character. The other mechanism is due to the filler; damping is increased by adding fillers to the rubber compound. The filler particles can be regarded as rigid compared to the stiffness of the rubber matrix. The filler particles, as mentioned above, form agglomerates and these build a filler structure inside the rubber network. When the composed rubber material is being deformed there will be forces developing in the filler interfaces and the filler structure will break. The increased damping must therefore be attributed to a resistance in the rubber-carbon interfaces and in the carbon-carbon interfaces. It will be argued that this part of the damping is rate-independent and responsible for the non-linear dynamic behaviour of filled rubbers that appears as amplitude dependence of the dynamic stiffness and phase angle.

A.3.1 Stationary dynamic properties

There will be differences between loading and unloading curves in a force-displacement diagram when a cyclic load is applied on a rubber material. This phenomena is termed *hysteresis*. The energy which is dissipated in each cycle is represented by the enclosed area U_c created by the loading and unloading curves cf. Figure A.5. This energy dissipates mainly as heat. It is the dissipated energy that causes the amplitude of the vibration to decrease, and this material property is therefore termed *damping*. As mentioned earlier the damping will increase if more filler is added into the rubber compound.

Linear dynamic is characterized by sinusoidal response to sinusoidal excitation. The response is of the same frequency but shifted by a phase angle δ. Figure A.5(a) corresponds to linear (viscoelastic) behaviour, which is characterized by a pure elliptical form. Figure A.5(b) is more general where non-linearities are present. The non-linear behaviour appears as a distortion of the hysteresis loop. These non-

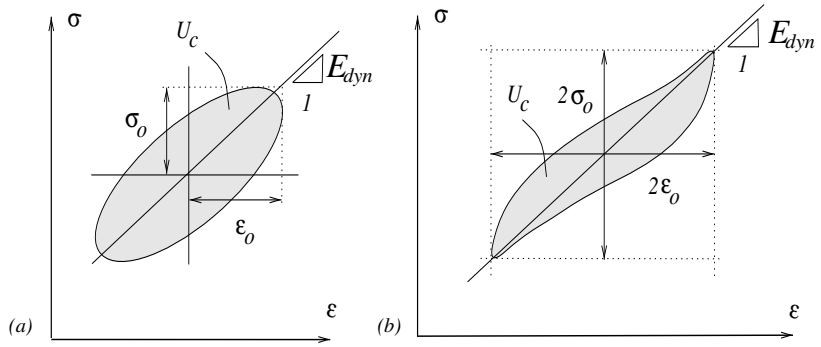

Figure A.5: *Linear viscoelastic (a) and general (b) hysteresis loop for harmonic excitation.*

linearities are due to non-linear elasticity and/or frictional damping (filler structure breakdown and reforming).

On the basis of a steady state harmonic excitation which is an important loading case, the *dynamic modulus* is defined according to Figure A.5 as

$$E_{dyn} = \frac{\sigma_0}{\epsilon_0} \tag{A.1}$$

Note that the dynamic modulus for the non-linear case is not unambiguous by this definition since the same dynamic modulus can be achieved with different hysteresis (if σ_0 and ϵ_0 is the same).

The dissipated energy U_c for each strain cycle is related to the phase angle δ according to $U_c = \pi\sigma_0\epsilon_0 \sin(\delta)$. This expression is derived in connection with linear viscoelastic models in Appendix B and is only valid for linear viscoelastic materials. The *normalized damping* d is defined according to

$$d = \sin(\delta) = \frac{U_c}{\pi\sigma_0\epsilon_0} \tag{A.2}$$

For moderate damping, $\sin(\delta) \approx \delta$, it is concluded that the normalized damping d will coincide with the phase angle (loss angle).

The dynamic properties of rubber are dependent on frequency, temperature, static load, and amplitude.

Frequency dependence

Figure A.6 shows the frequency dependence of the dynamic modulus and phase angle for a filled rubber. The dynamic shear modulus and phase angle are shown as function of frequency. The effect of changing the temperature is also shown in the figure. The values given are approximate and strongly dependent also on the amplitude, which will be discussed below.

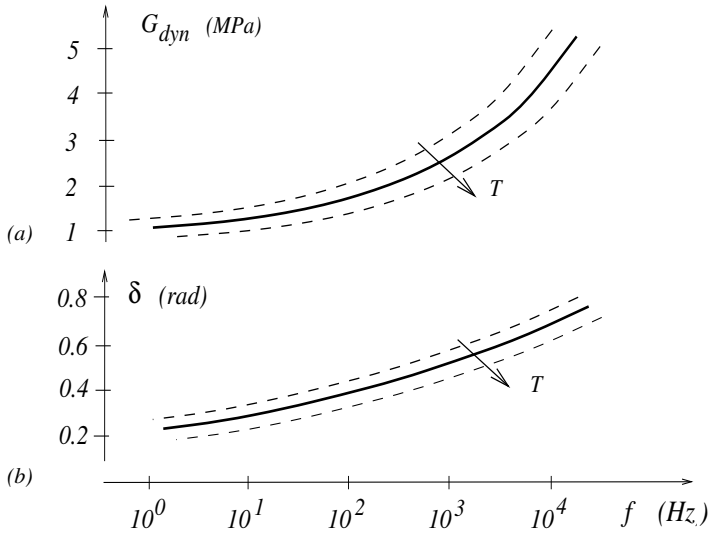

Figure A.6: *Frequency dependence of dynamic shear modulus (a) and phase angle (b) for a filled natural rubber. Influence of temperature is also shown.*

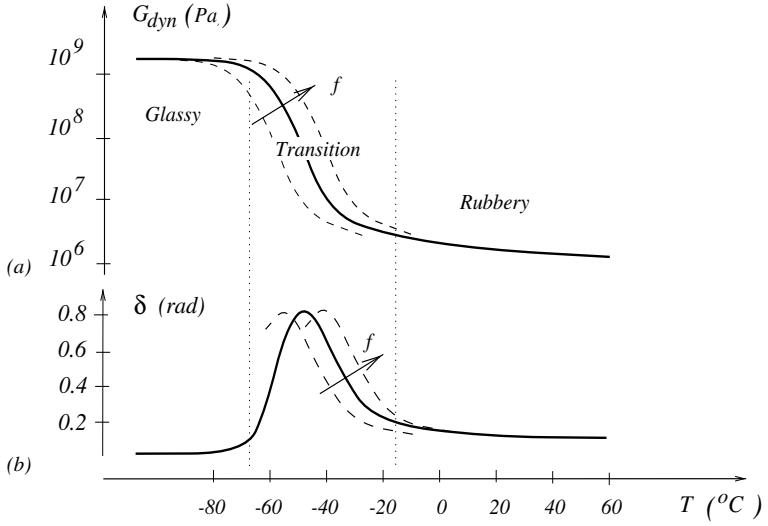

Figure A.7: *Temperature dependence of dynamic shear modulus (a) and phase angle (b) for a filled natural rubber. Influence of frequency is also shown.*

Temperature dependence

Figure A.7 shows the temperature dependence of the dynamic shear modulus and phase angle for a filled rubber. Values given are approximate and dependent also on the amplitude. The dynamic modulus decreases, with increasing temperature. The effect of changing the frequency is also shown in the figure. The general behaviour shown in Figure A.7 is the same for all rubbers, although the temperature scale can be shifted by additives in the rubber compound.

Three temperature regions are indicated. The first is the glassy region where the

thermal motion of the polymer molecules is reduced. In this range, almost no intermolecular motion is possible and the material is glass-like and brittle. Mechanical behaviour of rubber in this temperature range is dependent on the inter-atomic bonds. The modulus is therefore considerably high (≈1 GPa) in this region, while damping represented by the phase angle is low. The second region is the transition region, with a drastic drop in dynamic modulus and with maximum damping shown as a peak in the phase angle. The third temperature region is the rubbery region with a considerably low dynamic modulus (≈1 MPa). Rubbers in working conditions must be in the end of the transition region or in the rubbery region in order to have rubber-like properties.

Amplitude dependence

Special emphasis will here be put on strain amplitude dependence of the dynamic modulus. The modulus is seen to decrease with increasing strain amplitude. This effect is sometimes denoted the *Payne effect* due to investigations of reinforced elastomers made by Payne [10]. He interpreted the decline in modulus for increasing strain amplitude as a result of breaking of the filler structure. The structure is composed of aggregates held together by van der Waals bonds. Payne found that the modulus is almost recoverable upon return to small amplitudes, i.e. the filler structure largely reforms for an amplitude cycle. It is clear that the mechanisms involved should not be confused with the Mullins' effect, which is attributed to breaking of the cross-links between the filler and elastomeric material with recovery times of about 24 hours. To sum up, it canbe concluded that the Payne effect has a short recovery time while the Mullins' effect has a long recovery time.

Payne also observed that the shape of the decline in modulus for increasing strain amplitude was almost independent of frequency for low frequencies.

Harris and Stevenson [5] have made experimental investigations of several non-

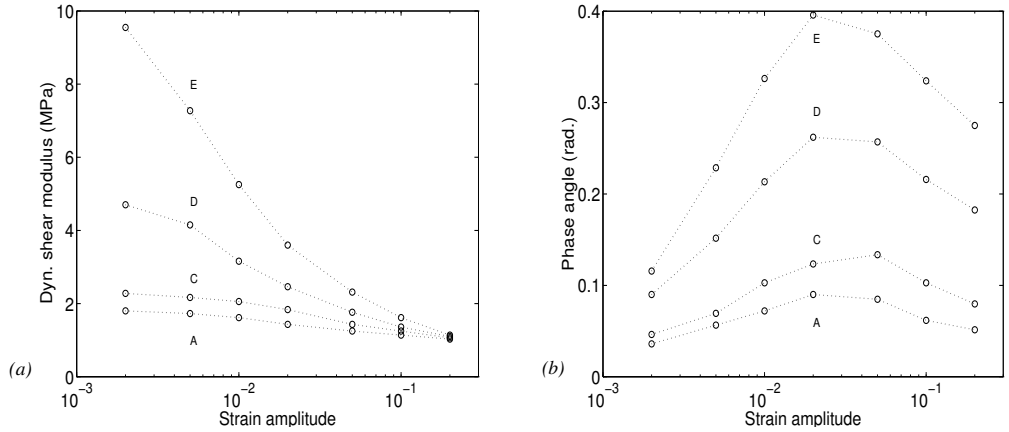

Figure A.8: *Amplitude dependence of dynamic shear modulus (a) and phase angle (b) for some filled natural rubbers with various filler content. A-E represent increasing filler content. (Reproduced from Harris and Stevenson.)*

linear aspects of the dynamic behaviour of, especially, filled rubbers. They investigated effects of frequency, amplitude, and elastic non-linearity for filled and unfilled rubbers. For unfilled rubbers it is clearly seen that the hysteresis loop has an elliptic shape for small amplitudes and preload and the behaviour is viscoelastic. For filled rubbers a significant effect of the strain amplitude on the dynamic modulus is reported. Figure A.8 shows the strain amplitude dependence of the dynamic shear modulus and phase angle, reproduced from [5], for natural rubbers (NR) with different carbon-black loading. The amount of black varied from 30 phr (parts per hundred of NR by weight) to 75 phr. The rubbers are all of approximately the same hardness (about 55 IRHD). This was accomplished by using three different types of carbon-black and by balancing the reinforcing effect by addition of a high-viscosity aromatic oil. Figure A.8 shows the strain amplitude influence in simple shear. The vulcanizates are denoted A, B, C, D, and E in [5] in order of increasing reinforcement of carbon-black. The carbon-black content varied from 30 to 75 phr (75 phr for vulcanizate E). Vulcanizate B and C behaved similarly. B is therefore left out in the reproduction (cf. Figure A.8). The vulcanizate with the highest damping and variation in dynamic modulus is the one with the highest filler content.

Harris and Stevenson also report that the stress response for harmonic loading in simple shear is influenced by higher harmonic components, resulting in a distorted elliptic shape which tends towards a parallelogram. The most significant contribution is from the third harmonic component. The ratios of the third and the first harmonic component are reported for vulcanizate specimen E for a 1 Hz test at different amplitudes. The maximum ratio is 0.035 for a strain amplitude of 5%.

The shape of the shear strain has a very small influence in quasi-static tests. For example a test with triangular shaped periodic shear load and sinusoidal shear load yields almost the same hysteresis, according to [1].

It has been mentioned that the dynamic modulus decreases for increasing strain amplitude. It is therefore interesting to discuss the reversibility for rubber. The influence of damage on the amplitude dependence of the dynamic modulus is not too severe. Most of the decline in dynamic modulus is recoverable and the damage plays a minor role, according to [1].

An important property of the dynamic behaviour of filled rubbers is the separability of rate and amplitude effects, as illustrated in Figure A.9. This phenomena is fundamental for the modelling in this Master's dissertation.

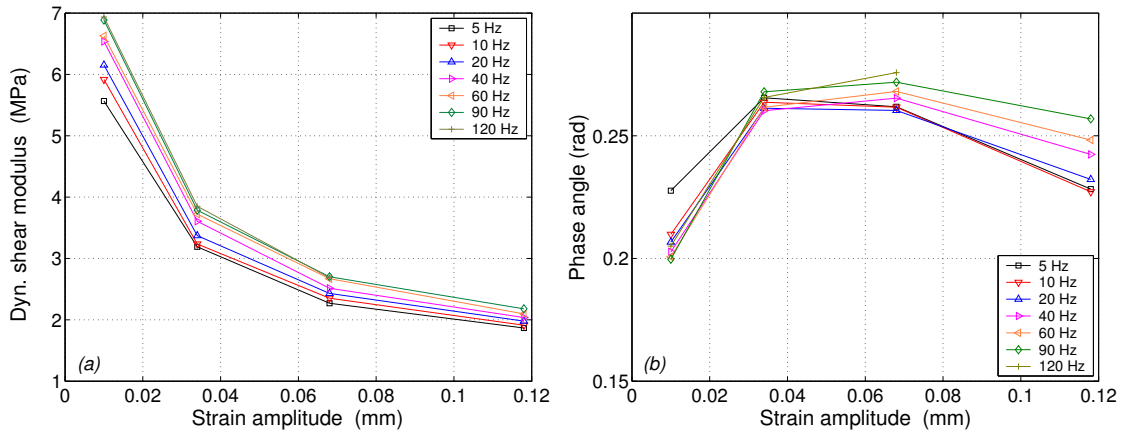

Figure A.9: *Separation of rate and amplitude effects. Dynamic shear modulus (a) and phase angle (b) as function of strain amplitude for different frequencies. Natural rubber with the hardness 60 shore.*

A.4 Summary

Deviations from linear dynamic behaviour are caused by the underlying non-linear elastic properties and/or by the damping mechanisms introduced by the filler.

For unfilled rubbers, a linear viscoelastic behaviour can be observed in simple shear, which is a linear mode of deformation if the strains are not too large. In the case of filled rubbers, non-linear dynamic behaviour is present even for simple shear due to breakdown and reforming of the carbon-black structure.

Important mechanical and dynamic properties of carbon-black-filled natural rubbers are summarized here.

- Payne interpreted the decline in dynamic modulus for increasing strain amplitude as a result of breaking of the filler structure. Payne found that the modulus is almost recoverable upon return to small amplitudes, i.e. the filler structure largely reforms for an amplitude cycle.

- Mullins' effect is attributed to breaking of the cross-links between the filler and elastomeric material, which results in decline in dynamic modulus for increasing strain amplitude. This breaking of cross-links between the filler and elastomeric material has a recovery time of about 24 hours.

- The dynamic modulus is almost recoverable for a strain cycle with increasing amplitude followed by decreasing amplitude in harmonic testing. The mechanisms on microstructural level involved must therefore be different from the mechanisms involved in the Mullins' effect. The explanation lies in the breakdown and quick reforming of the carbon-black structure.

- On the basis of steady state harmonic excitation, the dynamic modulus is defined according to Figure A.5 and equation (A.1) as $E_{dyn} = \sigma_0/\epsilon_0$. It is obvious that this definition is not unambiguous when non-linearity appears.

- The normalized damping is defined according to equation (A.2) as $d = U_c/(\pi\sigma_0\epsilon_0)$. As the dynamic modulus is not the damping unambiguous when non-linearity appears.

- In quasi-static loading, it can be observed that a difference between loading and unloading curves is present irrespective of how low the loading rate is, according to [1]. It can also be observed [1] that the hysteresis loop in quasi-static loading of heavily filled rubber takes the approximate shape of a parallelogram.

- The shape of the strain history in quasi-static loading does not appreciately influence the shape of the hysteresis loop. Triangular shaped periodic shear strain and sinusoidal shear strain in quasi-static loading gives almost the same hysteresis loops, according to [1].

- In harmonic loading, it can be observed that the dynamic modulus shows a considerable amplitude dependence. The modulus declines with amplitude towards an asymptotic value for large amplitudes. The damping represented by the equivalent phase angle reaches a maximum where the decline in modulus is the greatest (cf. Figure A.8).

- The shape of the decline of the dynamic modulus with amplitude is insensitive to frequency. Experiments indicate that the amplitude and frequency dependence are separable (cf. Figure A.9).

Appendix B

Material models for rubber

Appendix B concerns one dimensional material models which constitute the basis for the modelling of rubber components. Linear viscoelastic models are first discussed, then elastoplastic models. Most of the figures and the text in Appendix B are copied from the PhD thesis by Per-Erik Austrell [1].

A starting point for the modelling of damping in filled rubbers is the simple one-dimensional model of elastic and damping properties shown in Figure B.1. The elastic behaviour is provided by the spring element, which is assumed to be non-linear. Damping is modelled by the rate-dependent viscous damper and the rate-independent frictional element. The frictional element makes it possible to model hysteresis in quasi-static load cases, i.e. when the strain rate approaches zero.

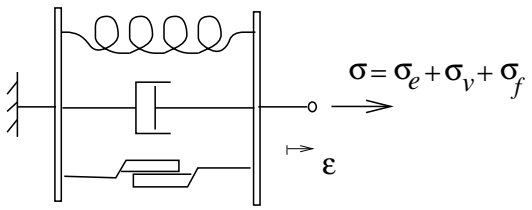

Figure B.1: *Simple one-dimensional rheological model including non-linear elastic, viscous, and frictional properties.*

The elastic, viscous, and frictional forces act in parallel, and the total stress is the sum of the stresses in the elements, i.e. $\sigma = \sigma_e + \sigma_v + \sigma_f$. The viscous stress σ_v corresponds to dissipative stresses in the rubber network. Stresses in the filler phase and in the rubber-filler interfaces are responsible for the rate-independent contribution σ_f.

This model incorporates some important aspects of the mechanical behaviour of filled rubbers. Frequency dependence, effects of static load on the dynamic modulus, distortion of the elliptic shape of the hysteresis loop, and amplitude dependence are properties of the simple model. However, it has some unphysical properties, e.g. discontinuous stress response for continuous strain and inability to exhibit relaxation behaviour. More sophisticated models are therefore needed.

B.1 Non-linear elasticity

A material where the stress can be defined by a strain energy function W is termed *a hyperelastic material*. The strain energy function can be regarded as a potential function for the stresses i.e. stresses are determined by derivatives of the strain energy function. In this section the concept of hyperelasticity will be illustrated by a non-linear elastic bar. Also hyperelastic models like Neo-Hooke and Yeoh are discussed. Finally the stress and strain relation in simple shear will be derived.

B.1.1 Non-linear elastic bar

Consider the non-linear elastic bar, illustrated in Figure B.2, with original length L and cross-section area A. The force P causes the displacement u at the end of the bar and increases its length to l giving the stretch $\lambda = l/L$.

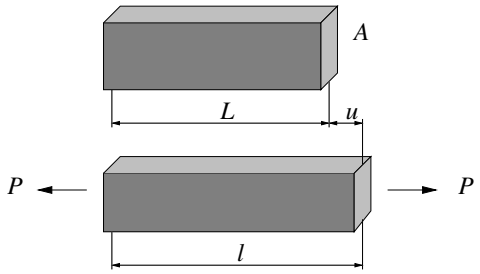

Figure B.2: *Non-linear elastic bar loaded by a force P.*

The uniaxial stress-stretch relation will be derived here for a uniaxial state of stress. This is done by introducing the strain energy function $W(\lambda)$ with W the strain energy per undeformed volume of the bar and λ the stretch, defined as the length ratio of the deformed and undeformed bar.

The total strain energy U is computed by multiplying the strain energy density W with the volume, i.e.

$$U = AL\,W(\lambda)$$

The incremental work done by the external force P should be equal to the increment in total strain energy. Hence, the energy balance is stated as

$$P du = dU \tag{B.1}$$

and the increment in total strain energy can be expressed by use of W as

$$dU = AL\,dW = AL\,\frac{dW}{d\lambda}\,d\lambda \tag{B.2}$$

The displacement increment can also be written in terms of stretch by using

$$u = l - L = (\lambda - 1)L$$

Differention yields

$$du = Ld\lambda \tag{B.3}$$

Inserting (B.3) and (B.2) into the energy balance equation (B.1) yields

$$PLd\lambda = AL\,\frac{dW}{d\lambda}\,d\lambda$$

Simplifying the expression gives

$$\frac{P}{A} = \frac{dW}{d\lambda} \tag{B.4}$$

where P/A is the nominal stress, i.e. force per original cross section area, derived from the strain energy function.

It is seen from this one-dimensional example that the stress can be obtained directly from the strain energy density function. In the general multiaxial case the stresses are found in a similar manner from the strain energy density function.

B.1.2 The Neo-Hooke material

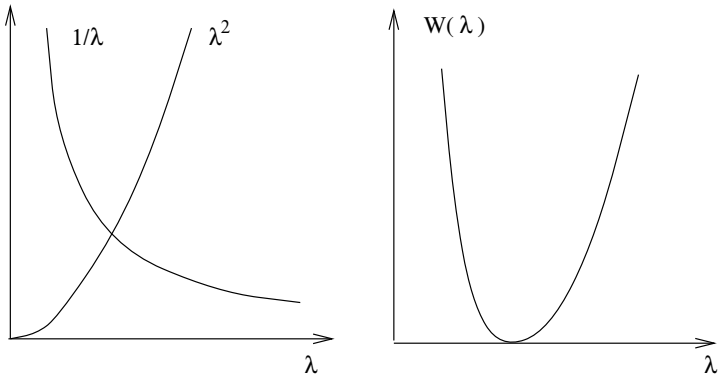

Figure B.3: *Strain energy function $W(\lambda)$ constructed from a simple choice of functions.*

The strain energy function $W(\lambda)$ has to fulfill some general conditions:

- $W(1) = 0$ for $\lambda = 1$, i.e. the strain energy is zero in the unloaded case.
- $W(\lambda) \to \infty$ for $\lambda \to 0$ and for $\lambda \to \infty$, i.e. the strain energy should increase for increasing compression and tension.
- $dW/d\lambda = 0$ for $\lambda = 1$, the nominal stress has to be zero in the unloaded state.

A strain energy function can be constructed from a simple choice of functions by using $1/\lambda$ and λ^2 according to Figure B.3. A function that satisfies these conditions is given by

$$W(\lambda) = C(\lambda^2 + \frac{2}{\lambda} - 3) \tag{B.5}$$

Inserting (B.5) into (B.4) results in

$$\frac{P}{A} = 2C(\lambda - \frac{1}{\lambda^2}) \tag{B.6}$$

where C is an arbitrary material constant. Equation (B.6) is the nominal stress in the so-called Neo-Hooke material, which is the simplest possible hyperelastic model, with only one material parameter.

B.1.3 Yeoh material

In [1] it is concluded that for a material which is assumed to be isotropic the strain energy function W can be expressed as a function of the strain invariants i.e.

$$W = W(I_1, I_2, I_3)$$

with the strain invariants

$$\begin{cases} I_1 = {\lambda_1}^2 + {\lambda_2}^2 + {\lambda_3}^2 \\ I_2 = {\lambda_1}^2{\lambda_2}^2 + {\lambda_1}^2{\lambda_3}^2 + {\lambda_2}^2{\lambda_3}^2 \\ I_3 = {\lambda_1}^2{\lambda_2}^2{\lambda_3}^2 \end{cases} \tag{B.7}$$

In the case of an *incompressible* material there is no dependence on the third strain invariant, because this invariant expresses the volume change, giving

$$W = W(I_1, I_2) \tag{B.8}$$

A general form of (B.8) is given by the series expansion

$$W = \sum_{i=0,j=0}^{\infty} C_{ij}(I_1 - 3)^i(I_2 - 3)^j \tag{B.9}$$

where C_{ij} are unknown constants. The sum is formally written as a sum to infinity, but normally only few terms are used. The explicit version of (B.9), with the terms having an index sum less or equal to three, is written as

$$\begin{aligned} W = {} & C_{10}(I_1 - 3) + C_{01}(I_2 - 3) \\ & + C_{20}(I_1 - 3)^2 + C_{11}(I_1 - 3)(I_2 - 3) + C_{02}(I_2 - 3)^2 \\ & + C_{30}(I_1 - 3)^3 + C_{21}(I_1 - 3)^2(I_2 - 3) + C_{12}(I_1 - 3)(I_2 - 3)^2 + C_{03}(I_2 - 3)^3 \\ & + \text{..... .} \end{aligned}$$

Taking terms that include I_1, I_1^2, I_1^3 and $I_1 I_2$ then the *third order of deformation* is obtained i.e.

$$W = C_{10}(I_1-3)+C_{01}(I_2-3)+C_{20}(I_1-3)^2+C_{11}(I_1-3)(I_2-3)+C_{30}(I_1-3)^3 \tag{B.10}$$

which is a model with five parameters.

Yeoh [11] found that the dependence on the second invariant is very weak for carbon-black-filled natural rubbers. By leaving out terms in (B.10) that include I_2 Yeoh obtained a model with three parameters that gave a good fit to experiments carried out on filled rubbers. Consequently, this strain energy function is written as

$$W = C_{10}(I_1 - 3) + C_{20}(I_1 - 3)^2 + C_{30}(I_1 - 3)^3 \tag{B.11}$$

which is the so-called Yeoh material.

B.1.4 Simple shear

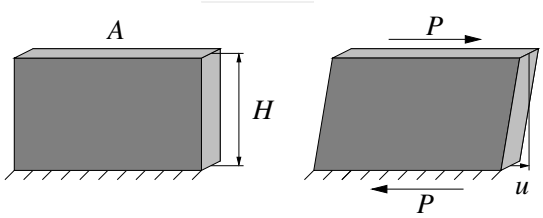

Figure B.4: *Simple shear.*

Another important state of deformation is simple shear cf. Figure B.4. The force P causes the shear strain

$$\kappa = \frac{u}{H} \tag{B.12}$$

The total strain energy U, is in similar manner as for the example of the bar, computed by multiplying the strain energy density W with volume

$$U = AHW(\kappa) \tag{B.13}$$

The incremental work caused by the external force P is equal the increment in total strain energy i.e.

$$Pdu = dU \tag{B.14}$$

Differention of equation (B.12) and equation (B.13) gives

$$\frac{du}{d\kappa} = H \tag{B.15}$$

and

$$dU = AH\frac{dW}{d\kappa}d\kappa \tag{B.16}$$

Inserting equation (B.16) in equation (B.14) gives

$$P\frac{du}{d\kappa} = AH\frac{dW}{d\kappa} \tag{B.17}$$

If the strain energy function is chosen according to Yeoh i.e. $W(I_1)$ and making use of the expression

$$I_1 = 3 + \kappa^2 \tag{B.18}$$

which is derived in [1], the chain rule gives that $dW/d\kappa$ in equation (B.17) can be written as

$$\frac{dW}{d\kappa} = \frac{dW}{dI_1}\frac{dI_1}{d\kappa} \tag{B.19}$$

From equation (B.18) it is concluded that

$$\frac{dI_1}{d\kappa} = 2\kappa \tag{B.20}$$

Inserting equation (B.20) in equation (B.19), and inserting equation (B.19) in equation (B.17) and finally making use of equation (B.15) gives

$$\tau = \frac{P}{A} = 2\frac{dW}{dI_1}\kappa \tag{B.21}$$

where

$$\frac{dW}{dI_1} = C_{10} + 2C_{20}(I_1 - 3) + 3C_{30}(I_1 - 3)^2 \tag{B.22}$$

according to equation (B.11) with use of (B.18).

B.2 Linear viscoelasticity

This section deals with different aspects of viscoelastic behaviour. Linear viscoelasticity will be illustrated for transient and periodic loading. Issues like complex modulus, creep and relaxation functions will be treated.

Viscoelastic material models combine elastic and viscous characteristics. The constitutive relations are defined in terms of time functions of stress $\sigma(t)$ and strain $\epsilon(t)$. Hence, the response becomes time dependent, in contrast to ideally elastic materials where a one-to-one relation exists between the current stresses and the current strains. The constitutive equations can be defined by an integral or by a differential equation.

Mechanical analogies consisting of spring and dashpot assemblies are often used to illustrate viscoelastic material behaviour. The mechanical behaviour of a specific viscoelastic material in a uniaxial case is analogous to the behaviour of a proper combination of springs and dashpots.

With harmonic excitation the response will be a phase shifted harmonic function with the same frequency. This property of linear viscoelasticity makes it possible to define a complex modulus independent of amplitude and a function only of frequency.

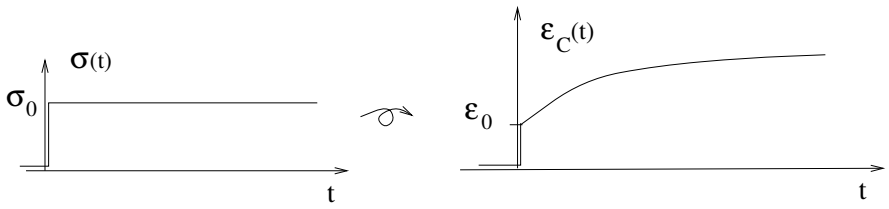

Figure B.5: *Creep behaviour; increasing strain as response to a stress step.*

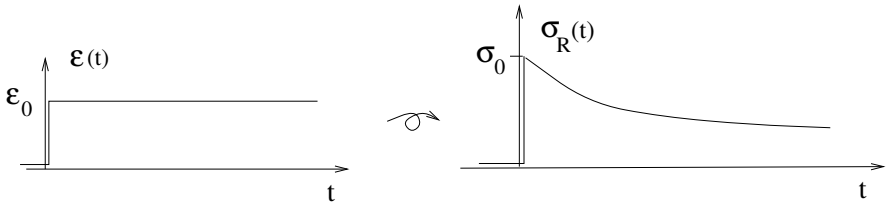

Figure B.6: *Relaxation behaviour; decreasing stress as response to a strain step.*

B.2.1 Creep and relaxation

Material behaviour explainable by linear viscoelastic models includes, for example, creep and relaxation phenomena. These are in the hereditary approach discussed below.

Creep is an increasing strain as response to a step-stress loading. Consider a bar with cross section A and length L. When a step-stress loading according to Figure B.5 is applied to the bar at time $t = 0$ the length will suddenly increase to ΔL according to:

$$\varepsilon(0) = \frac{\Delta L}{L} = \frac{\sigma_0}{E(0)} \tag{B.23}$$

where $E(0)$ is the Young's modulus at $t = 0$.

Viscoelastic materials, for example rubber, undergo creep i.e. the deformation increases with respect to time even though the stress is constant.

The phenomena *relaxation* cf. Figure B.6 is a decreasing stress as a response to a step-strain loading and depends on the same mechanisms as creep. Therefore relaxation is coupled to the phenomena creep.

There are two approaches in order to model linear viscoelasticity; one is the *hereditary* approach and the other is the *differential* approach. The *differential* approach is here used in this chapter to derive the constitutive equations for the subsequent linear viscoelastic models represented by assemblies of linear springs and dashpots. The *hereditary* approach is discussed in the next section.

To represent viscoelastic behaviour by the *hereditary* approach there is a need to introduce the creep compliance $J_C(t)$ and relaxation modulus $E_R(t)$:

- $J_C(t)$ is the strain developed in a creep test when loaded by a unit stress.
- $E_R(t)$ is the stress developed in a relaxation test when loaded by a unit strain.

For a linear viscoelastic material the creep compliance $J_C(t) = \epsilon(t)/\sigma_0$ (cf. Figure B.5) is a characteristic function independent of the stress step σ_0. This function is unique for a specific linear viscoelastic material.

For a linear viscoelastic material, the relaxation modulus $E_R(t) = \sigma(t)/\epsilon_0$ (cf. Figure B.6) is a characteristic function independent of the strain step ϵ_0. This function is unique for the specific linear viscoelastic material.

It can be shown that the instantaneous elasticity, i.e. the relationship between the creep compliance and the relaxation modulus at $t = 0$, is $E_R(0) = 1/J_C(0)$.

B.2.2 Hereditary approach

The behaviour of a linear viscoelastic material can be defined from this single step response function. Linearity and superposition (Boltzmann's superposition principle) leads to the constitutive equation defined as a convolution integral (also called hereditary integral). The stress history corresponding to any strain history can be obtained from this integral. The constitutive model is defined by the relaxation modulus, or for the inverse relation, the creep compliance.

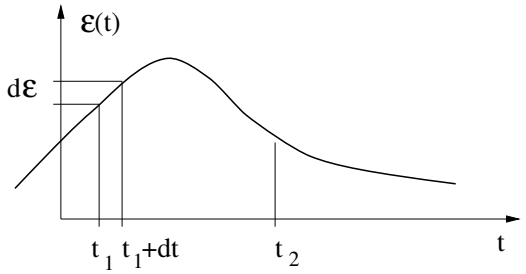

Figure B.7: *An arbitrary strain history.*

An arbitrary strain history $\epsilon(t)$, cf. Figure B.7, can be considered as a sum of a large number of differential, positive and negative strain steps. A strain step $d\epsilon$ at time t_1 causes a stress change $d\sigma$. At time t_2 the stress change has been relaxed to

$$d\sigma(t_2) = E_R(t_2 - t_1)\, d\epsilon(t_1)$$

Summation of all stress changes at time t_2 due to all previous strain steps yields

$$\sigma(t_2) = \int_{-\infty}^{t_2} E_R(t_2 - t)\, \frac{d\epsilon}{dt} dt \tag{B.24}$$

This is the *hereditary integral* that defines the linear viscoelastic stress response for an arbitrary strain history. Hence, from knowledge of the relaxation modulus the stress $\sigma(t_2)$ can be derived by (B.24) for an arbitrary strain history $\epsilon(t)$.

The inverse relation can be obtained by applying stress steps and assembling the creep histories, giving the relation

$$\epsilon(t_2) = \int_{-\infty}^{t_2} J_C(t_2 - t)\, \frac{d\sigma}{dt} dt \tag{B.25}$$

In connection with the finite element method, where strain and displacement are the basic unknown quantities, the form (B.24) defined by the relaxation modulus is preferred.

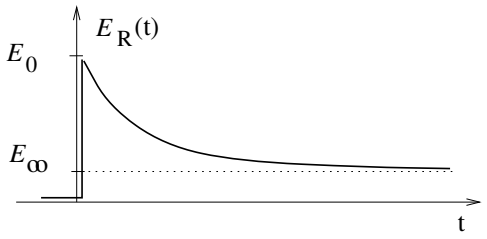

Figure B.8: *The relaxation modulus of a viscoelastic solid. E_0 is the instantaneous modulus and E_∞ is the long-term modulus.*

Linear viscoelastic theory can model both fluid and solid material behaviour. The main interest here is models for solids. It is therefore required that the creep response is limited, and that the relaxation has a limit different from zero according to Figure B.8.

An example of a relaxation process can be obtained by assuming a simple exponential law given by

$$E_R(t) = E_\infty + (E_0 - E_\infty)\, e^{-t/t_r}$$

which is the relaxation modulus associated with the so-called *Zener model*, where the parameter t_r is the relaxation time. The Zener model will be discussed further in relation to the models in Section B.3.3.

B.2.3 Harmonic excitation and complex modulus

The response to a stationary sinusoidal strain history is of interest in many engineering applications. The stress corresponding to a stationary sinusoidal strain can be expressed by a complex modulus. The constitutive relation (B.24) will be used to determine an expression for the complex modulus. Consider the sinusoidal strain in complex notation

$$\epsilon^* = \epsilon_0 e^{i\omega t} = \epsilon_0(cos(\omega t) + isin(\omega t)) \tag{B.26}$$

where the real or imaginary part is interpreted as the physical strain. Inserting (B.26) into the convolution integral (B.24) yields an expression that resembles the Fourier transform. The Fourier transform is a complex valued function depending on the parameter $\omega = 2\pi/T$ i.e. the angular frequency for the vibration, with T being the periodic time.

The form of the relaxation modulus $E_R(t)$ is inadequate for Fourier transform methods since the transform is defined only for absolute convergent functions. This requires that the function to be transformed fulfills the condition

$$\int_{-\infty}^{\infty} \mid f(t) \mid dt < \infty \tag{B.27}$$

The relaxation modulus, cf. Figure B.8, does not fulfill the requirement in (B.27). The long-term modulus E_∞ has to be separated from $E_R(t)$. A dimensionless relaxation function $e(t)$ is therefore introduced, according to

$$E_R(t) = E_\infty(1 + e(t)) \tag{B.28}$$

The function $e(t)$ has the property $e(t) \to 0 \quad$ when $\quad t \to \infty$. The dimensionless relaxation function now fulfills the requirement in (B.27) and the constitutive relation (B.24) may now be written as

$$\sigma(t_2) = E_\infty \int_{-\infty}^{t_2} (1 + e(t_2 - t)) \frac{d\epsilon(t)}{dt} dt \tag{B.29}$$

Introducing a change of variables $\tau = t_2 - t$ and substituting the complex strain (B.26) into (B.29) yields

$$\sigma(t_2) = E_\infty(1 + i\omega \int_0^\infty e(\tau) e^{-i\omega\tau} d\tau) \epsilon_0 e^{i\omega t_2} \tag{B.30}$$

In (B.30) the Fourier transform of the dimensionless relaxation function can now be identified as

$$e^*(\omega) = \mathcal{F}(e(\tau)) = \int_0^\infty e^{-i\omega\tau} e(\tau) d\tau$$

and (B.30) can now be expressed as

$$\sigma^* = E^*(\omega)\epsilon^* \tag{B.31}$$

with the complex modulus

$$E^*(\omega) = E_\infty(1 + i\omega e^*(\omega)) \tag{B.32}$$

Hence, the hereditary integral (B.24) is converted into a relation between the complex strain and stress given by a simple multiplication by a complex function, the complex modulus.

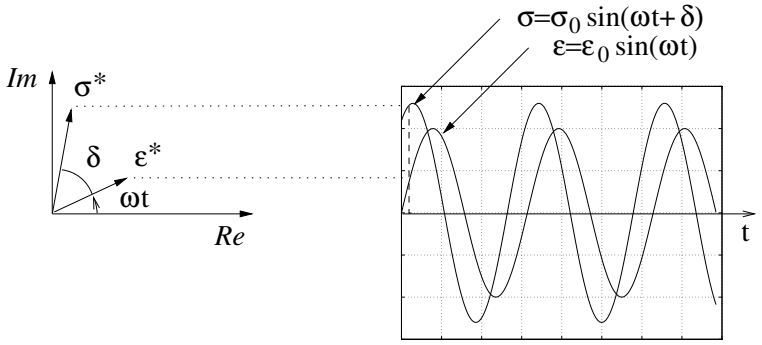

Figure B.9: *The real or imaginary part of the complex strain and stress represents the harmonic motion.*

The stress response σ^* can therefore be written as a complex number in polar form as

$$\sigma^* = \sigma_0 e^{i(\omega t+\delta)} \tag{B.33}$$

The response to a steady-state sinusoidal strain is thus a steady-state sinusoidal stress with the same frequency, but out-of-phase. The phase relationships are conveniently shown in the rotating-vector representation according to Figure B.9.

Interpretation of the complex modulus

In view of (B.31), the complex modulus can be expressed as

$$\sigma^* = \mid E^* \mid e^{iarg(E^*)}\epsilon_0 e^{i\omega t} = \mid E^* \mid \epsilon_0 e^{i(\omega t+arg(E^*))} \tag{B.34}$$

Comparing (B.34) with (B.33) yields an interpretation of the complex modulus in terms of measurable quantities according to

$$\mid E^* \mid = \frac{\sigma_0}{\epsilon_0} \quad \text{and} \quad arg(E^*) = \delta$$

i.e. the absolute value $\mid E^*(\omega) \mid$ is the amplitude ratio of stress and strain and the phase angle $arg(E^*(\omega))$ is the phase shift between stress and strain. The absolute value $\mid E^*(\omega) \mid$ is here called the *dynamic modulus* (also called the absolute modulus).

Note that the dynamic modulus and the phase angle are functions of the angular frequency ω only. Hence, for a linear viscoelastic material, the dynamic modulus is independent of the strain amplitude ϵ_0.

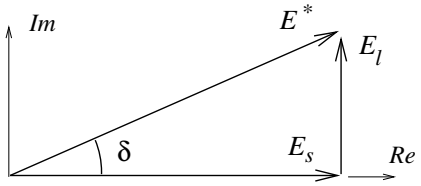

Figure B.10: *Relation between polar and rectangular form of the complex modulus.*

The complex modulus

$$E^* = \frac{\sigma^*}{\epsilon^*} = \frac{\sigma_0 e^{i(\omega t+\delta)}}{\epsilon_0 e^{i\omega t}} = \frac{\sigma_0}{\epsilon_0} e^{i\delta}$$

can alternatively be expressed in rectangular form

$$E^* = \frac{\sigma_0}{\epsilon_0} cos\delta + i\frac{\sigma_0}{\epsilon_0} sin\delta \tag{B.35}$$

where the real part E_s is termed *storage modulus* and the imaginary part E_l is termed *loss modulus*. Hence,

$$E_s = \frac{\sigma_0}{\epsilon_0}\, cos\delta \quad \text{and} \quad E_l = \frac{\sigma_0}{\epsilon_0}\, sin\delta$$

The storage modulus is said to represent in-phase response and the loss modulus is said to represent out-of-phase response, according to Figure B.10.

An alternative representation of the rectangular form is

$$E^* = E_s(1 + itan\,\delta)$$

where $tan\,\delta$ is called the *loss factor*.

The relation between the polar and the rectangular form of the complex modulus can be simplified for small values of δ. The approximate equalities $sin\,\delta \approx tan\,\delta \approx \delta$ and $cos\,\delta \approx 1$ yield

$$E_s \approx \mid E^* \mid \qquad \text{and} \qquad E_l \approx \mid E^* \mid \delta$$

For example, $\delta = 0.2$ rad yields $sin\,\delta = 0.199$, $cos\,\delta = 0.980$, and $tan\,\delta = 0.203$.

Hysteresis and energy dissipation

For cyclic loading, viscoelastic materials dissipate energy, which for instance results in damping of free vibrations. The area enclosed by the loading and unloading curves (cf. Figure B.11) represents the energy dissipated as heat.

Harmonic excitation yields harmonic response with the same frequency but out-of-phase for a linear viscoelastic material, according to the previous discussion. Consequently, if the strain $\epsilon = \epsilon_0 \sin(\omega t)$ and the stress $\sigma = \sigma_0 \sin(\omega t + \delta)$ are plotted in the (σ, ϵ)-plane, an elliptic path is obtained, as shown in Figure B.11. The hysteresis is dependent on the angular frequency ω through the complex modulus.

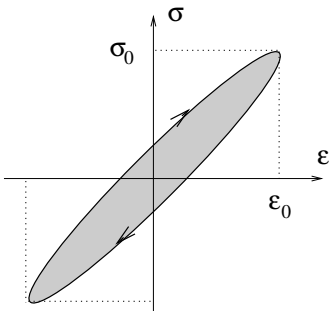

Figure B.11: *The stress $\sigma = \sigma_0 sin(\omega t + \delta)$ and the strain $\epsilon = \epsilon_0 sin(\omega t)$ plotted in the (σ, ϵ)-plane, giving an elliptical hysteresis loop.*

The energy dissipated during one cycle is

$$U_c = \oint \sigma d\epsilon = \sigma_0 \epsilon_0 \omega \int_0^T cos(\omega t) sin(\omega t + \delta) dt \tag{B.36}$$

Expression (B.36) is evaluated by using the trigonometric formula $sin(\omega t + \delta) = sin\omega t\, cos\delta + cos\omega t\, sin\delta$, giving

$$U_c = \pi \sigma_0 \epsilon_0 sin\,\delta \tag{B.37}$$

We observe that dissipated heat increases with the phase difference δ and the largest dissipation is obtained for $\delta = \pi/2$.

B.3 Viscoelastic models derived from differential equations

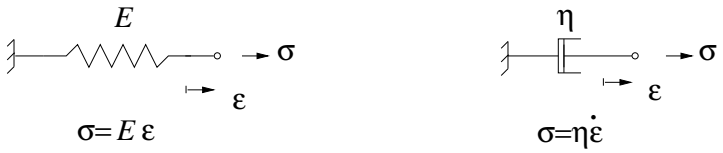

Figure B.12: *Basic elements in rheological models; the linear spring and the dashpot.*

An intuitive way to interpret and describe the nature of viscoelastic behaviour is to use mechanical analogies that consist of springs and dashpots combined together in different ways.

The spring is characterized by the modulus E (N/m^2) cf. Figure B.12, and the stress in the spring is proportional to the strain

$$\sigma = E\epsilon \tag{B.38}$$

A spring can only describe instantaneous elastic deformation.

The dashpot is characterized by the time dependent relation $d\epsilon/dt = \dot{\epsilon} = \sigma/\eta$ i.e. the stress is proportional to the strain rate

$$\sigma = \eta\dot{\epsilon} \tag{B.39}$$

where η is the coefficient of viscosity (Ns/m^2) cf. Figure B.12. A dashpot can only describe viscous deformation.

B.3.1 The Kelvin-Voigt model

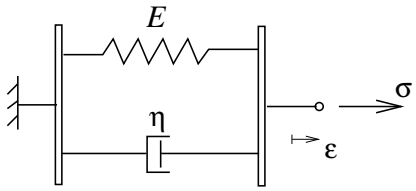

Figure B.13: *The Kelvin-Voigt model.*

To obtain the *Kelvin-Voigt model*, which is a simple viscoelastic solid model, a spring and a dashpot are connected in parallel according to Figure B.13.

Differential equation

Connection in parallel yields

$$\sigma = \sigma_{spring} + \sigma_{dashpot} \tag{B.40}$$

By inserting the relations $\sigma_{spring} = E\epsilon$ and $\sigma_{dashpot} = \eta\dot{\epsilon}$, the total stress is

$$\sigma = E\epsilon + \eta\dot{\epsilon} \tag{B.41}$$

which is the differential equation for the Kelvin-Voigt model.

Relaxation

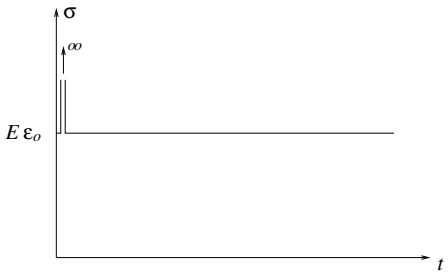

Figure B.14: *Relaxation test.*

The Kelvin-Voigt model can not exhibit relaxation. In order to deform the Kelvin-Voigt model instantaneously an infinitely large stress is required. Therefore, the stress increases instantaneously and immediately after, the stress will take the value $\sigma = E\epsilon_0$ cf. Figure B.14. This behaviour is not particularly physical and the Kelvin-Vogit model is thus a poor viscoelastic solid model.

Creep compliance

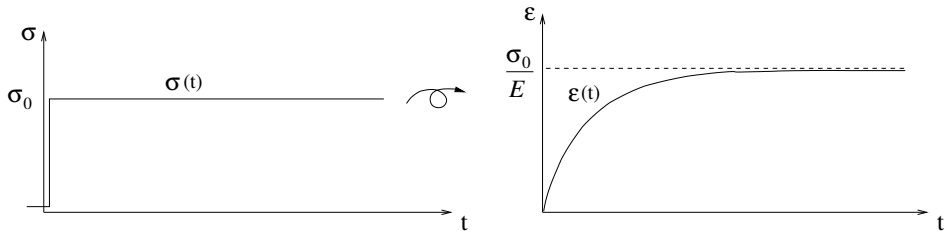

Figure B.15: *Creep behaviour of the Kelvin-Voigt model.*

The homogenous solution to (B.41) is $\epsilon = Ce^{\frac{-E}{\eta}t}$ where C is an arbitrary constant. For the case with constant stress σ_0 a particular solution to (B.41) is σ_0/E and the solution to (B.41) is therefore

$$\epsilon = \frac{\sigma_0}{E} + Ce^{\frac{-E}{\eta}t} \tag{B.42}$$

When a load is applied suddenly, the dashpot will react like a rigid member which gives the condition $\epsilon = 0$ when $t = 0$. Inserting this condition in (B.42) determines C and (B.42) can now be written as

$$\epsilon = \frac{\sigma_0}{E}(1 - e^{\frac{-E}{\eta}t}) \tag{B.43}$$

It can be seen in equation (B.43) that the strain ϵ will reach an asymptotic upper limit σ_0/E for large values of t.

From the definition of $J_C(t)$ it is concluded that

$$J_C(t) = \frac{1}{E}(1 - e^{\frac{-E}{\eta}t}) \tag{B.44}$$

Dynamic modulus

The dynamic modulus $E_{dyn}(\omega)$ can be determined by solving (B.41) for a steady state sinusoidal strain history $\epsilon = \epsilon_0 \sin(\omega t)$. The time derivative is $\dot{\epsilon} = \omega\epsilon_0 \cos(\omega t)$. Inserting the expression for ϵ and $\dot{\epsilon}$ in (B.41) and rearranging yields

$$\sigma = E\epsilon_0 \sin(\omega t) + \eta\omega\epsilon_0 \cos(\omega t) \tag{B.45}$$

Equation (B.45) can also be written as

$$\sigma = \sigma_0 \sin(\omega t + \delta) \tag{B.46}$$

where

$$\sigma_0 = \epsilon_0\sqrt{E^2 + \eta^2\omega^2} \tag{B.47}$$

and

$$\tan(\delta) = \frac{\eta}{E}\omega \tag{B.48}$$

From the definition of dynamic modulus $E_{dyn} = \sigma_0/\epsilon_0$ it is concluded that

$$E_{dyn} = \sqrt{E^2 + \eta^2\omega^2} \tag{B.49}$$

B.3.2 The Maxwell model

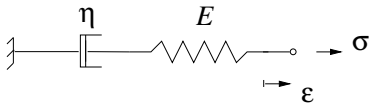

Figure B.16: *The Maxwell model.*

To obtain the *Maxwell model* the spring and the dashpot are connected in series, giving a viscoelastic fluid model. The Maxwell element is illustrated in Figure B.16. The relaxation behaviour with a totally relaxed stress suggests that the element is a simple model of a linear viscoelastic fluid. The normalized relaxation behaviour given by $E_R(t)$ is the fundamental function that defines the behaviour of a linear viscoelastic material as mentioned earlier. Hence, the stress-strain relation for a Maxwell model is found by applying a step strain and evaluating the stress response.

Differential equation

The total deformation in a Maxwell element, which consists of a spring and a dashpot in series cf. Figure B.16, is $\epsilon = \epsilon_{spring} + \epsilon_{dashpot}$. It appears that

$$\dot{\epsilon} = \dot{\epsilon}_{spring} + \dot{\epsilon}_{dashpot} \tag{B.50}$$

Inserting $\dot{\epsilon}_{spring} = \dot{\sigma}/E$ and $\dot{\epsilon}_{dashpot} = \sigma/\eta$ into (B.50) and rearranging yields

$$\dot{\sigma} + \frac{E}{\eta}\sigma = E\,\dot{\epsilon} \tag{B.51}$$

which is the differential equation that defines the stress-strain relation for the Maxwell model.

Relaxation modulus

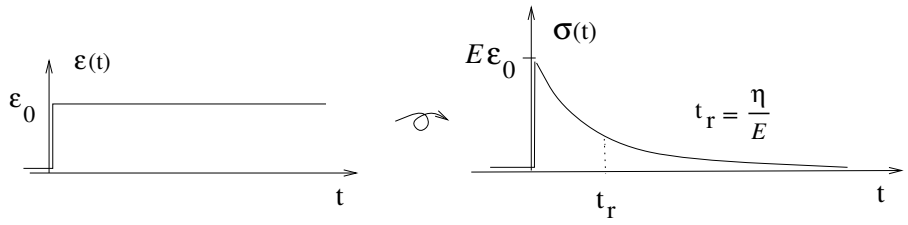

Figure B.17: *Relaxation behaviour of the Maxwell model; stress is relaxed to zero.*

The normalized relaxation behaviour $E_R(t)$ can be derived by solving (B.51) for a step strain. For $t > 0$ we have $\dot{\epsilon} = 0$, giving

$$\dot{\sigma} + \frac{E}{\eta}\sigma = 0 \quad t > 0 \tag{B.52}$$

On application of the step strain the dashpot acts as a rigid member due to the infinitely large strain rate at $t = 0$. Hence, the initial stress is defined entirely by the elastic spring, and the initial condition for the differential equation is $\sigma(0) = E\,\epsilon_0$, i.e. the instantaneous elastic response. Solving (B.52) yields

$$\sigma(t) = E\,\epsilon_0\,e^{-\frac{E}{\eta}t} \tag{B.53}$$

The step strain stress response is illustrated in Figure B.17, and we conclude that the relaxation modulus for the Maxwell model is

$$E_R(t) = E\,e^{-t/t_r} \tag{B.54}$$

where the relaxation time is defined as $t_r = \eta/E$.

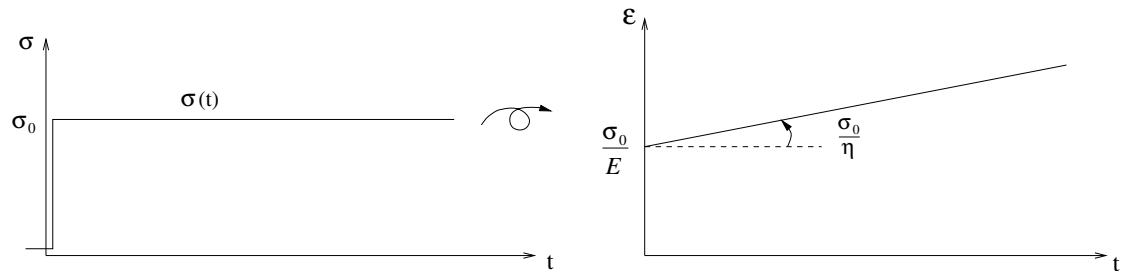

Figure B.18: *Creep behaviour of the Maxwell model .*

Creep compliance

The creep compliance $J_C(t)$ can be derived by solving (B.51) for a step load i.e. $\sigma(t) = const = \sigma_0$. For $t > 0$ it is concluded that $\dot{\sigma} = 0$, giving

$$\dot{\epsilon} = \frac{\sigma_0}{\eta} \Leftrightarrow \epsilon(t) = \epsilon(t_0) + \frac{\sigma_0}{\eta} \int_0^t d\tau \tag{B.55}$$

A sudden applied load gives the initial condition $\epsilon(t_0) = \sigma_0/E$ as a consequence that the dashpot acts like a rigid member and (B.55) can be written as

$$\epsilon(t) = (\frac{1}{E} + \frac{t}{\eta})\sigma_0 \tag{B.56}$$

From the definition of creep compliance i.e. $J_C(t) = \epsilon(t)/\sigma_0$ it is concluded that the creep compliance for the Maxwell model is

$$J_C(t) = \frac{1}{E} + \frac{t}{\eta} \tag{B.57}$$

Complex modulus

The complex modulus $E^*(\omega)$ for the Maxwell model can be determined by solving (B.51) for a steady state sinusoidal strain history

$$\epsilon^* = \epsilon_0 e^{i\omega t}$$

Inserting a trial solution $\sigma = Ce^{i\omega t}$ into (B.51) yields the stationary solution

$$C = E\frac{i\omega}{i\omega + E/\eta}\epsilon_0 = E\frac{i\omega t_r}{i\omega t_r + 1}\epsilon_0$$

Consequently we find the complex modulus

$$E^*(\omega) = E\frac{i\omega t_r}{1 + i\omega t_r} \tag{B.58}$$

for the Maxwell model, where $t_r = \eta/E$.

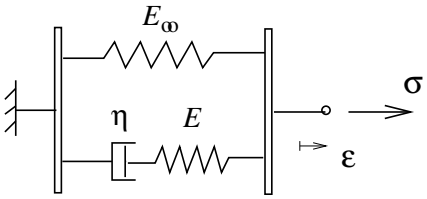

Figure B.19: *The Zener model. A spring coupled in parallel with a Maxwell element.*

B.3.3 The Zener model

To avoid the problem which is associated with the Kelvin-Voigt model, the dashpot element is replaced by a Maxwell element according to Figure B.19. This model is the so-called *Zener* or *standard linear solid model* which behaves like a solid. The Zener model is the simplest viscoelastic model with solid properties that reflects the behaviour of real solid materials in the sense that the relaxation behaviour is reasonable and the creep response is limited.

Differential equation

Let us denote the stress in the spring with σ_∞ and the stress in the Maxwell element with σ_M. The total stress σ in the Zener model, cf. Figure B.19, is then given by

$$\sigma = \sigma_\infty + \sigma_M \tag{B.59}$$

Equation (B.59) gives the following relation

$$\begin{cases} \sigma_M = \sigma - \sigma_\infty \\ \dot{\sigma}_M = \dot{\sigma} - \dot{\sigma}_\infty \end{cases} \tag{B.60}$$

Inserting the relation (B.60) in (B.51) gives

$$\begin{cases} \sigma_\infty = E_\infty \epsilon \\ \dot{\sigma} + \frac{E}{\eta}\sigma = E\dot{\epsilon} + \frac{E}{\eta}\sigma_\infty + \dot{\sigma}_\infty \end{cases} \tag{B.61}$$

i.e.

$$\dot{\sigma} + \frac{E}{\eta}\sigma = (E + E_\infty)\dot{\epsilon} + \frac{EE_\infty}{\eta}\epsilon \tag{B.62}$$

which is the differential equation that defines the stress-strain relation for the Zener model.

Relaxation modulus

Solving the equation (B.62) to a step strain history yields

$$\sigma_R(t) = E_\infty \epsilon_0 + Ee^{-\frac{E}{\eta}t}\epsilon_0 \qquad t > 0 \tag{B.63}$$

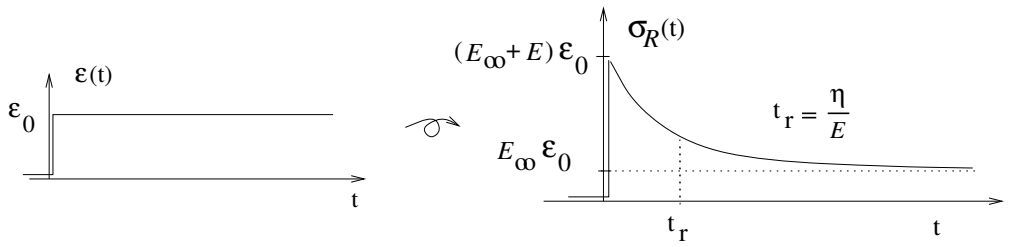

Figure B.20: *Relaxation behaviour of the Zener model; stress is relaxed to a long-term value.*

Hence, the relaxation modulus for the Zener model is

$$E_R(t) = E_\infty(1 + \frac{E}{E_\infty}e^{-t/t_r}) \tag{B.64}$$

The step strain response (B.64) is illustrated in Figure B.20. The instantaneous and the long-term response is

$$E_R(0) = E_\infty + E \qquad E_R(\infty) = E_\infty$$

according to (B.64), and the model gives elastic behaviour for both cases.

Creep compliance

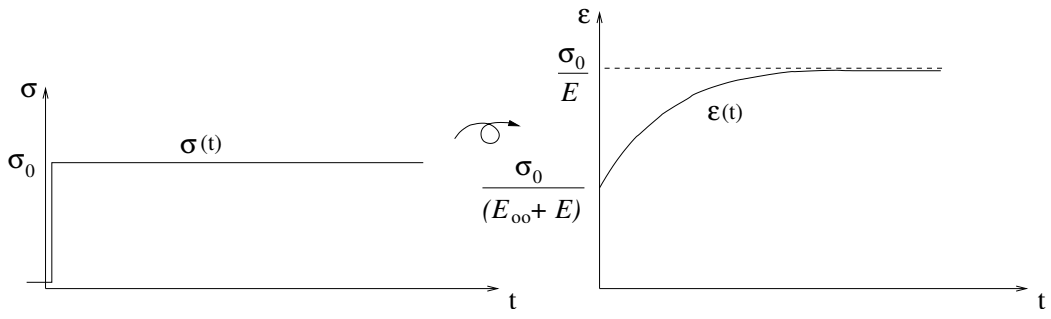

Figure B.21: *Creep behaviour of the Zener model.*

Solving the equation (B.61) to a step load history will give

$$\epsilon(t) = \frac{\sigma_0}{E_\infty} + \sigma_0(\frac{1}{E_\infty + E} - \frac{1}{E_\infty})e^{-\frac{E_\infty E}{\eta(E_\infty+E)}t} \qquad t > 0 \tag{B.65}$$

and consequently the creep compliance for the Zener model is given by

$$J_C(t) = \frac{1}{E_\infty} + (\frac{1}{E_\infty + E} - \frac{1}{E_\infty})e^{-\frac{E_\infty E}{\eta(E_\infty+E)}t} \tag{B.66}$$

Complex modulus

The complex modulus $E^*(\omega)$ for the Zener model can be determined by solving for a stationary sinusoidal strain. The strain is given by

$$\epsilon^* = \epsilon_0 e^{i\omega t} \tag{B.67}$$

The stress is given by inserting the Maxwell stress (B.58) into (B.59) according to

$$\sigma^* = E_\infty \epsilon^* + E\frac{i\omega t_r}{1+i\omega t_r}\epsilon^* \tag{B.68}$$

Hence, the complex modulus for the Zener model is

$$E^*(\omega) = E_\infty(1 + \frac{E}{E_\infty}\frac{i\omega t_r}{1+i\omega t_r}) \tag{B.69}$$

Consider three cases of harmonic excitation; low, medium, and high frequency i.e.

$$1) \quad \omega t_r \ll 1 \qquad 2) \quad \omega t_r \approx 1 \qquad 3) \quad \omega t_r \gg 1$$

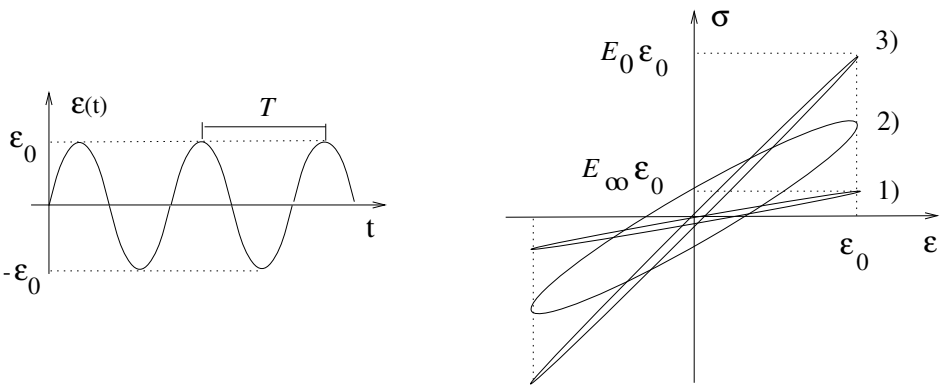

Figure B.22: *Linear viscoelastic solid response to sinusoidal excitation.*

The elliptic paths in the (σ, ϵ)-plane for the three cases are illustrated in Figure B.22. Low and high frequencies yield approximately elastic behaviour. Elastic behaviour is obtained if E^* is real, i.e. for $\omega t_r = 0$ and $\omega t_r = \infty$. For intermediate frequencies E^* is complex, giving hysteresis. The absolute value and the phase of E^* are shown in Figure B.23 as function of normalized frequency ωt_r.

Maximum phase angle (and hysteresis) occurs at $\omega t_r \approx 1$. An approximation of the maximum phase angle $\delta_{max} = max\{arg(E^*)\}$ can be shown [1] to be

$$\delta_{max} = \frac{g}{2-g} \qquad (\text{ for } \omega t_r \approx 1 \text{ and } g \leq 0.5)$$

with

$$g = \frac{E}{E + E_\infty}$$

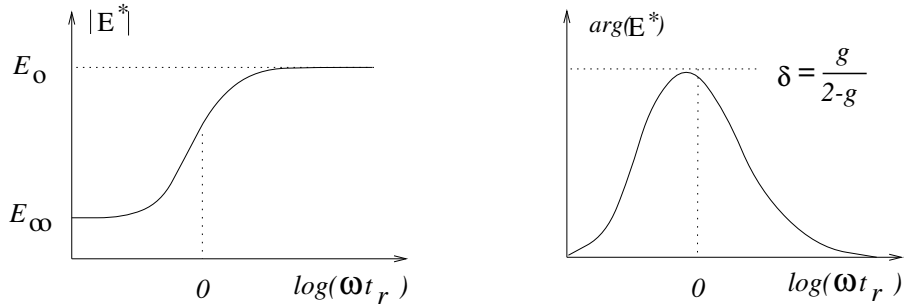

Figure B.23: *Zener model; frequency dependence of the complex modulus for* $g \leq 0.5$.

Summary

The Zener model responds approximately elastically for both very slow and very fast loading. This is because the dashpots behave like rigid members for fast loading rates and because the dashpot stresses are relaxed for slow loading rates.

The Zener model is a simple example of a linear viscoelastic solid model with physically reasonable properties.

B.4 Elastoplastic models

Filled rubber components exhibit an amplitude dependent behaviour. This section concerns the modelling of frictional (i.e. rate-independent) damping by a model including several frictional elements according to Figure B.24. Heavily filled rubbers develop a hysteresis loop which reminds of a parallelogram. The elastoplastic model in Figure B.24, the so-called *generalized frictional solid model*, is able to reproduce the parallelogram-shaped hysteresis loop of filled rubbers. Relaxation and creep is not represented by the models. Moreover, the response to a harmonic strain will not be harmonic due to the friction elements.

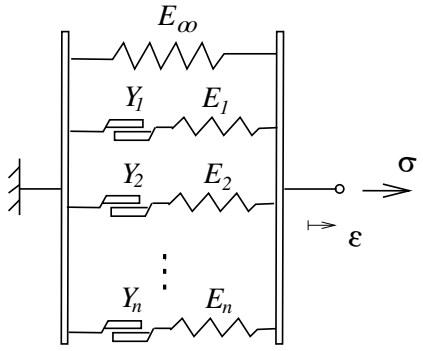

Figure B.24: *The generalized frictional solid model.*

An elastoplastic model consists of such basic components as the linear spring and two blocks with sliding friction. These components coupled in series give the

so-called frictional element. Elastic behaviour is described with a linear spring and the rate-independent damping is symbolized by the two blocks, shown in figure B.24. Since the elastoplastic model includes the frictional element, the model is able to describe the amplitude dependence of filled rubber.

B.4.1 The basic element

The frictional element has the important advantage to give decreasing dynamic modulus with increasing strain amplitude. However, the frictional element is not particularly physical by itself since a sudden application of strain gives a discontinuous stress response. The two blocks with sliding friction stay fixed together until

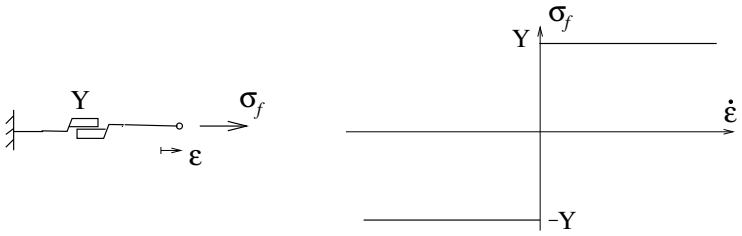

Figure B.25: *The basic element and stress response.*

the stress in the element reaches the yield limit. The stress in the element is then constant ±Y, depending on whether the sign of the strain-rate is positive or negative, see Figure B.25. This frictional element has an important advantage, namely the ability to describe amplitude dependence as will be shown in the next section.

B.4.2 Frictional analogy to the Kelvin-Voigt model

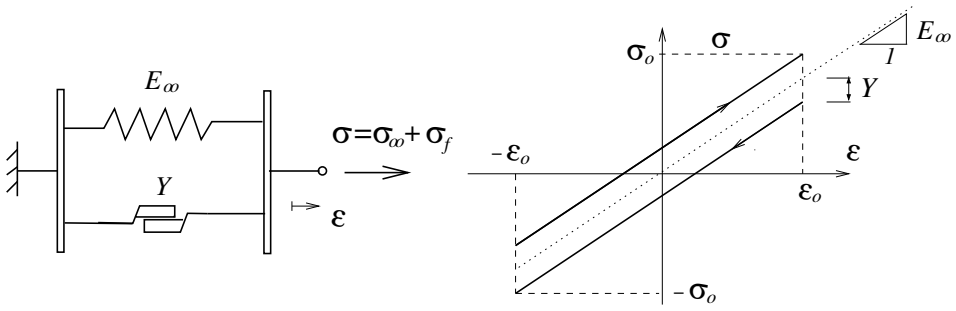

Figure B.26: *Friction model in analogy with the Kelvin-Voigt model.*

The simplest frictional model consists of a linear spring and two blocks coupled in parallel according to Figure B.26. This model is similar to the Kelvin-Voigt model, but the dashpot is replaced by two sliding blocks. The stress is a sum of the stress from the spring and the frictional element given by

$$\sigma = \sigma_\infty + \sigma_f \tag{B.70}$$

developing each term gives

$$\sigma_\infty = E_\infty \epsilon \qquad \sigma_f = Y sign(\dot{\epsilon}) \tag{B.71}$$

Equation (B.70) and equation (B.71) gives the stress equation

$$\sigma = E_\infty \epsilon + Y sign(\dot{\epsilon}) \tag{B.72}$$

Inserting a sinusoidal strain history

$$\epsilon(t) = \epsilon_0 sin\omega t \tag{B.73}$$

into the stress equation (B.72) yields

$$\sigma(t) = E\epsilon(t) sin\omega t \pm Y sign(cos\omega t) \tag{B.74}$$

This simple frictional model gives amplitude dependence with respect to dynamic modulus. Amplitude dependence is desirable since that is a feature of filled rubber components. The equation (B.75) for the dynamic modulus can be understood by studying Figure B.26. It gives decreasing dynamic modulus with increasing strain amplitude according to

$$E_{dyn} = \frac{\sigma_0}{\varepsilon_0} = E_\infty + \frac{Y}{\varepsilon_0} \tag{B.75}$$

The model does not show any relaxation behaviour. When the model is exposed to a step-strain, the response will be limited to Y, see Figure B.25. The model gives unphysical hysteresis with discontinuouities at the turning points cf. Figure B.26. The characteristics of this very simple frictional model can be summarized as:

- Discontinuous and unphysical hysteresis loop.
- An infinitely large dynamic modulus as the model is exposed to infinitely small strain.
- Amplitude dependence with respect to dynamic modulus.
- As all frictional models it does not show any relaxation behaviour.

B.4.3 Frictional analogy to the Maxwell model

If a spring and two blocks are coupled in series the "frictional Maxwell" is obtained. In terms of plasticity this is a one-dimensional elastic perfectly plastic model.

The rate-independent damping in the "frictional Maxwell" model is fully developed when the stress in the element reaches $\sigma_f = Y$. When the stress is less than Y, the two blocks are fixed together and the linear spring gives a linear elastic response, see Figure B.27. The stress-strain relationship for the element, in Figure B.27, must be evaluated for increments of strain and stress. The strain is a sum of elastic and (frictional) plastic strain $\epsilon = \epsilon^e + \epsilon^p$. The algorithm for the basic element is discussed in Chapter 2 Section 2.4.

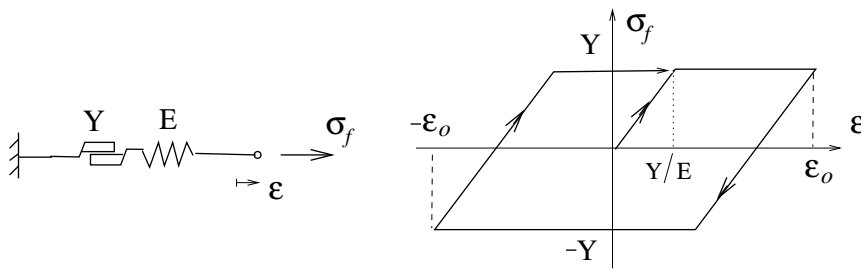

Figure B.27: *Frictional stress in the simple model.*

B.4.4 Frictional analogy to the Zener model

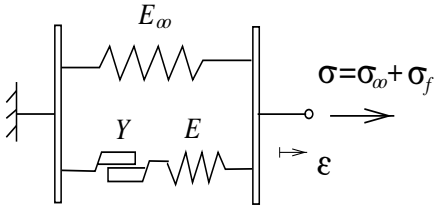

Figure B.28: *Frictional model including elastic and frictional properties. The yield strain* $\epsilon_s = Y/E$.

The model is similar to the Zener model, but the rate-dependent dashpot is replaced by a rate-independent frictional element. It has the same configuration as the model in Section B.4.2, except that it has a spring in series with the sliding blocks, according to Figure B.28. The advantage with the extra spring is a limited increase in dynamic modulus with decreasing amplitude. In terms of plasticity this is a kinematic linear hardening von Mises model.

The hysteresis loop for the total stress, also shown in Figure B.29, is the sum of the frictional stress shown in Figure B.27 and the elastic stress (in the spring with the modulus E_∞) i.e.

$$\sigma = \sigma_\infty + \sigma_f$$

The rectangular hysteresis according to Figure B.27 is tilted due to the elastic stress $\sigma_\infty = E_\infty \epsilon$ giving the hysteresis shown in Figure B.29.

The parallelogram-shaped hysteresis loop is the same for different kinds of periodic strain excitation with the same amplitude. That is, a sine, sawtooth or square-shaped periodic function yields the same response, regardless of the frequency, if the amplitude is the same.

As mentioned earlier, this model describes the dynamic modulus and damping in a better way. As one may se in Figure B.30, the dynamic modulus increases with decreasing amplitude, but the dynamic modulus is limited for extremely small amplitudes.

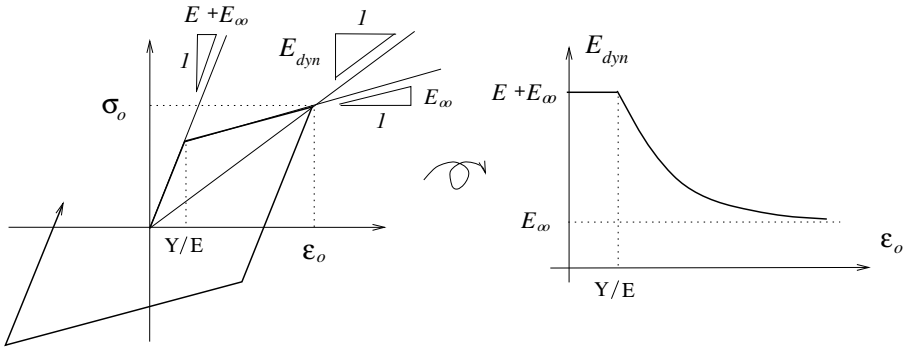

Figure B.29: *Amplitude dependence in the simple frictional model.*

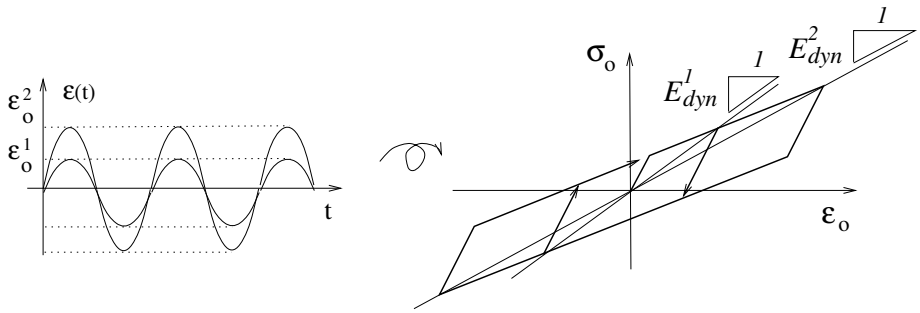

Figure B.30: *Amplitude dependence of the dynamic modulus.*

Maximum stress and maximum strain occur simultaneously, and the dynamic modulus is according to Figure B.29 calculated at that point as $E_{dyn} = \sigma_0/\epsilon_0$. If the strain is below the yield limit $\epsilon_s = Y/E$, the two sliding blocks are fixed together and the model is fully elastic with a constant modulus $E + E_\infty$. When the strain amplitude exceeds the yield limit the two blocks start to slide, the blocks and the linear elastic spring coupled in parallel give $\sigma_0 = Y + E_\infty \epsilon_0$. The dynamic modulus decreases with increasing amplitude according to

$$E_{dyn} = \frac{\sigma_0}{\epsilon_0} = E_\infty + \frac{Y}{\epsilon_0} \qquad \epsilon_0 > \epsilon_s \tag{B.76}$$

In order to determine the damping, the definition discussed in Appendix A Section A.3.1 will be used. The damping can be determined from the area enclosed in one cycle. This area is the same as for the basic element (the hysteresis is just tilted) and it is simpler to determine that area (cf. Figure B.27).

We have to look at two cases. If the strain amplitude is below the yield strain then the area enclosed is zero because there will not be any hysteresis and the damping $d = 0$. Otherwise, the area is $U_c = 4Y(\epsilon_0 - \epsilon_s)$ and the stress amplitude is $\sigma_0 = Y + E_\infty \epsilon_0$. The damping given by the normalized dissipated energy in each cycle is thus given by

$$d = \frac{4}{\pi} \frac{\epsilon_0 - \epsilon_s}{(1 + E_\infty \epsilon_0 / Y)\epsilon_0} \qquad \epsilon_0 > \epsilon_s$$

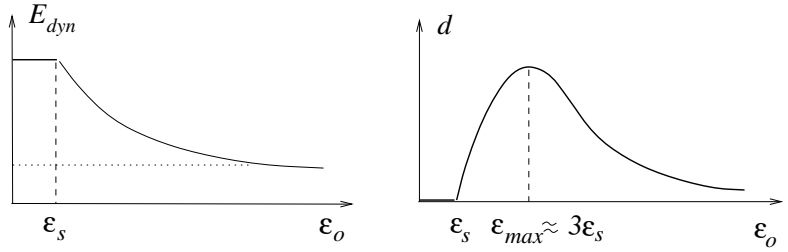

Figure B.31: *The damping for the simple frictional model.*($\epsilon_s = Y/E$)

This frictional model have the same characteristics as the model described in Section B.4.2 with one important exception:

- Infinitely small strain amplitudes give limited dynamic modulus.

Summary

The elastoplastic models consist of linear elastic springs and sliding blocks. The elastoplastic models does not show any relaxation behaviour. The advantage with the elastoplastic models is the capability of modelling amplitude dependence.

Appendix C

Error functions

Appendix C deals with how the error function ϕ is established for different kinds of linear viscoelastic and elastoplastic models. Error functions for linear viscoelastic models are first discussed and thereafter error functions for elastoplastic models.

C.1 Error functions for linear viscoelastic models

The equations for the complex modulus E^* for linear viscoelastic models were derived in Appendix B. In Chapter 4, the experimental data were expressed on a structural level. However, as it was concluded in Chapter 3, the material and structural level expressions are almost the same. The material level models are simply connected to the structural level models by some geometric factor. The dynamic stiffness can therefore be expressed as $K^* = (geometric\ \ factor) * E^*$. Using the theoretical expressions together with the experimental data in equation (5.1) yields the stiffness and phase angle in terms of unknown component parameters.

C.1.1 Kelvin-Voigt model

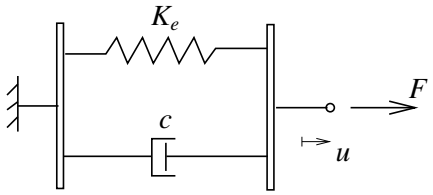

Figure C.1: *The Kelvin-Voigt model: A spring coupled in parallel with a dashpot.*

There are two material parameters in the Kelvin-Voigt model cf. Figure C.1 which are to be fitted to experimental data. The model equations for a Kelvin-Voigt material were derived in Appendix B and as the Kelvin-Voigt model is a viscoelastic model it is found that E_{dyn} and $d = sin(\delta)$ only are functions of the angular velocity ω, see equation (B.48) and equation (B.49).

In the case of moderate damping, i.e. $\delta < 0.4\,rad$ $(\approx 23^o)$ the approximation $d = sin(\delta) \approx \tan(\delta) \approx \delta$ can be used and equation (B.48) can therefore be expressed as

$$d_{theor} = \frac{\eta}{E}\omega \tag{C.1}$$

The equations (B.48)-(B.49) are derived on the material level i.e. functions of E and η and the dynamic modulus from the experimental data are expressed on the structural level i.e. $K_{dyn,exp}$. It is therefore necessary to rewrite the equations (B.48) and (B.49). In accordance with Chapter 3 Section 3.1 the structural geometry is assumed to be in the form of a uniaxially loaded bar. This approach leads to

$$K_{dyn,theor} = \sqrt{K_e^2 + c^2\omega^2} \tag{C.2}$$

which is the structural level equation corresponding to (B.49). Equation (C.1) can be rewritten on structural level as

$$d_{theor} = \frac{\frac{cL}{A}}{\frac{K_e L}{A}}\omega = \frac{c}{K_e}\omega \tag{C.3}$$

The two material parameters K_e and c are obtained by minimization of the function ϕ expressed as

$$\phi = \sum_{i=1}^{n}((\frac{\sqrt{K_e^2 + c^2\omega_i^2}}{K_{dyn,exp}^i} - 1)^2 + (\frac{c\omega_i}{K_e d_{exp}^i} - 1)^2) \tag{C.4}$$

where n denotes the number of measurements.

C.1.2 Zener model

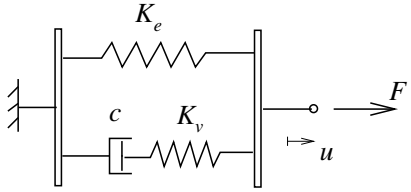

Figure C.2: *The Zener model: A spring coupled in parallel with a Maxwell element.*

The Zener model is also a simple viscoelastic solid model. However, it has some clear benefits compared to the Kelvin-Voigt model. It was mentioned in Appendix B that the Kelvin-Voigt model, can not exhibit relaxation. This problem is circumvented in the Zener model with a spring coupled in series with the dashpot giving the simplest viscoelastic model that can reflect the principal behaviour of a real solid

material. The difference between the Zener model and the Kelvin-Voigt model is that the dashpot is replaced by a Maxwell element. This leads to a model requiring evaluation of three material parameters K_e, K_v, and c, according to Figure C.2.

The expression for the complex modulus in Appendix B Section B.3.3 is rewritten here

$$E^*(\omega) = E_\infty(1 + \frac{E}{E_\infty}\frac{i\omega t_r}{1 + i\omega t_r}) \tag{C.5}$$

From Appendix B Section B.2.3 it is known that $E_{dyn,theor} = |E^*(\omega)|$ and $d_{theor} = sin(\delta) = sin(arg(E^*(\omega)))$ likewise $t_r = \eta/E$. The transition from material to structural level using equation (C.5) yields

$$K^*(\omega) = K_e + K_v\frac{i\omega}{1 + i\omega t_r}t_r \tag{C.6}$$

where t_r in equation (C.6) is expressed as $t_r = c/K_v$.

By making use of the interpretation of complex stiffness in analogy with complex modulus it is concluded that

$$K_{dyn,theor} = |K^*(\omega)| \tag{C.7}$$

and

$$d_{theor} = \sin(\delta) = \sin(arg(K^*(\omega))) \tag{C.8}$$

Equation (C.7) and (C.8) make it possible to establish the error function ϕ, i.e. equation (5.1).

C.1.3 Generalized Maxwell model

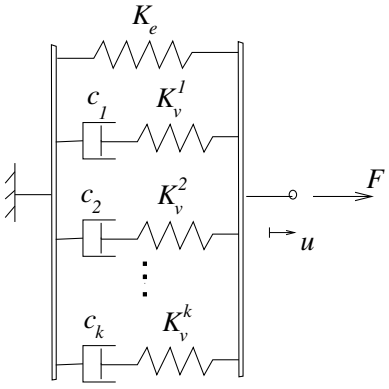

Figure C.3: *The generalized Maxwell model: A spring in parallel with several Maxwell elements.*

If more than one Maxwell element is coupled in parallel with a spring, the model is called generalized Maxwell model. This model has the same properties as the Zener model but with better ability to accurately fit the rate dependence in experimental data as a consequence of the arbitrary number of Maxwell elements.

Generalization of the Zener model to contain more than one Maxwell element gives a complex stiffness in analogy with complex modulus, (see Appendix B), as

$$K^*(\omega) = K + \sum_{j=1}^{k} K_v^j \frac{i\omega t_r^j}{1 + i\omega t_r^j} \tag{C.9}$$

where k denotes the number of Maxwell element. Equation (C.9) and the relations (C.7)-(C.8) make the error function ϕ complete.

C.2 Error functions for elastoplastic models

In this section fitting procedures for elastoplastic models , i.e. no viscous elements, are discussed. A frictional element is a rate-independent element and the experimental data are therefore evaluated for amplitude interval

$$[\hat{u}_1, \ldots, \hat{u}_n]$$

At each amplitude 1 to n the dynamic stiffness $K_{dyn,exp}$ and the phase angle δ_{exp} are measured. Hence, the following experimental data are obtained

$$[K^1_{dyn,exp}, \ldots, K^n_{dyn,exp}] \qquad (N/m)$$

$$[\delta^1_{exp}, \ldots, \delta^n_{exp}] \qquad (rad)$$

As for the viscoelastic models, the component parameters are obtained with an optimization approach. Hence, the error function (5.1) is also used in elastoplastic models.

C.2.1 Frictional model in analogy with Maxwell model

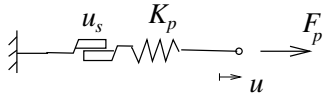

Figure C.4: *Basic frictional element.*

The behaviour of the basic frictional element depends on whether it is plastic or not (cf. Figure C.4), i.e. whether the displacement $\hat{u}$ is larger than the yield displacement u_s. In analogy with material level expressions

$$K_{dyn,theor} = \begin{cases} \frac{K_p u_s}{\hat{u}} & \text{if } u_s < \hat{u} \\ K_p & \text{otherwise} \end{cases} \tag{C.10}$$

The definition of the normalized damping from viscoelasticity (A.2) is repeated here and used in order to determine the damping d_{theor}

$$d = \sin(\delta) = \frac{U_c}{\pi \sigma_0 \epsilon_0} \tag{C.11}$$

U_c is the enclosed area created by the loading and unloading curve and represents the dissipated energy in each cycle. The definition of the normalized damping d will coincide with the phase angle for moderate damping, i.e. $d \approx \delta$ ($\sin(\delta) \approx \delta$ for small δ).A transition from material to structural level makes it possible to rewrite equation (C.11) according to

$$d = \sin(\delta) = \frac{U_s}{\pi \hat{F} \hat{u}} \tag{C.12}$$

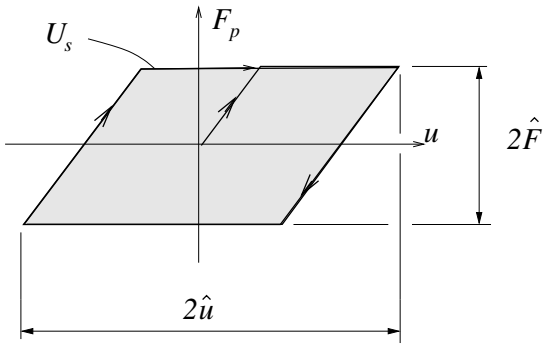

Figure C.5: *The enclosed area U_s in a $F-u$ diagram.*

U_s is the enclosed area in a $F-u$ diagram, $\hat{F}$ is the applied force amplitude, and $\hat{u}$ is the applied displacement amplitude (cf. Figure C.5). There are two possible expressions for the hysteretic work U_s

$$U_s = \begin{cases} 4K_p u_s(\hat{u} - u_s) & \text{if } u_s < \hat{u} \\ 0 & \text{otherwise} \end{cases} \tag{C.13}$$

i.e. if the displacement amplitude is below the yield displacement u_s , the enclosed area is zero and the damping $d = 0$. Otherwise, the area is expressed according to $U_s = 4K_p u_s(\hat{u} - u_s)$. Inserting equation (C.13) in equation (C.12) will determine the damping d_{theor}.

Equation (C.10) and (C.13) together with equation (C.12) and the experimental data make it possible to establish the error function ϕ , i.e. equation (5.1).

C.2.2 Frictional model in analogy with Zener model

A simple frictional model can be represented by a spring coupled in parallel with a basic frictional element cf. Figure C.6. There are three material parameters

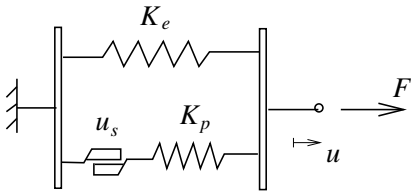

Figure C.6: *Frictional model in analogy with Zener model.*

K_e, K_p, and u_s which are to be fitted to experimental data by use of the error function. Therefore it is necessary to find expressions for $K_{dyn,theor}$ and d_{theor}.

If the applied displacement amplitude $\hat{u}$ is below the yield displacement u_s, the model is fully elastic with a constant stiffness $K_e + K_p$. The total force in the model when the displacement amplitude exceeds the yield limit can be determined according to $\hat{F} = K_p u_s + K_e \hat{u}$. The dynamic stiffness decreases thus with the inverse of the displacement amplitude according to

$$K_{dyn,theor} = \frac{\hat{F}}{\hat{u}} = K_e + \frac{K_p u_s}{\hat{u}} \tag{C.14}$$

To summarize it is concluded that

$$K_{dyn,theor} = \begin{cases} K_e + \frac{K_p u_s}{\hat{u}} & \text{if } u_s < \hat{u} \\ K_e + K_p & \text{otherwise} \end{cases} \tag{C.15}$$

There are two possible expressions for the damping d_{theor}. If the displacement amplitude $\hat{u}$ is below the yield displacement u_s , U_s in equation (C.12) is zero and also the damping d_{theor}. Otherwise, the damping is obtained from equation (C.12) rewritten here according to

$$d_{theor} = \sin(\delta) = \frac{U_s}{\pi \hat{u} K_p u_s} \tag{C.16}$$

where U_s is calculated according to equation (C.13). Equation (C.15) and (C.16) together with the error function (5.1) make it possible to evaluate the unknown component parameters K_e, K_p, and u_s.

C.2.3 Generalized frictional solid model

Generalized frictional solid models contain more than one basic frictional element which leads to several component parameters i.e. K_e, $K_p^1, \ldots, K_p^m$ and $u_s^1, \ldots, u_s^m$ where m denotes the number of basic frictional element cf. Figure C.7. The total dynamic stiffness $K_{dyn,theor}$ is obtained from the following expressions

$$K_{dyn}^j = \begin{cases} \frac{K_p^j u_s^j}{\hat{u}_i} & \text{if } u_s^j < \hat{u}_i \\ K_p^j & \text{otherwise} \end{cases} \tag{C.17}$$

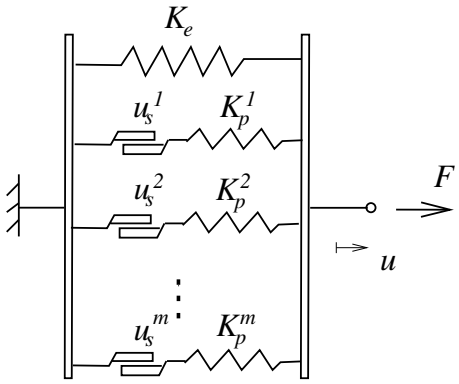

Figure C.7: *Generalized frictional solid model.*

and

$$K_{dyn,theor} = K_e + \sum_{j=1}^{m} K_{dyn}^j \tag{C.18}$$

The damping d_{theor} can be calculated by summing the enclosed areas for the basic frictional elements that yield at a particular displacement amplitude $\hat{u}$. The total damping can therefore be obtained from the following expression

$$d_{theor} = \sin(\delta) = \frac{\sum_{j=1}^{m} U_s^j}{\pi \hat{u} \sum_{j=1}^{m} K_p^j u_s^j} \tag{C.19}$$

where U_s^j is calculated according to

$$U_s^j = \begin{cases} 4K_p^j u_s^j(\hat{u}_i - u_s^j) & \text{if } u_s^j < \hat{u}_i \\ 0 & \text{otherwise} \end{cases} \tag{C.20}$$

With the error function (5.1) together with the expressions derived above for $K_{dyn,theor}$ and d_{theor}, the unknown component parameters can be evaluated.

Appendix D

Component parameters

The fitted component parameters for the viscoelastic models and the generalized non-linear elastic viscoelastic elastoplastic model are tabled in this section.

D.1 Viscoelastic models

Kelvin-Voigt

Component	K_e [N/mm]	c [Ns]
Shear specimen A	172.2919	0.0953
Shear specimen B	211.1067	0.2582
Cylindrical bushing C	1035.6000	0.5558
Cylindrical bushing D	1141.3000	1.1006

Table D.1: *The component parameters for the Kelvin-Voigt model.*

Zener

Component	K_e [N/mm]	K_v [N/mm]	t_r [s]
Shear specimen A	140.1991	58.6715	0.027700
Shear specimen B	161.6707	134.5649	0.008800
Cylindrical bushing C	905.4096	134.5649	0.006800
Cylindrical bushing D	877.2268	541.1714	0.006500

Table D.2: *The component parameters for the Zener model.*

Generalized Maxwell

Component	K_e [N/mm]	K_v [N/mm]	t_r [s]
Shear specimen A	80.2974	47.0714	9.219100
		17.2353	0.274700
		21.1840	0.021200
		40.1433	0.002300
Shear specimen B	91.8722	55.7943	1.810300
		39.1573	0.219300
		51.5727	0.013100
		83.0546	0.001600
		47.3225	0.001500
		111.5544	0.001300
Cylindrical bushing C	490.6290	309.3259	0.584500
		143.1166	0.015700
		268.9768	0.001500
Cylindrical bushing D	532.1760	434.7185	0.085010
		218.6918	0.007800
		495.6674	0.000830
		359.7936	0.000460

Table D.3: *The component parameters for the generalized Maxwell model.*

D.2 Generalized non-linear elastic viscoelastic elastoplastic model

The left column identifies which specimens that are tabled.

	C_{10}	C_{20}	C_{30}	K_v [N/mm]	t_r [s]	K_p [N/mm]	u_s [mm]
A	53.4938	-0.1648	0.0015	0.6678	0.021535	54.2000	2.2909
				3.3322	0.020338	24.8990	5.3929
				15.8280	0.002021	12.5560	12.7160
						4.2478	12.5660
B	40.9413	-0.1583	0.0015	17.5170	0.004727	217.6800	4.9650
						71.4620	6.8941
						32.9800	14.2370
						14.7550	18.0970
C	383.3117	-1.4602	0.0503	12.1060	0.024697	436.4100	56.3350
				59.0040	0.004518	62.9890	41.2440
				41.4530	0.000773	40.6520	57.4790
D	389.4253	-2.1094	0.0786	61.4760	0.004335	1016.6000	101.5800
						301.0400	42.2560
						25.5160	12.6950
						33.9180	17.7630
						54.9620	35.1160
						84.9550	110.6800

Table D.4: *The component parameters for the generalized non-linear elastic viscoelastic elastoplastic model.*

Bibliography

[1] Austrell P.-E., (1997), *Modeling of Elasticity and Damping for Filled Elastomers*, Report TVSM-1009, Lund University, Division of Structural Mechanics, Sweden, 1997.

[2] Austrell P.-E., Bellander M., Carlsson U., Kari L., Persson S., Stenberg B., (1998), *Survey of Design Methods and Material Characteristics in Rubber Engineering*, Report TVSM-3036, Lund University, Division of Structural Mechanics, Sweden, 1998.

[3] Olsson, A.K., and Austrell, P-E., (2001), *A Fitting Procedure for Viscoelastic-Elastoplastic Material Models*, Proceedings of the Second European Conference on Constitutive Models for Rubber, Germany, 2001.

[4] Austrell, P-E., Olsson, A.K., and Jönsson, M., (2001), *A method to analyze the non-linear dynamic behaviour of carbon-black-filled rubber components using standard finite element codes*, Proceedings of the Second European Conference on Constitutive Models for Rubber, Germany, 2001.

[5] Harris J. and Stevenson A., (1986), *On the Role of Nonlinearity in the Dynamic Behavior of Rubber Components*, Rubber chemistry and technology, Vol. 59, pp.741-764, 1986.

[6] Lindley P.B., (1974), *Engineering Design with Natural Rubber*, MRPRA, 1974.

[7] Malvern L.E., (1969), *Introduction to the Mechanics of a Continous Medium*, Prentice-Hall, 1969.

[8] Mullins L., (1969), *Softening of Rubber by Deformation*, Rubber Chemistry and Technology, Vol. 42, pp.339-362, 1969.

[9] Ottosen, N.S., and Ristinmaa, M., (1999), *The Mechanics of Constitutive Modelling, (Numerical and thermodynamical topics)*, Lund University, Division of Solid Mechanics, Sweden, 1999.

[10] Payne A.R., (1965), *In Reinforcement of Elastomers*, G.Kraus, Ed., Interscience, Chap. 3, New York, 1965.

[11] Yeoh O.H., (1990), *Characterization of Elastic Properties of Carbon-black-filled Rubber Vulcanizates*, Rubber Chemistry and Technology, Vol. 63, pp. 792-805, 1990.

[12] Berg M., (1998), *A non linear rubber spring model for rail vehicle dynamics analysis*, Vehicle System Dynamics 30, pp. 197-212, 1998.

[13] Besseling J.F., (1958), *A Theory of Elastic, Plastic, and Creep Deformation of an Initially Isotropic Material.*, J. Appl. Mech. 25, pp. 529-536, 1958.

[14] Coveney V.A., Johnsson D.E., and Turner D.M., (1995), *A Triboelastic Model for the Cyclic Behavior of Filled Vulcanizates*, Rubber Chemistry and Technology, Vol. 68, 1995.

[15] Gregory M.J., (1985), *Dynamic properties of rubber in automotive engineering*, Elastomerics 19, November 1985.

[16] Kari L. and Sjöberg M., (2002), *Non-linear behaviour of a rubber isolator system using fractional derivatives*, Vehicle System Dynamics, No 3, pp. 217-236, 2002.

[17] Kraus G., (1984), *Mechanical Losses in Carbon-Black-Filled Rubbers*, J. Appl. Polym. Sci.: Applied Polymer Symposium 39, 1984.

[18] Medalia A.I., (1978), *Effects of Carbon-black on Dynamic Properties of Rubber*, Rubber Chemistry and Technology, Vol.51, pp.437, 1978.

[19] Ulmer J.D., (1995), *Strain Dependence of Dynamic Mechanical Properties of Carbon-Black-Filled Rubber Compounds*, Rubber Chemistry and Technology, Vol. 69, pp.15-47, 1995.

[20] Vieweg S. et. al., (1995), *Frequency and Temperature Dependence of the Small-Strain Behavior of Carbon-Black-Filled Vulcanizates*, Polym. Networks Blends, 5(4), pp. 199-204, 1995.

[21] Warnaka G.E., (1962), *Effects of Dynamic Strain Amplitude on the Dynamic Mechanical Properties of Polymers*, ASME Rubber and Plastics Div., New York, Pre-print 62-WA: 323, 1962.